Unipolar Charge-Sensing for Evaporated Large-Area Solid-State Photoconductors for Digital Radiography

by

Amirhossein Goldan

A thesis
presented to the University of Waterloo
in fulfillment of the
thesis requirement for the degree of
Doctor of Philosophy
in
Electrical and Computer Engineering

Waterloo, Ontario, Canada, 2012

I hereby declare that I am the sole author of this thesis. This is a true copy of the thesis, including any required final revisions, as accepted by my examiners.

I understand that my thesis may be made electronically available to the public.

- Amirhossein Goldan

Abstract

An alternative approach to energy integrating systems is photon counting which provides higher dose efficiency through efficient noise rejection and optimal energy weighting, and, moreover, is not susceptible to memory artifacts such as image lag and ghosting. The first large-area photon counting imager was Charpak's Nobel Prize winning invention of the gas-filled multiwire proportional chamber (MWPC), which revolutionized the field of radiation detection in 1968. In most applications, however, the use of a solid detection medium is preferable because solid densities are about three orders-of-magnitude greater than gas, and thus, they can yield much smaller detector dimensions with unsurpassed spatial and temporal resolution.

Thus far, crystalline Cadmium Zinc Telluride is the only room-temperature solid-state detector that meets the requirements for photon counting imaging. However, the material is grown in small ingots and production costs are high for large-area imaging applications. The problem is that disordered (or non-crystalline) solids, which are easier and less expensive to develop over large-area than single crystalline solids, have been ruled out as viable photon counting detectors because of their poor temporal resolution, or more specifically, extremely low carrier mobilities and transit-time-limited photoresponse.

To circumvent the problem of poor charge transport in disordered solids with a conventional planar detector structure, we propose unipolar charge sensing by establishing a strong near-field effect using an electrostatic shield within the material. We introduce the concept of time-differential photoresponse in unipolar solids and show that their temporal resolution can be improved substantially to reach the intrinsic physical limit set by spatial dispersion.

Inspired by Charpak's MWPC and its variants, and for the first time, we have implemented an electrostatic shield inside evaporated amorphous selenium (a-Se) using the proposed lithography-based microstrip solid-state detector (MSSD). The fabricated devices are characterized with optical, x-ray, and gamma-ray impulse-like excitations. Using optical time-of-flight (TOF) measurements, we show for the first time a unipolar Gaussian TOF transient from the new MSSD structure, instead of a rectangular response with a Gaussian-integral at the tail which is a typical response of a conventional planar device. The measured optical and x-ray TOF results verify the time-differential property of the electrostatic shield and the practicality of the dispersion-limited photoresponse. Furthermore, we use single gamma-ray photon excitations to probe detector's temporal resolution in pulse mode for photon counting. For the MSSD, we show a depth-independent signal for photon absorption across the bulk and a reduction in signal rise-time by a factor of 350, comparing performance limiting factors being hole-dispersion for the MSSD and electron-transit-time for the conventional planar device.

The time-differential response obtained from the proposed unipolar detector structure enables disordered photoconductive films to become viable candidates for large-area photon counting applications.

Acknowledgements

First and foremost, I would like to thank Assoc. Prof. Dr. Karim S. Karim for his supervision and support of this work.

This doctoral project would not have been possible without the encouraging support of my mentor, Prof. Dr. John A. Rowlands. I wish to express my deepest gratitude to Dr. Rowlands who inspired me greatly and offered invaluable assistance, support and guidance during my academic endeavor.

I would like to show my appreciation to the members of my supervisory committee, Prof. Dr. John A. Rowlands, Prof. Dr. Siva Sivoththaman, Assoc. Prof. Dr. Ehsan Toyserkani, and Prof. Dr. David W. Holdsworth, for accepting to review my work.

I am highly indebted to Dr. Olivier Tousignant and Dr. Giovanni DeCrescenzo who were abundantly helpful and offered immense assistance throughout the experimental work.

I am grateful to Dr. Hadi Izadi and Dr. Ehsan Fathi for providing training and assistance with film deposition and device fabrication. I also thank Dr. Hamidreza Alemohammad for assistance with SOLIDWORKS and COMSOL simulation tools.

I would like to thank Mr. Richard Barber for his sincere efforts in maintaining the Giga-to-Nanoelectronics (G2N) centre facilities at the University of Waterloo, where my devices were fabricated photolithographically. Also, the support received from ANRAD Corporation was vital for the success of this project. Amorphous selenium films were deposited at ANRAD corporation.

Special thanks go to my special friends: Dr. Ehsan Fathi, soon-to-be-Dr. Mohsen Sepehr, Dr. Hamidreza Alemohammad, Dr. Mohammad Esmaeili, Dr. Majid Gharghi, and Dr. Arash Akhavan for the memorable times we spent in Waterloo.

I would like to express my deepest love and gratitude to my wonderful father for his unconditional love, sacrifice, and never-ending support.

Finally, I am very grateful to my beautiful wife, Sadaf, for her love and patience.

To my father,

with deepest love and gratitude

Table of Contents

List of Tables

List of Figures

Chapter 1

Introduction

1.1 Motivation

The limitations with the current direct conversion flat panel detectors (FPDs) are poor dose efficiency, due to poor noise rejection and incorrect energy weighting, and the presence of memory artifacts and anatomical noise in the radiographs. For x-ray tomosynthesis, in order not to increase the patient dose, the imaging system must readout multiple (ideally ∼100) images with each image using only a small portion (i.e., 1%) of the normal dose. However, this puts an extreme requirement on the detector in regards to the total input-referred noise level. Almost all mammographic detectors currently available are based on energy integrating techniques which are amplifier noise limited in the areas of low x-ray exposure (i.e., the dark part of the image) and require additional radiation to make up for this deficiency. Increasing the pixel readout rate, to achieve higher frame rates required for tomosynthesis, makes this problem worse and thus, overcoming the amplifier noise in the subdivided images (i.e., one frame of the 3D tomosynthesis image) is a key challenge in implementing a practical tomosynthesis system. For a constant x-ray exposure, a higher frame rate in photon integrating systems leaves less integration time for the incoming photons to build up a sufficient input signal level while background noise levels stay relatively constant. Thus, higher frame rates can lead to noise-vulnerable input signals.

The root of these limitations is the operation of the radiation detector in *current mode* with energy-integrating readout. An alternative approach is to operate the detector in *pulse mode* for individual photon counting which provides higher dose efficiency through efficient noise rejection and optimal energy weighting. Photon counting systems are also not susceptible to memory artifacts. However, the preceding benefits come at the expense of a complex on-pixel readout circuitry, which can only be implemented in complementary metal-oxide semiconductor (CMOS) technology. In addition, the requirements for an imaging detector to operate in pulse mode are: (1) room-temperature operation, (2) high resistivity and low leakage, (3) high radiation absorption efficiency, (4) high conversion gain to enable single photon detection, and (5) fast operation for high count-rate and high frame rate. Thus far, crystalline Cadmium Zinc Telluride (CZT) is the only room-temperature solid-state detector that meets the requirements for large-area radiation imaging. However, the material is grown in small ingots, and thus, a 4-side buttable design is necessary for large-area. Also, the material is relatively expensive to grow as single crystal. Currently, the high cost associated with the large-area detector growth and CMOS readout electronics is the major drawback of photon counting systems.

Amorphous selenium (a-Se), which was previously developed for photocopying machines, has been commercially revived as a direct x-ray photoconductor for digital imaging in FPDs because it has high x-ray sensitivity and can be uniformly evaporated over large area as a thick film. However, amorphous solids (i.e., non-crystalline solids with disorder) which are easier and less expensive to develop over large area than single crystalline solids, have been ruled out as viable radiation imaging detectors in pulse mode because of their low temporal resolution. Furthermore, a necessary condition for complete charge collection is that the carrier lifetime exceeds the transit time across the detector thickness. In disordered solids, this condition is generally met by only one type of carrier that has a higher mobility-lifetime product. Also, given that photon interaction depths vary across the bulk, the slow signal risetime for the portion of the induced charge due to the slower carrier and significant trapping cause depth-dependent noise. The issue of low temporal resolution and depth-dependent noise are both related to poor charge transport properties in disordered solids due to extremely low carrier mobilities and transit-time-limited photoresponse.

1.2 Objectives

This research, given the aforementioned benefits of photon counting systems, investigates methods of circumventing the problem of poor carrier transport in disordered solids to substantially improve their temporal resolution in pulse-mode and enable them as viable candidates for photon counting applications.

Conventionally, a planar radiation detector is comprised of a photoconductive material fitted between two electrodes to form a sandwich cell: one is the drift electrode and the other is the collector. We propose modifying the detector structure to enable preferential sensing of only the carrier type with a higher mobility-lifetime product (i.e., the primary carrier) and providing insensitivity of the collector to the transport properties of the slower carrier type. Such localized preferential sensing of primary carriers, which is also referred to as unipolar (or single-polarity) charge sensing, is implemented by establishing a strong near-field effect using an electrostatic shield within the photoconductive material. We introduce the concept of time-differential photoresponse in unipolar solids and show that their temporal resolution can be improved substantially to reach the intrinsic physical limit set by spatial dispersion.

Inspired by Charpak's multiwire proportional chamber and its variants, and for the first time, we show the fabrication process for establishing an electrostatic shield inside evaporated solids using the proposed lithography-based microstrip solid-state detector (MSSD). The fabricated devices are characterized with optical, x-ray, and gamma-ray impulse-like excitations. Optical and x-ray time-of-flight transient photoconductivity measurements are used to verify the time-differential property of the electrostatic shield and the practicality of the dispersion-limited photoresponse. Single gamma-ray photon excitations are used to measure photoresponse risetime, and thus, characterize detector's temporal resolution in pulse mode for photon counting.

One must note that energy-integrating systems, aside from their limitations, are still being actively pursued by FPD manufacturers as a basis technology for commercially available area-imaging x-ray tomosynthesis systems. This is because of two technological advances: 1) the availability of cost-effective, large area a-Si TFT readout panels, and 2) successful and reliable coupling of the evaporated amorphous selenium photoconductor to these large-area readout panels. Thus, this research also investigates incremental performance improvements provided by the proposed unipolar photoconductors in energy-integrating current mode, which are higher charge collection efficiency, higher spatial resolution, and lower image lag.

1.3 Thesis Organization

Background Topics:

In chapter 2, we provide a brief background on digital radiography systems and investigate the limitations with the current direct conversion flat panel detectors (FPDs). We show the significance of pulse mode operation for individual photon counting to improve imager's dose efficiency.

In chapter 3, we investigate the nature of conduction in amorphous (also called non-crystalline or disordered) solids based on a model presented by Nevill Mott. We show the different mechanisms of transport as the strength of disorder increases.

Design, Implementation, and Characterization of the Proposed Device:

In chapter 4, we investigate the deteriorating effect of poor carrier transport on the temporal resolution and the counting rate of an amorphous selenium (a-Se) spectrometer. We propose a novel photoconductive device structure, based on unipolar charge sensing using the near field effect of electrostatic shields, for circumventing the problem of poor carrier transport in not just a-Se, but also any solid with any degree of disorder. Most importantly, we introduce the concept of time-differential photoresponse using the new device and investigate the performance improvement in temporal resolution and its intrinsic physical limit.

In chapter 5, we implement the new proposed device with electrostatically shielding grids between the sandwich electrodes using evaporated photoconductive films, designs that have been inspired by Charpak's multiwire proportional chambers and its variants. Most importantly, we show the construction of the first microstrip solid-state detector (MSSD) using standard photolithography which has proven to be very effective for establishing a strong near field effect.

In chapter 6, we characterize the fabricated devices using three impulse-like excitations. The first two experiments include optical and x-ray time-of-flight transient photoconductivity measurements to verify our predictions being (1) the time-differential property of the electrostatically shielding microstrips and (2) the dispersion-limited photoresponse. The third experiment is a single gamma-ray photon excitation to characterize device's temporal response in pulse mode.

Other Related Topics:

In chapter 7, we drive analytical expressions for the operation of unipolar charge-sensing solid-state photoconductors in energy-integrating current mode. The analyze imager's performance in terms of x-ray sensitivity, detective quantum efficiency (DQE), modulation transfer function (MTF), and image lag. Finally, we present theoretical results underscoring the performance improvements for digital medical imaging modalities such as mammography tomosynthesis and real-time fluoroscopy.

In chapter 8, we reexamine the question of whether the increased charge injection due to the increased electric field, or the detrapping of the bulk space charge is the dominant mechanism for the persistent photocurrent lag. Using a unipolar detector, we experimentally investigate the level of reduction in image lag due to insensitivity of the collector to the detrapping of the low-mobility space charge.

Conclusion:

Chapter 9 summarizes the results presented in this thesis and concludes by providing the most important contribution of the author to research.

Chapter 2

Digital Radiography Detectors

2.1 Historical Background

Radiography is an imaging procedure where x-rays emitted from the x-ray tube pass through one side of a patient and the transmitted x-rays are detected on the other side. Different tissues have different x-ray attenuation properties and the degree of beam attenuation after passing through the patient depends on the type and the thickness of the tissues along the beam trajectory.

The field of projection radiography (e.g., chest radiography, mammography, fluoroscopy) was created soon after the discovery of x-rays by Wilhelm Röntgen in 1985, and the first radiograph was that of Mrs. Röntgens hand shown in Fig. 2.1a. Since its initiation, radiography has been vastly improved over the past century in terms of dose efficiency and image quality. Figure 2.1b shows an image of a hand taken with a state-of-the-art x-ray

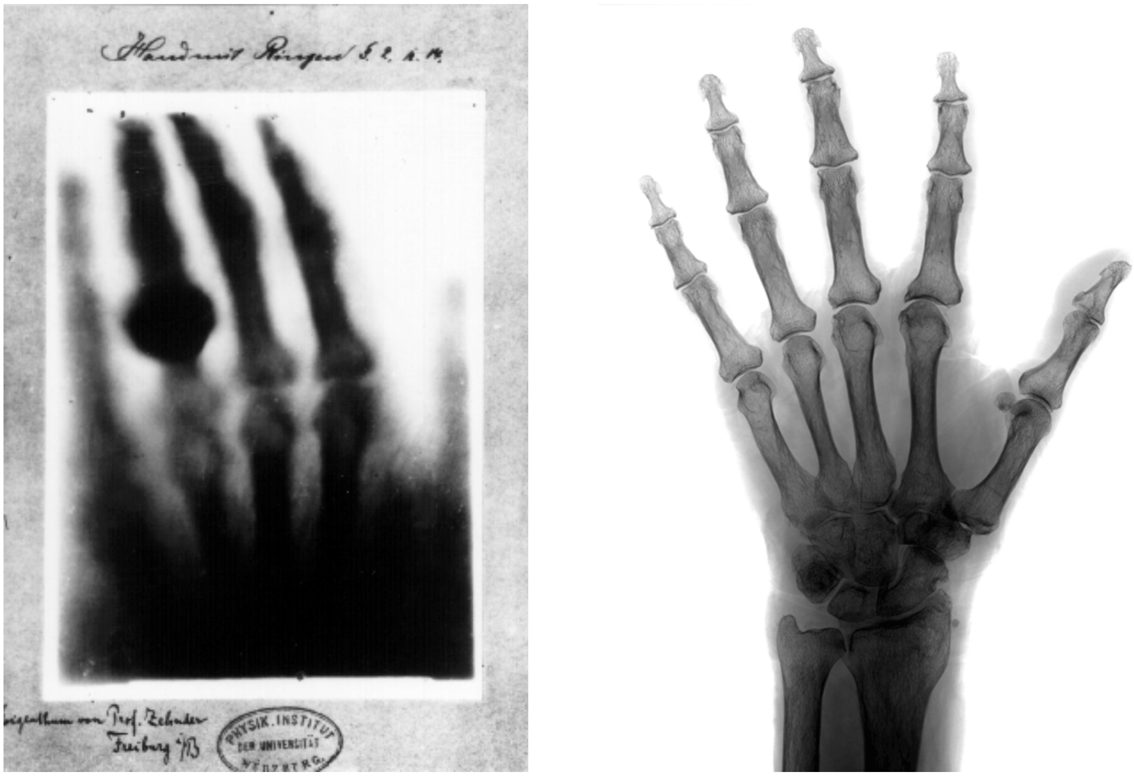

(a) (b)

Figure 2.1: (a) The first medical x-ray image taken by Wilhelm Röntgen on December 22, 1985. The radiograph is of his wife's hand. (b) X-ray image of a hand taken with a modern imager (courtesy of ANRAD Corporation).

imager. Such high quality bone images are used today in the diagnosis and monitoring of bone pathologies, such as osteoporosis and arthritis.

A conventional screen-film detector for radiography is illustrated in Fig. 2.2a, which consists of a cassette, intensifying screens made of a scintillating material (also called a phosphor), and a film with a photosensitive emulsion coating on both sides. The attenuated x-rays incident on the cassette are absorbed by the screen and converted into visible or

Table 2.1: Detector design requirements for digital radiography. Data is extracted from Table 1 in Ref. [2].

	Chest radiography	Mammography	Fluoroscopy
Detector size (cm)	35 × 43	18 × 24	25 × 25
Pixel size (μm^2)	200 × 200	50 × 50	250 × 250
Number of pixels	1750 × 2150	3600 × 4800	1000 × 1000
Image readout time (s)	<5	<5	0.033
X-ray spectrum (kVp)	120	30	70
Mean exposure to image detector (mR)	0.3	12	0.001

ultraviolet (UV) light. The light emitted by the phosphor exposes the film and creates a latent image, which is later developed chemically and becomes a manifest radiograph [1].

Considering the digital imaging modalities, computed tomography (CT) and magnetic resonance imaging (MRI), which have been clinically available since 1970s and 1980s, respectively, are intrinsically digital. Also, ultrasound and nuclear medicine imaging transitioned from analog to digital in the 1970s. Radiography, however, is the only imaging modality that has not yet made full transition from analog screen-film technology to digital acquisition. The reason is because modern screen-film is a full-field, large area detector system with high spatial resolution. To produces images of equivalent quality and spatial resolution as screen-film, digital radiography detectors must satisfy the requirements listed in Table 2.1, which are challenging to achieve [2].

Recently, digital radiography detectors, such as charge-coupled devices (CCDs) and flat panel detectors (FPDs), have been commercialized and are slowly replacing screen-film cassettes in radiology centers and hospitals. The key advantages provided by digital detectors over the conventional analog ones include: (i) same, or possibly better, image quality can

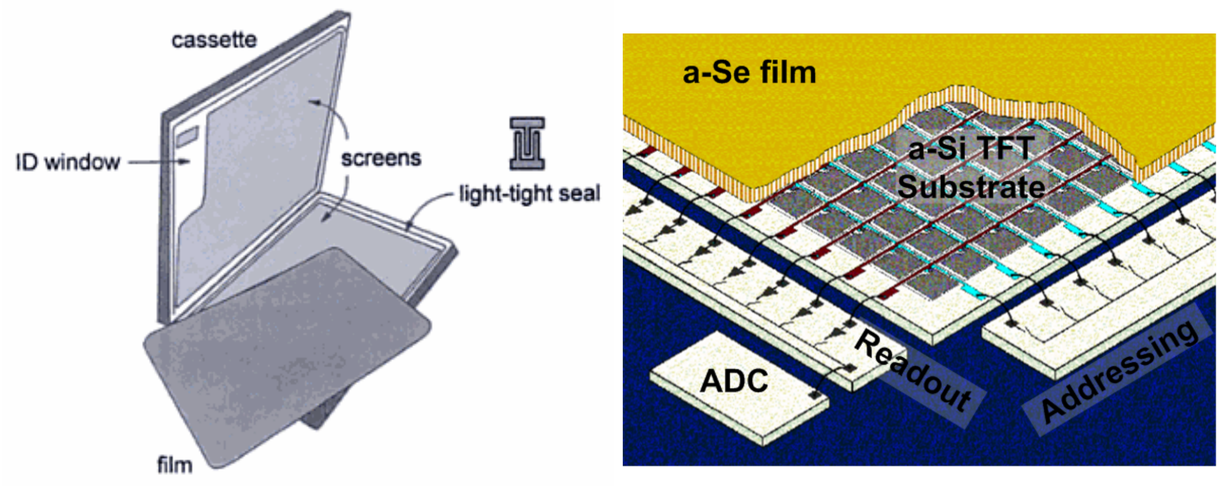

(a) (b)

Figure 2.2: (a) Conventional screen-film detector for general radiography [1]. The film, which is a thin plastic with a photosensitive emulsion coating on both sides, is sandwiched between two intensifying screens inside the cassette. (b) Direct conversion flat panel detector (FPD) for digital radiography.

be obtained with lower patient dose, (ii) captured digital data can undergo post-processing to improve image quality, (iii) computer-aided detection can help the diagnosis of subtle legions, (iv) images can be viewed faster after acquisition without the need for chemical development, and finally, (v) data can be easily stored and transferred electronically. A direct detection flat panel imager is shown in Fig. 2.2b. The photoconductive film is amorphous selenium and is evaporated over an amorphous silicon (a-Si) thin-film transistor (TFT) substrate. X-ray photons absorbed by the photoconductor release electron-hole pairs (EHPs) which then drift in the presence of the applied electric field. Movement of carriers inside the detector bulk induces charge on the pixel electrode and this charge is integrated by the underlying two-dimensional array of TFT-based passive pixel sensors (PPS) [1], [2].

2.2 Direct versus Indirect Detection of X-rays

Solid-state FPDs consist of an x-ray absorption layer coupled to a readout substrate. In direct detection, x-rays are absorbed in a photoconductive film and converted to charge in a single step. In indirect detection, absorbed x-rays in the phosphor screen are first converted to optical photons and subsequently to electronic charge by the photodiode. In both direct and indirect detection, the produced charge is collected by the solid-state readout, which for commercial energy integrating systems is an a-Si TFT substrate with a PPS readout architecture.

Generally, direct detectors are preferred over indirect imaging. Indirect detectors suffer from image blur caused by the lateral spread of the induced light in the phosphor, which reduces spatial resolution at high frequency. The blur diameter is typically in the order of the phosphor layer thickness. Absorbed x-rays in photoconductors, however, generate charge very close to the primary interaction site, and then carriers drift towards their respective electrodes by the applied electric field. The size of the collected charge cloud is negligible compared to the radiography pixel sizes, and thus, direct detectors provide unsurpassed spatial resolution. Also, direct detectors do not require optical coupling elements and because of a single conversion stage, they do not suffer from the secondary quantum sink [3], [4].

Amorphous selenium (a-Se) is the most highly developed photoconductor for large area x-ray imaging applications, owing to its commercial use as a xerographic photoreceptor in industry [5]. Note that the material is structureless with no grain boundaries, and consequently, no granularity noise is present even at very high spatial resolutions. Most importantly, a-Se films are reliably evaporated over large-area substrates and the fabrication process is less costly than that of indirect detectors.

This research, for the preceding reasons, only considers direct detection x-ray imagers with evaporated solid-state photoconductors. The work identifies limitation of the existing FPDs, as energy integrating imagers, and presents new device solutions to overcome some of the limitations and to improve imagers performance.

2.3 Dose Efficiency

An imaging systems dose efficiency is characteristic of its overall performance considering the following factors: 1) quality of the x-ray spectrum, 2) quantum efficiency, 3) energy absorption efficiency, 4) scatter rejection efficiency, 5) conversion efficiency (of absorbed photons to image signal), 6) detector noise (i.e., swank noise, film granularity noise, leakage shot noise, variations in the conversion gain), and finally, 7) readout noise. Currently, all conventional screen-film and area-imaging digital radiography detectors are operated in energy integrating mode. The dose efficiency of a conventional screen-film mammography system with a Smit-Röntgen antiscatter grid, 35% detective quantum efficiency (DQE), and 30 kVp molybdenum (Mo) x-ray spectrum is illustrated in Fig. 2.3. The simulated data is extracted from Fig. 1 in Ref. [6], and can also be representative of the dose efficiency for a mammography a-Se FPD with 35% DQE at a spatial frequency of 4 lp/mm (LMAM, Anrad Corporation, St. Laurent, Quebec, Canada) [7], [8]. Note that DQE is different than dose efficiency in that it excludes degradation due to scatter and shape of the polyenergetic bremsstrahlung x-ray beam. The reason for such low dose efficiency,

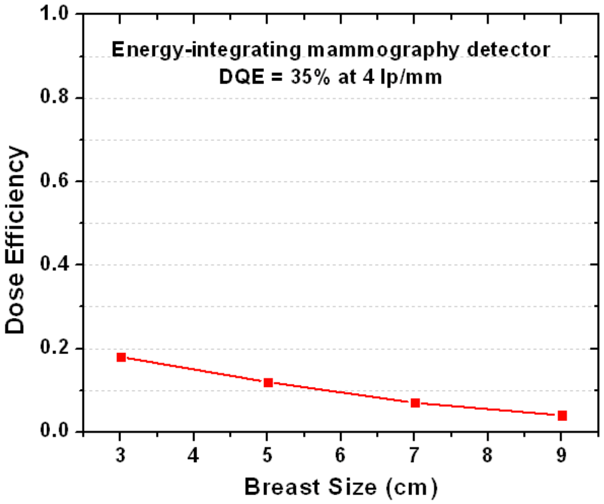

Figure 2.3: Dose efficiency of an energy-integrating mammography system with a Smit-Röntgen antiscatter grid and 35% DQE, using a 30 kVp Mo x-ray spectrum. Results are extracted from Fig. 1 in Ref. [6].

compared to an ideal system with 100% DQE that is exposed to a monoenergetic x-ray source at the optimum energy, is due to poor scatter and noise rejection, and low conversion efficiency due to non-optimal energy weighting.

2.3.1 Scatter

The dose efficiency of an area-imaging x-ray detector can be affected by Compton scattered photons. The percentage loss in dose efficiency due to scattered photons is tabulated in Table 2.2 for both area-imaging and scanning systems. The area-imaging, energy integrating mammography detectors were simulated with both a Smit-Röntgen and a Lorad antiscatter grid. Simulations are based on a Monte-Carlo modelling of a 5 cm thick breast with a 100 μm microcalcification and a mean glandular breast tissue (i.e., 50% glandular

Table 2.2: Percentage loss in the dose efficiency of area-imaging and scanning mammography systems due to scattered photons. Results for area-imaging detectors are extracted from Table 5 in Ref. [9]. Simulations are based on a Monte-Carlo modelling of a 5 cm thick breast with a 100 μm microcalcification and a mean glandular breast tissue (i.e., 50% glandular and 50% adipose). The 30kVp x-ray spectrums used are for both tungsten (W) and molybdenum (Mo) targets.

	Area-Imaging		Scanning
X-ray spectrum	Smit-Röntgen grid [9]	Lorad grid [9]	Scanned-slit [6]
30 kVp W	26%	14%	3%
30 kVp Mo	30%	14%	3%

and 50% adipose) [9].

In comparison to area-imaging detectors with a loss in dose efficiency of as much as 30% (using a 30kVp tungsten spectrum and a Smit-Röntgen grid), scanning systems provide the advantage of being inherently immune to Compton scatter and are reported to degrade dose efficiency by only 3% [6]. However, scanning systems highly collimate the x-ray beam and are very inefficient in utilizing the x-rays emitted from the x-ray tube. A complete patient scan can impose an immense heating on the tube, and thus, special x-ray tubes with high heat storage capacity must be designed for clinical applications [10]. To date, area-imaging systems with much better x-ray utilization have been preferred and using Lorad grids, their scatter rejection efficiency can be improved [11].

2.3.2 Detector and readout noise

An ideal system in terms of noise rejection is the one that is fundamentally limited by the uncertainty in the statistical distribution of the incident x-ray photons. Given a Poisson distribution and 100% quantum efficiency, the number of absorbed x-rays in a detector fluctuates around its mean N with a standard deviation $N^{1/2}$. Such a system is said to be quantum limited with a signal-to-noise (SNR) ratio $N^{1/2}$.

In an *energy integrating* detector, photon energies of the incident x-ray spectrum are absorbed and converted to electronic charge, and the charge is integrated during a fixed time. The accumulated charge at the end of the integration cycle is readout and digitized to represent the raw pixel value. This readout scheme is susceptible to both detector and readout noise. The detector noise components are the swank noise [12] and the leakage shot noise. The noise of the PPS readout architecture, for example, are the flicker and the thermal noise of the on-pixel TFT switch, the thermal noise of the column charge amplifier, and the analog-to-digital converter (ADC) noise. The total input-referred noise of an indirect FPD is reported to be ∼2500 electrons for a 100 μm pixel pitch [13]. The poor noise rejection of energy integrating systems greatly limits their DQE at low exposures, and thus, additional radiation dose to the patient is required to compensate for this deficiency.

Photon counting systems, however, are inherently quantum limited and reject both detector and readout noise at the expense of a complex on-pixel readout circuitry. In photon counting detectors, the value of each image pixel is equal to the number of photons that interact with the detector, and thus, swank noise is no longer present. The integrated photon-generated charge is amplified and filtered and the output is compared to a low-level discriminator. The filtering action reduces the background noise (or the total input-referred noise), which arises from the detector and the readout circuitry, and the discriminator rejects the remaining filtered background noise. Note that only signals that are larger than the low-level discriminator value are counted as valid events [14]. Preferably, the low-level discriminator value must be high enough for optimal noise rejection, and low enough not to provide significant beam hardening.

2.3.3 Conversion efficiency and optimal energy weighting

Higher energy photons deposit more charge in the detector than low energy ones, but in mammography, optimal energy weighting requires the photon weighting factor, w, to be inversely proportional to the cube of the photon energy (i.e., $w \propto E^{-3}$) [15]. This is because the higher part of the 30 kVp energy spectrum, after having passed through the patients breast, carries lower contrast anatomical data. Traditionally, to produce higher contrast mammograms, operators were using the lowest possible mean energy for the x-ray spectrum at the expense of higher patient dose.

Another problem with energy integrating detectors is their inefficiency to convert the absorbed photon energy to the image signal, because photons are weighted in proportion to their energy (i.e., $w \propto E$). Such weighting is different than the optimal energy weighting by a factor of E^4. In photon counting systems, however, signals exceeding the low-level discriminator value are counted as valid events and assigned the same weight. Thus, w is independent of energy and is equal to unity (i.e., $w = 1$). Table 2.3 shows how (1) different energy weightings and (2) different spectrums, generated by tungsten (W) and molybdenum (Mo) targets, impact dose efficiency. Note that photon counting can improve dose efficiency by as much as 14% compared to energy integration.

Another limiting factor for conversion efficiency is due to the nature of carrier transport inside the bulk of the photoconductor. The effective mobility of carriers in most practical

Table 2.3: Percentage loss in the dose efficiency due to non-optimal energy weighting for mammography. Results are extracted from Table II in Ref. [15] and are based on a 100 μm microcalcification.

X-ray spectrum	Energy integrating ($w \propto E$)	Photon counting ($w = 1$)	Optimal ($w \propto E^{-3}$)
30 kVp W	26%	16%	0%
30 kVp Mo	30%	16%	0%

x-ray detectors can be substantially different for holes and electrons due to their respective charge transport properties. In addition, trapping effects, which dominate in amorphous and poly-crystalline materials, can result in *schubweg*[1] limited charge transport and reduce the collection efficiency of the photon-generated charge [16]. Incomplete charge collection reduces the conversion efficiency for both energy integrating and photon counting readout techniques. Most importantly, poor carrier transport in a-Se, for example, has enormously limited its photon count rate and made the photoconductor impractical in photon counting mode for digital radiography applications [17].

Detailed discussion of the implications of poor charge transport and our proposed solution to improve charge collection efficiency and photon count rate are provided in chapter 4.

---

[1] Schubweg is defined as the carrier drift range before being deeply trapped and is equal to the products of the carrier mobility, the carrier lifetime, and the applied electric field.

2.4 Memory Artifacts in Direct Detection FPDs

Memory artifacts are seen in radiographs, which are caused by the spill-over of residual signal from previous exposures into subsequent image frames [18]. Such memory effects, which relax with time, are attributed to interrupted carrier transport by deep traps in the detector bulk and degrade the imagers temporal response. Memory effects are characterized by two important figures of merit: (1) persistent photocurrent lag, and (2) ghosting [19]. Persistent photocurrent lag manifest itself as increased dark conductivity after x-ray exposure. Ghosting is the change in detector sensitivity due to previous exposures, and as opposed to lag, it is measured during subsequent x-ray exposures [20].

Amorphous selenium is currently a dominant force in static mammography imaging applications but, due to image lag, has limited use in high frame rate modalities such as real-time fluoroscopy [21]. Other direct detection materials such as poly-crystalline mercuric iodide (HgI2) and lead-oxide (PbO) have not yet entered commercial use mainly due to longer lag decay time compared to a-Se [22].

2.5 Anatomical Noise and X-ray Tomosynthesis

Conventional screen-film mammography does not detect all cancers and as many as 20% of cancers that become clinically evident over the course of a year will not have been visible by screening mammography performed within that year [23]. A major factor contributing to this limitation is the anatomical noise created by the overlap of normal structures within the breast, which are superimposed on each other in a standard two-dimensional mammogram. To improve the visualization of the desired pathologies in the breast, this tissue overlap effect has to be reduced or eliminated. Breast tomosynthesis is a three-dimensional (3D) imaging modality that can reduce or even eliminate the tissue overlap effect by reinforcing the pathology of interest and blurring the underlying and overlying structures. Initial studies show that tomosynthesis has the ability to reveal 16% more cancers than conventional mammography and reduce false positives by 85% even at a radiation dose to the patient comparable to a conventional two-view mammogram [23], [24].

2.6 Conclusions

We showed that the limitations with the existing direct conversion flat panel detectors (FPDs) are poor dose efficiency (due to poor noise rejection and non-optimal energy weighting) and the presence of memory artifacts and anatomical noise in the radiographs. The root of these limitations is the operation of the radiation detector in *current mode* with energy-integrating readout which is susceptible to poor noise rejection and incorrect energy weighting. We showed that by switching the operation to *pulse mode* for individual photon counting, we can gain higher dose efficiency through efficient noise rejection and suboptimal energy weighting. Photon counting systems are also not susceptible to memory artifacts. However, the preceding benefits come at the expense of a complex on-pixel readout circuitry, which can only be implemented in complementary metal-oxide semiconductor (CMOS) technology. In addition, the requirements for an imaging detector to operate in pulse mode are: (1) room-temperature operation, (2) high resistivity and low leakage, (3) high radiation absorption efficiency, (4) high conversion gain to enable single photon detection, and (5) fast operation for high count-rate and high frame rate. Thus far, Cadmium Zinc Telluride (CZT) is the only room-temperature solid-state detector that meets the requirements for large-area radiation imaging. However, the material is grown in small ingots, and thus, a 4-side buttable design is necessary for large-area. Also, the material is relatively expensive to grow as single crystal. Currently, the high cost associated with the large-area detector growth and CMOS readout electronics is the major drawback of counting systems for radiation imaging. Amorphous solids, which are easier and less expensive to develop over large area than single crystalline solids, have been ruled out as a viable radiation detection medium because of low carrier mobilities and transit-time-limited photoresponse. In the following chapters we investigate the nature of conduction in amorphous solids and propose a method for circumventing the problem of poor carrier transport to enable detectors such as evaporated amorphous selenium operate in pulse mode for large-area photon-counting radiation imaging.

Chapter 3

Conduction in Disordered Solids

3.1 Introduction

The most common amorphous (non-crystalline) material is Glass, which is interesting to know that the art of manufacturing glass goes back to prehistoric times [25]. Silicon dioxide (SiO_2), also known as *silica*, is a fundamental compound used in the production of glass for windows, drinking cups, and etc. The striking fact about glass is that it's transparent which, using band theory, means there is a forbidden gap of energies between the occupied states (called the valence band) and the empty states (called the conduction band) and that photons in the visible range do not have sufficient energy to excite electrons across this gap. This explanation of transparency is questionable, because band theory was introduced as a result of solving the Schrödinger equation for a crystalline lattice with a periodic potential. Also, sharp Bragg reflections from crystalline materials is the cause of their energy gaps. However, glass and glassy solids (i.e., amorphous solids with a glass transition) are without the long range order of atomic sites, and thus, do not have a periodic potential. Furthermore, amorphous materials generally do not show a sharp Bragg reflection. These striking facts about amorphous materials persuaded Mott around 1967 to be the first to ask the question "how can glass be transparent?" [26]. What was also curious to him, given such contradictions between amorphous and crystalline solids, was the result of the Leningrad experiments by Kolomiets [27] which showed that the concept of bandgaps can be extended to amorphous solids. The question was then how to describe this gap.

Mott started his theoretical model with two important clues. First was the Ioffe-Regel criterion for conduction in highly scattering materials, which states that the carrier-mean-free path cannot be less than the interatomic spacing. And second was the energy state localization of electrons in the presence of disorder-induced random potential, which was introduced by Anderson. Mott's work on the application of modern quantum physics to disordered semiconductors and metals has been at the forefront of solid state physics, and for that he was awarded the 1977 nobel prize for physics, a prize that he shared with Philip W. Anderson and John Van Vleck.

3.2 Clues to the nature of conduction

Clues to the nature of conduction in amorphous solids were the Ioffe-Regel criterion [28] and the Anderson localization [29]. Both clues relate to the extent of disorder in a given system.

3.2.1 Ioffe-Regel criterion

> *It is hardly necessary to prove that [for semiconductors with the mean-free-path less than the the interatomic spacing] the mechanism of mobility itself must be altogether different, and that the concept of mean free path has no meaning. The electron waves fade out within the limits of a single unit of the crystal lattice.*
>
> Abram F. Ioffe and Anatoli R. Regel, 1960 [28]

Ioffe and Regel argued that the carrier mean-free-path, L, cannot be less than interatomic spacing, a, otherwise the electron wave diminishes within the limits of a single potential well of a crystal lattice, and thus, the concept of mobility based on carrier mean velocity would be meaningless. In metallic systems, when disorder is sufficiently large that $L < a$, metal-insulator transition occurs [30].

3.2.2 Anderson localization

> *The central idea of my paper [29] was to suggest that under some circumstances the exact eigenstates in a macroscopic random lattice might be localized rather than extended throughout the lattice.*
>
> Philip W. Anderson, 1970 [31]

> *Very few believed [localization] at the time, and even fewer saw its importance; among those who failed to fully understand it at first was certainly its author. It has yet to receive adequate mathematical treatment, and one has to resort to the indignity of numerical simulations to settle even the simplest questions about it. Only now, and through primarily Sir Nevill Mott's efforts, is it beginning to gain general acceptance.*
>
> Philip W. Anderson, Nobel Lecture [32],
> 8 December, 1977

Let's start with the time-independent single-electron Schrödinger equation and consider the periodic potential well model for a crystalline lattice shown in Fig. 3.1a

$$E\psi(\mathbf{r}) = -\frac{\hbar^2}{2m}\nabla^2\psi(\mathbf{r}) + V(\mathbf{r})\psi(\mathbf{r}) \tag{3.1}$$

where E is the energy eigen value of the Hamiltonian, $\psi(\mathbf{r})$ is the electron wavefunction, $-\frac{\hbar^2}{2m}\nabla^2$ is the kinetic energy operator, $\hbar$ is the Plank's constant h divided by 2π, m is the particle mass, ∇^2 is the Laplace operator, and $V(\mathbf{r})$ is the time-independent potential energy. Note that in the crystalline lattice, scattering is weak and the carrier mean-free-path is long ($L \gg a$). The fixed periodic lattice potential is considered a perturbation that modifies the free-electron states leading to *"Bloch states"* in the well. We use the tight-binding approximation (TBA) for the single-electron atoms where the electron wavefunctions are mostly localized about their respective atomic cores and the overlap between wavefunctions of neighbouring sites is small. Thus, an approximate solution to eq. 3.1 is a linear combination of atomic orbitals (LCAO)

$$\psi(\mathbf{r}) = \sum_{\mathbf{R_n}} e^{i\mathbf{k}\cdot\mathbf{R_n}} \varphi(\mathbf{r} - \mathbf{R_n}), \quad \text{for } L \gg a \tag{3.2}$$

where $\mathbf{R_n}$ locates an atomic site in the lattice, $\varphi(\mathbf{r})$ is the electron wavefunction for a single isolated atom, and $\varphi(\mathbf{r} - \mathbf{R_n})$ is periodic with the periodicity a. Solving for energy eigen values yields a narrow band of energy levels with a bandwidth B, as shown in Fig. 3.1a. Also, in this model states are delocalized and belong to the entire crystal.

Now consider the Anderson lattice with a random potential, as shown in Fig. 3.1b. In the Anderson lattice, the disorder of tightly bound atoms is modelled as a cascade of wells with random potentials and variation of the potential has a uniform distribution of width W [33]. The strength of the disorder is measured by the ratio

$$\delta = W/B. \tag{3.3}$$

Anderson proved that sufficient disorder results in characteristic solutions to the Schrödinger equation with energy states that are localized in space [29]. Figure 3.2 shows the extent of localized states as the strength of disorder is increased. Such distribution for the density of states in the Anderson model indicates that any amount of random variation in the potential, however small, will introduce localized states at the band tail. Mott, whose

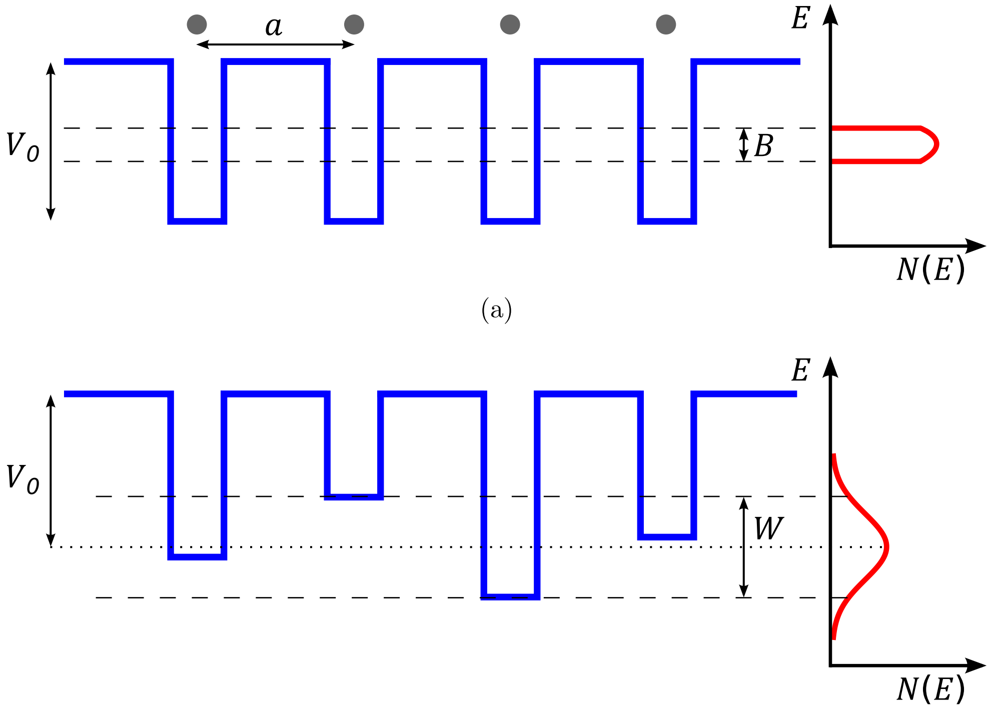

(a)

(b)

Figure 3.1: (a) Periodic potential wells for a crystalline lattice. (b) Random potential wells for a disordered lattice. Adapted from Fig. 1 in Ref. [33].

model of conduction is heavily based on the Anderson localization, was first to point out the existence of a critical energy E_C separating the localized tail from the non-localized states [34], [35]. He defined localized states below E_C as states where the d.c. conductivity at zero temperature vanishes. This supported Anderson's argument that in a disordered solid with deep wells of random depths, an electron that is localized in one of these wells cannot diffuse away. E_C was later called the "mobility edge" when state localization was first introduced in the amorphous semiconductor band model by Cohen et al [36].

When the amount of disorder reaches the Anderson criterion, localization occurs at the centre of the band at the fermi level, E_F [37]. Materials in which states at E_F are localized have been called "Fermi glasses" by Anderson[31]. The evaluation of the critical value, δ_c, for the Anderson criterion has proved difficult and has been a subject of many debates in literature where a range from 1 to 5.5 has been proposed. But what is apparent is that in some cases δ_c is proportional to the atomic coordination number, and in others experimental estimates of δ_c have come from measurements of the minimum metallic conductivity. Figure 3.2 shows $\delta_c = e \approx 2.7$ for which the Anderson criterion for localization is satisfied.

It was emphasized by Ioffe-Regel that the shortest possible mean-free-path is equal to the inter-atomic spacing. In a disordered solid with $L \approx a$, the wavefunction loses phase memory due to strong scattering when it hops from one atom to the next, and thus, the new solution to eq. 3.1 is of the form

$$\psi(\mathbf{r}) = \sum_{\mathbf{R_n}} A_n \varphi(\mathbf{r} - \mathbf{R_n}), \quad \text{for } L \approx a \text{ in extended (non-localized) states} \tag{3.4}$$

where the coefficient A_n has a random phase and amplitude at each atomic site. For strong

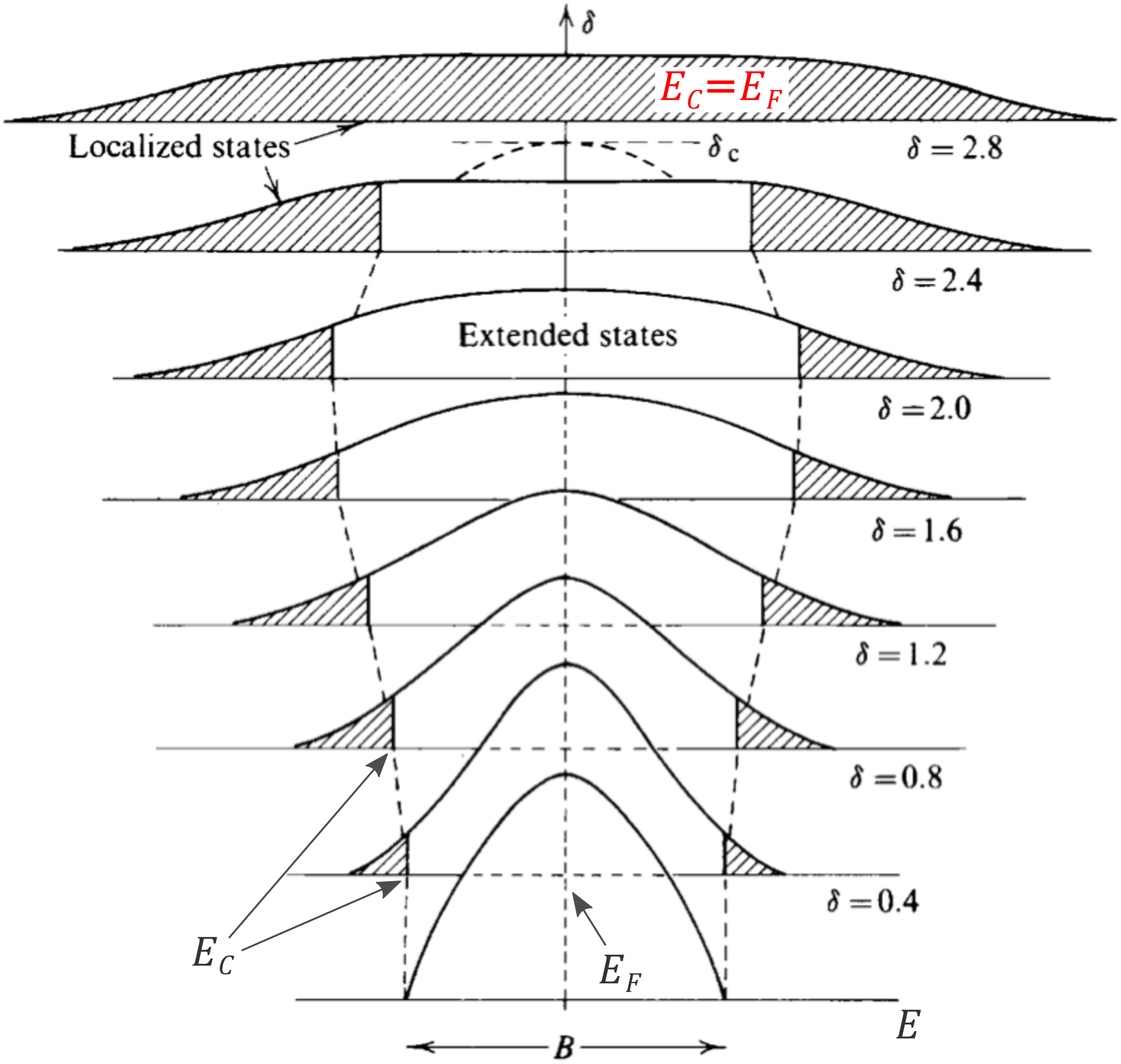

Figure 3.2: Localized states are formed at the band tail as the strength of disorder increases. At the critical value δ_c Anderson criterion is satisfied and all states become localized. From Fig. 9.17 in Ref. [37].

disorder-induced potential fluctuations (i.e., large δ), perturbation of neighbouring wells on the wavefunction of each isolated well is no longer negligible and one would intuitively expect an exponential decay of the wavefunction with distance from the localized site. Cohen *et al* [36] defines a localized state as "one with probability amplitude decreasing exponentially with distance from the centre of localization for sufficiently large disorder." The wavefunction of such localized states is represented as

$$\psi(\mathbf{r}) = e^{-\alpha\mathbf{r}} \sum_{\mathbf{R_n}} A_n \varphi(\mathbf{r} - \mathbf{R_n}), \quad \text{for } L < a \text{ in localized states} \tag{3.5}$$

where α is the rate at which wavefunctions fall off from the centre of localization and increases with increasing disorder.

Finally, given the preceding analysis, the wavefunctions envisaged for the periodic potential and the random potential (with and without localization) are illustrated in Fig. 3.3.

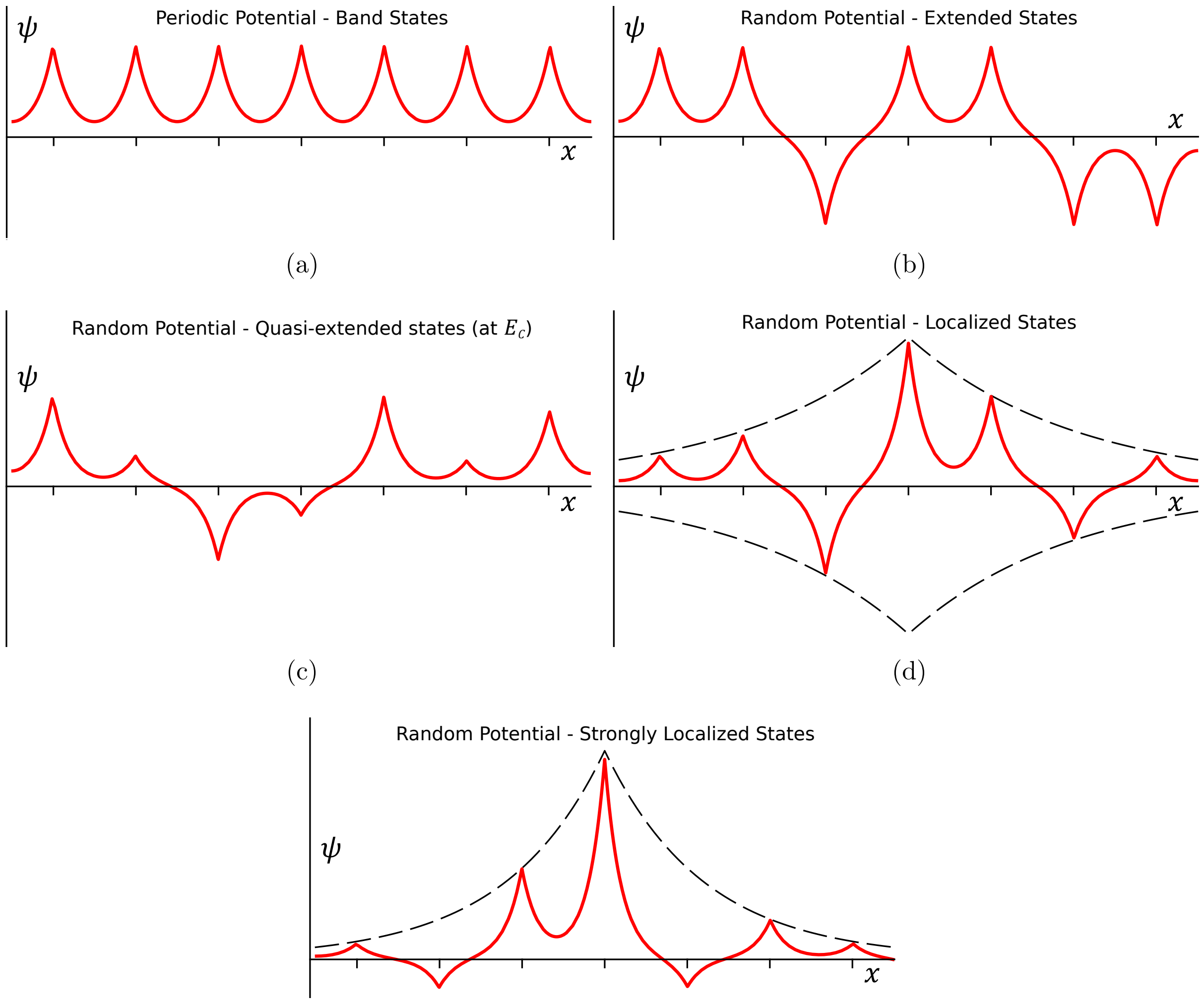

(a) (b) (c) (d) (e)

Figure 3.3: (a) Periodic wavefunction for a crystalline lattice. (b) Extended wavefunction in a random potential for $E > E_C$. (c) Quasi-extended wavefunction for $E \approx E_C$. (d) Localized wavefunction with an exponentially decaying envelope for $E < E_C$. Strongly localized wavefunctions $E \ll E_C$. Adapted from Fig. 2 in Ref. [33].

3.3 Mott-model of Conduction

> *It is curious, therefore, that no one much earlier than my coworkers and I did in Cambridge less than ten years ago seems to have asked the question "how can glass be transparent?".*
>
> *Clues [to the nature of conduction in disordered solids] came from another Leningrad idea due to Ioffe and Regel [28], namely that the mean free path cannot be shorter than the electron wavelength, and from the vastly important paper published by Anderson [29] in 1958, Absence of diffusion in certain random lattices, described in his Nobel lecture this year.*
>
> Sir Nevill Mott, Nobel Lecture [26],
> 10 December, 1977

3.3.1 Minimum metallic conductivity

Figure 3.4a shows the density of states for a typical crystalline metallic system where electron states are occupied by to the Fermi energy, E_F. However, let's consider a *degenerate* gas of electrons in a Gaussian density of states in a metallic Anderson band where the Anderson criterion is not satisfied. Thus, states are extended in the middle of the band and localized in the tail, and the two regions are separated by the mobility edge, E_C, as shown in Fig. 3.4b. In the extended states, the conductivity is due to band transport with finite d.c. conductivity $\sigma_{d.c.}(E)$ at temperature $T = 0$, and in the localized states transport is due to thermally activated hopping where $\sigma_{d.c.}(E)$ vanishes at $T = 0$ [38], [35]. The minimum metallic conductivity occurs at the onset of localization $E = E_C$ and is the smallest non-zero value at $T = 0$ before an abrupt change to zero when $E < E_C$. Note that at absolute zero temperature, the Fermi energy, E_F, is the energy of the highest occupied

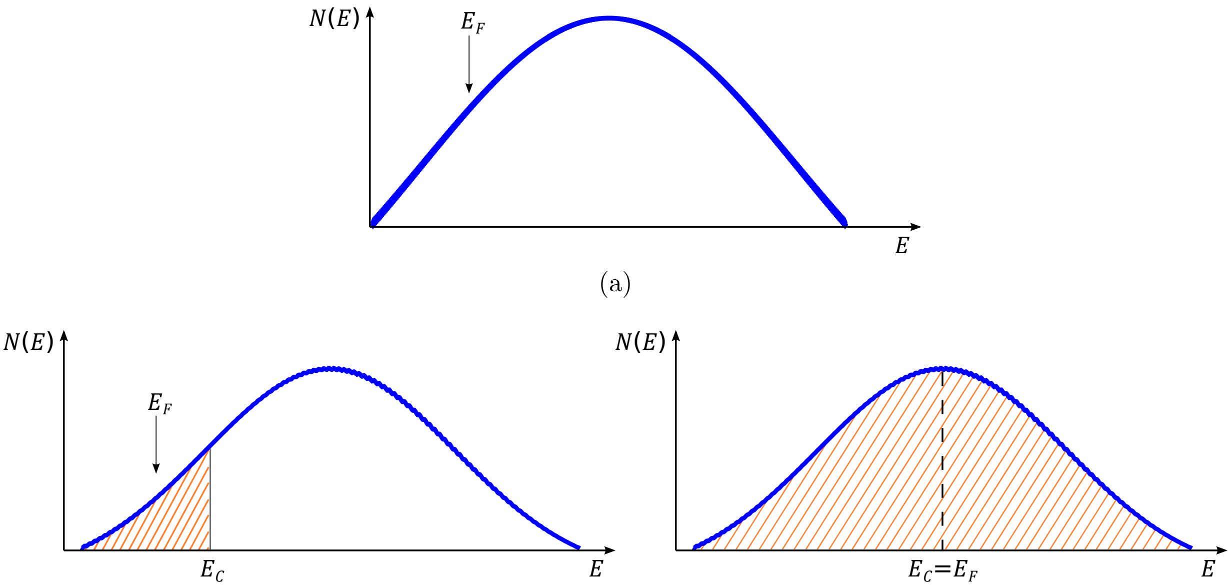

(a)

(b)

(c)

Figure 3.4: (a) Density of states for a crystalline metallic system with electron states occupied up to E_F. Gaussian density of states in an anderson band for (b) $\delta < \delta_c$ and (c) $\delta = \delta_c$. Localized states are shaded. Adapted from Fig. 3 and Fig. 12 in Ref. [35].

quantum state in our metallic system. Similarly, one can calculate the conductivity at the centre of the band while increasing the disorder strength. In that case, the minimum metallic conductivity occurs at the onset of reaching the Anderson criterion where all the states become localized, as shown in Fig. 3.4c.

Figure 3.5 is a plot of conductivity as a function of disorder strength, and is divided into three regimes. In regime (I) the carrier mean-free-path is long ($L > a$) due to weak scattering and carrier wavefunction is similar to that of a periodic potential well (Fig. 3.3a). In regime (II) L approaches a ($L \sim a$) due to increased scattering and carrier wavefunction in extended states loses phase memory along its transport from one atom to the next (Fig. 3.3b). At the onset of reaching the Anderson criterion (i.e., $\delta = \delta_c = 2$), although states are still extended, carrier wavefunction takes the form of Fig. 3.3c and the material experiences its minimum metallic conductivity. Finally, any further increase in the disorder strength beyond δ_c, as is the case in regime (III), causes the carrier wavefunction to be localized (Fig. 3.3d and Fig. 3.3e) and the concept of carrier mean-free-path fades out due to strong scattering ($L < a$) and conductivity drops *discontinuously* to zero. The conductivity equation at $T = 0$ is written as [33], [39]

$$\sigma_{d.c.} = \begin{cases} q^2/6\hbar a\delta^2 & \text{(I) } L > a \\ \pi q^2 B^2/4z\hbar a(B^2 + W^2) & \text{(II) } L \sim a \\ 0 & \text{(III) } L < a \end{cases} \tag{3.6}$$

where q is the electron charge, and z is the atomic coordination number of the material. Note that in regime (II), $\sigma_{d.c.}$ does not decrease much initially because of the term (B^2+W^2) in the denominator, but for large disorder close to δ_c we have $(B^2 + W^2) \approx W^2$. Thus, the minimum metallic conductivity is given as

$$\sigma_{min} = \pi q^2/4z\hbar a\delta_c^2, \quad \text{(II) } \delta = \delta_c. \tag{3.7}$$

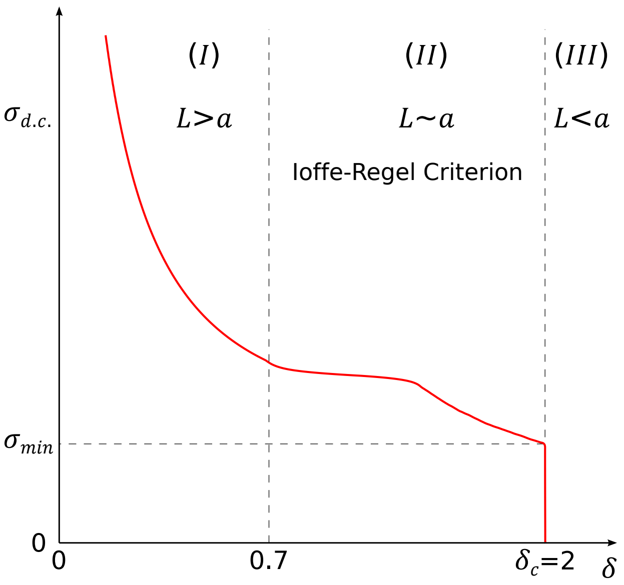

Figure 3.5: Conductivity at $T = 0$ as a function of disorder strength. Adapted from Fig. 3 in Ref. [33].

3.3.2 Metal-insulator (Anderson) transition

Now consider a hypothetical system with the Fermi energy above the mobility edge ($E_F > E_C$). Also characteristic of this system is the possibility to (1) change the Fermi energy E_F by varying the density of electrons, or (2) change the mobility edge E_C by varying the disorder strength, or (3) change both E_F and E_C. If the changes can extend to a degree that $E_F - E_C$ changes sign ($E_F < E_C$), then a metal-insulator (M-I) transition will occur and our metallic system becomes a Fermi glass. Mott called this M-I transition the "Anderson transition" [40].

As described earlier, conduction in our hypothetical system in its initial state (i.e., $E_F > E_C$ and $L > a$) can be explained using weak scattering theory. As the gap between E_F and E_C reduces, scattering increases and we approach the Ioffe-Regel criterion where the carrier mean-free-path becomes comparable to the interatomic spacing ($L \sim a$). We showed that at the onset of reaching the Anderson criterion, the material experiences its minimum metallic conductivity. Now, the question is what happens to the conduction process when the material becomes a Fermi glass with E_F below E_C.

According to Mott, there are two types of conduction processes for carriers in a Fermi glass. As shown schematically in Fig. 3.6a, carriers near the fermi energy can (1) be excited to the extended states near the mobility edge and experience band-like transport, or (2) undergo thermally activated hopping transport [40]. At high temperatures, transport in the extended-states dominates, so that

$$\sigma_{ext} = \sigma_{min} \exp\{-(E_C - E_F)/kT\}. \tag{3.8}$$

In the limit of low temperatures, the conductivity is due to hopping and follows the $T^{1/4}$ law

$$\sigma_{hop} = \sigma_0 \exp\{-B/T^{1/4}\}, \tag{3.9}$$

where the pre-exponential factor $\sigma_0 << \sigma_{min}$ and B is a function of α, the rate at which wavefunctions fall off from the centre of localization, and $N(E_F)$, the density of states at the Fermi energy. Figure 3.6b is a plot of resistivity as a function of $1/T$, parametric in the disorder strength [41], [26], [40].

Examples of such systems that experience the Anderson transition are doped and compensated semiconductors with impurity conduction at low temperatures, and more interestingly, the interface between silicon (Si) and silicon dioxide (SiO_2) in a, for example,

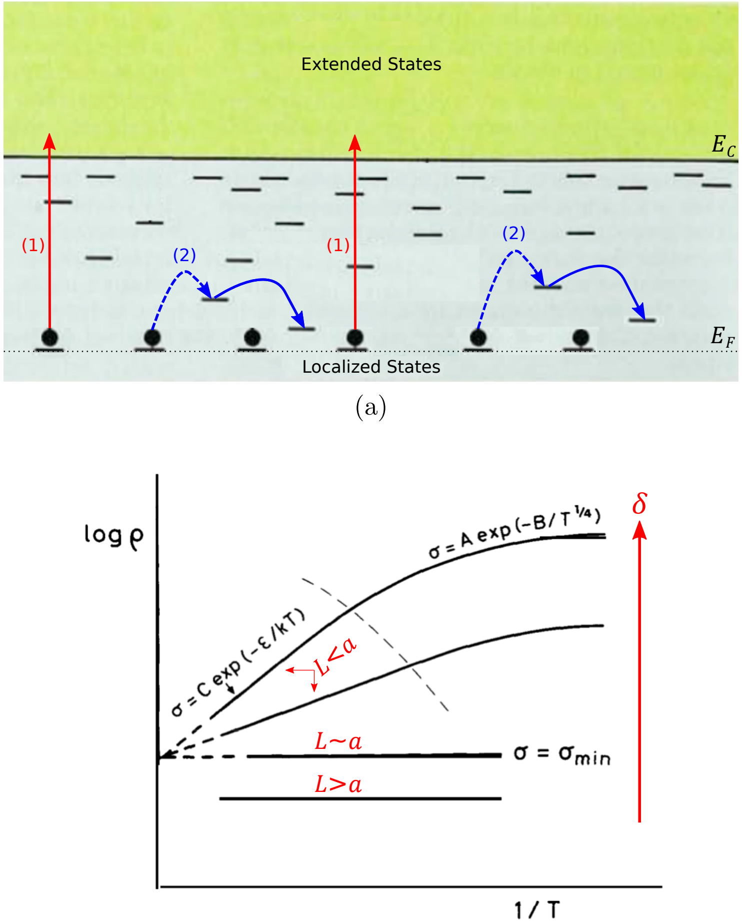

(a)

(b)

Figure 3.6: (a) Schematic diagram of the two conduction mechanisms in a Fermi glass. (b) Resistivity as a function of $1/T$ before and after Anderson transition for increasing disorder strengths (from Fig. 3 in Ref. [40]).

N-channel metal oxide semiconductor (MOS). Inhomogeneities above the inversion layer in a MOS device, caused by a cluster of sodium cations (Na^+) which enter the oxide during device fabrication, result in random potential fluctuations at the Si inversion layer [40].

3.3.3 Conduction in Amorphous Semiconductors

State localization was first introduced in the amorphous semiconductor band model by Cohen, Fritzche, and Ovshinsky [36]. As shown in Fig. 3.7 (left), the CFO model envisaged overlapping localized tails of the conduction and the valence bands where $E_{C,C}$ and $E_{C,V}$ are the energies of their respective mobility edges. In reality, the Mott-model in Fig. 3.7 (right) showed that in most amorphous semiconductors band tails do not overlap and the presence of overlapping Gaussian localized states in the gap, which give rise to a finite density of states at the Fermi energy, is due to defects in the material due to the dangling bonds. A simulated random networks of amorphous silicon or germanium with dangling bonds is shown in Fig. 3.8 [26]. In both models, $E_{C,C} - E_{C,V}$ is defined as the "mobility gap" in amorphous semiconductors.

According to the above Mott-model for the density of states (DoS) in amorphous semiconductors, three types of conduction occur simultaneously. First, carriers may be excited to the extended states to yield non-activated conduction with shallow-trap-limited mobility

$$\sigma_I = \sigma_0 \exp\{-(E_C - E_F)/kT\}. \tag{3.10}$$

where a very crude theoretical estimation yields $\sigma_{min} = \sigma_0 = 200\ \Omega^{-1}\mathrm{cm}^{-1}$. Second, carriers may be excited to the energy E_L above the tail with high localized DoS giving an activated hopping conduction of the form

$$\sigma_{II} = \sigma_1 \exp\{-(E_L - E_F + E_{A1})/kT\}. \tag{3.11}$$

where $\sigma_1/\sigma_0 \sim 1/1000$ and E_{A1} is the activated energy at high temperatures. Third, at very low temperatures, carriers may hop to localized states with energies near the Fermi level and yield activated hopping conduction of the form

$$\sigma_{III} = \sigma_2 F \exp\{-E_{A2}/kT\}. \tag{3.12}$$

where $\sigma_2 \ll \sigma_1$ and E_{A2} is the activated energy at low temperatures and is equal to half the width of the Gaussian defect states. As an example to illustrate activated hopping conduction, Fig. 3.9 shows the transition from σ_{II} at high temperatures with $E_{A1} = 0.43$ eV to σ_{III} at low temperatures with $E_{A1} = 0.06$ eV [42] in a 1 μm Ovonic glass [1].

---

[1] An Ovonic glass is a chalcogenide amorphous/glassy semiconductor with switching properties.

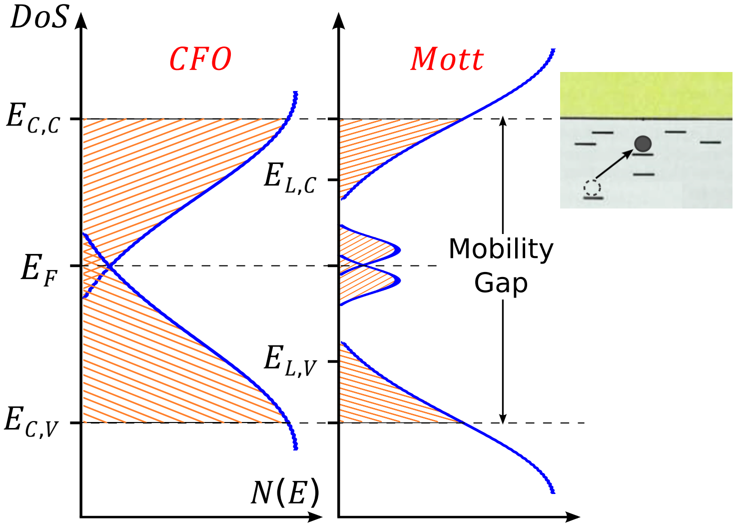

Figure 3.7: (left) Density of states (DoS) in amorphous semiconductors as proposed first by Cohen, Fritzsche, and Ovshinsky (called the CFO model) [36]. (right) Actual DoS in amorphous semiconductors with Gaussian defect states in the gap due to dangling bonds, as proposed by Mott [42], [43]. Localized states are shaded and $E_{C,C}$ and $E_{C,V}$ refer to the mobility edges for the conduction and the valence bands, respectively.

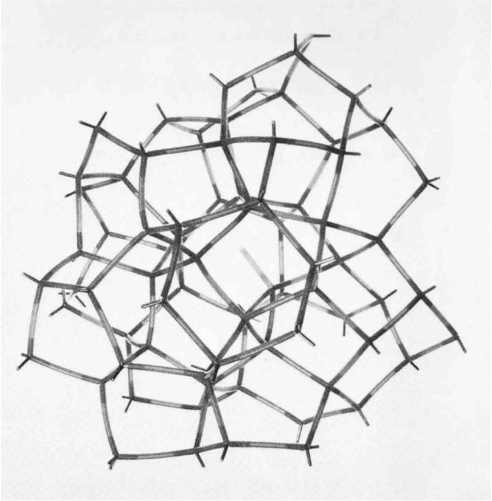

Figure 3.8: Simulated random networks of amorphous silicon or germanium with dangling bonds. From Fig. 7 in Ref. [26].

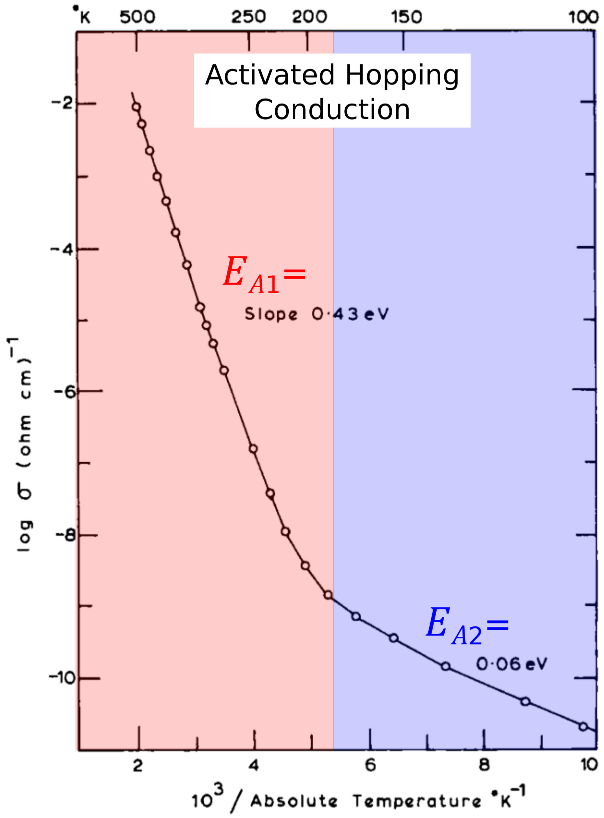

Figure 3.9: Activated hopping conduction in a 1 μm Ovonic glass showing the transition from σ_{II} at high temperatures to σ_{III} at low temperature. From Fig. 5 in Ref. [42].

3.4 Scher-Montroll Universality of Photocurrent

Figure 3.10a shows Gaussian statistics for the transport of a carrier packet inside a non-dispersive medium. Gaussian statistics for the root-mean-square (rms) diffusion, σ_D, and the mean carrier displacement, ℓ, obey time dependencies $\sigma_D \propto t^{1/2}$ and $\ell \propto t$, which yield the well-known relation $\sigma_D/\ell \propto t^{-1/2}$ [44], [45]. However, in many organic and inorganic amorphous semiconductors, the transport statistics are non-Gaussian and show anomalous dispersive properties, as shown in Fig. 3.10b.

The Scher-Montroll (SM) theory of continuous-time random walk (CTRW) for the dynamics of carrier packet transport provided a novel theoretical explanation of anomalous non-Gaussian transit dispersion in disordered solids. The results are known as SM *universality* of photocurrent [44] for dispersive (or non-Gaussian) transports because all plots of $I(t)/I(t_T)$ vs t/t_T collapse into one curve for varying applied electric fields and/or material thicknesses. Thus, the ratio of the rms spread to the mean position of the drifting carrier packet is independent of time, or in another words, σ_D/ℓ = constant. Such universal dispersive photocurrents are indicated as the following algebraic decay functions

$$i(t) \propto \begin{cases} t^{-(1-\alpha)} & t < t_T \\ t^{-(1+\alpha)} & t > t_T \end{cases} , 0 < \alpha < 1 \tag{3.13}$$

In contrast to the time-of-flight transients in Fig. 3.10c for Gaussian packets which are incompatible with SM universality, Fig. 3.10d shows the universal photocurrent plot of Eq. 3.13. As an example, α ≈0.5 for inorganic amorphous Arsenic triselenide (As_2Se_3) and α ≈0.8 for organic poly-N-vinyl carbazole (PVK) polymer [44].

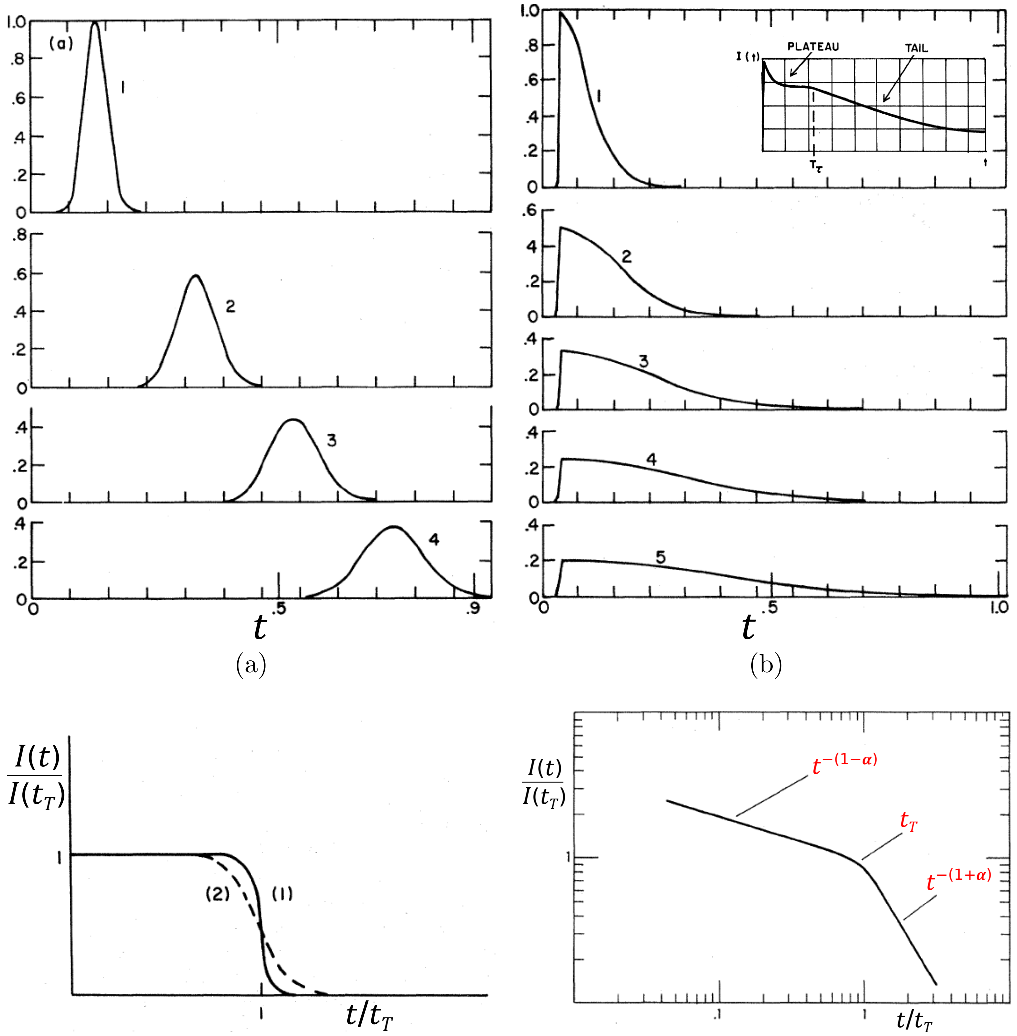

(a) (b)

(c) (d)

Figure 3.10: Spatial charge distribution density of a drifting carrier packet with (a) Gaussian statistics inside a non-dispersive medium and with (b) anomalous non-Gaussian statistics inside a dispersive medium. Normalized TOF transients for a propagating (c) Gaussian and (d) non-Gaussian packets. SM universality is only applicable for non-Gaussian dispersive transport where the ratio of the mean position of the drifting carrier packet to the rms spread is always a constant, and thus, all normalized TOF curves collapse into the same curve as is shown in (d) for varying applied electric fields and/or material thicknesses. In contrast, the plot in (c) shows different curves for varying field because Gaussian transport is incompatible with SM universality of TOF. From figures in Ref. [44].

3.5 Conclusions

We started the discussion in this chapter with the Ioffe-Regel criterion stating that the concept of band theory breaks down for disordered semiconductors with the carrier mean-free-path less than the interatomic spacing. We showed that the basis for understanding conduction in such disordered semiconductors is the Anderson localization indicating that the electron wave function has its largest amplitude at the center of localization and it decreases exponentially with distance, similar to an electron being trapped in an impurity state in a doped crystalline material. We introduced the Mott-model for the density of states with localized conduction and valence band tails (with the critical energy at the mobility edge separating extended and localized states) and overlapping localized Gaussian states in the gap due to dangling bonds. The Mott-model of conduction in amorphous semiconductors was based on three parallel processes: (1) trap-limited conduction in extended states, (2) activated hopping in the localized band tails at higher temperatures, and (3) field-enhanced activated hopping in the localized Gaussian gap states at lower temperatures. Finally, we presented the Gaussian transport process in non-dispersive materials and the anomalous non-Gaussian transport in dispersive materials with Scher-Montroll universality of photocurrent.

Chapter 4

Unipolar Charge Sensing: Theory of Operation

4.1 Introduction

4.1.1 Gas-filled multiwire proportional chamber

> *Multiwire chambers gave rise to further developments in the art of detectors, of which some are highly innovative. Most high-energy physics experiments make use of these methods, but their application has extended to widely differing fields such as biology, medicine, and industrial radiology.*
>
> Georges Charpak, Nobel Lecture [46],
> 8 December, 1992

The oldest type of radiation detectors are based on detecting the direct ionization by the travelling radiation in a gaseous medium. A conventional gas-filled proportional counter has a cylindrical cathode with a fine anode wire positioned along its axis. The detector geometry is such that large electric fields develop around the immediate vicinity of the anode wire, and thus, the electron liberated from the initial ionization will cause *Townsend avalanche* (due to inelastic ionizing collisions) while drifted towards the anode. The gas amplification is linear and the output pulse is proportional to the energy of the incident radiation [47]. The major problem of this detector is its low spatial and temporal resolution. Two-dimensional position sensing is not possible and the timing resolution is a few hundred nanosecond for a detector with 1 cm diameter.

In 1968, the invention of the gas-filled multiwire proportional chamber (MWPC) by Charpak revolutionized the field of radiation detection and showed spatial and temporal resolutions which were orders of magnitude better than those of single-wire cylindrical structures [48], [49], [46]. As illustrated in Fig. 4.1a, the invention was based on placing multiple evenly spaced anode wires in the middle of two cathode planes. Figures 4.1b and 4.1c show, respectively, the equipotential lines and the field strength between the anode and the cathode, which are identical to those of a conventional cylindrical detector. Such a normalized field distribution, where it is relatively low in the drift region and rises sharply to 1 in the immediate vicinity of the collector, is called the *"near-field effect"*. Note that a temporal resolution of 30 ns is obtained with a wire spacing of 2 mm. Figure 4.1d shows a two-dimensional position sensing MWPC with orthogonally segmented cathode planes [50], [51]. The distribution of the avalanche signal on the isolated cathode strips (in both planes) is measured to localize the ionization event using the"centre-of-gravity" techniques. In this design, highly accurate spatial resolution is obtained both along the wire in the y-axis and in the interpolation space between the wires in the x-axis. This technology enabled, for the first time, x-ray and neutron imaging over large areas. The technology was further evolved with the introduction of microstrip gas chambers (MSGC) [52], microgap gas chambers (MGC) [53], micromesh gas chambers (MICROMEGAS) [54], and gas electron multipliers (GEM) [55].

In 1992, Georges Charpak won the Nobel Prize in Physics for his invention of the multiwire proportional chamber [46]. Charpak's invention was considered by the Nobel prize committee as an advanced technological development within basic science, with applications not only in particle physics, but also in medicine, astronomy, and protein crystallography. It was the tenth time in the history of the Nobel prize that the word "invention" was used in the award citation in physics. It was also the last time that the Nobel prize in physics was awarded to a single person.

4.1.2 Solid-state detectors

In most applications, however, the use of a solid detection medium is preferable because solid densities are about three orders-of-magnitude greater than gas, and thus, they can yield much smaller detector dimensions with unsurpassed spatial and temporal resolution. The problem is that amorphous solids, which are easier and less expensive to develop over large area than single crystalline solids, have been ruled out as a viable radiation detection medium because of low carrier mobilities and transit-time-limited photoresponse. High radiation sensitivity requires high quantum efficiency and high charge collection efficiency.

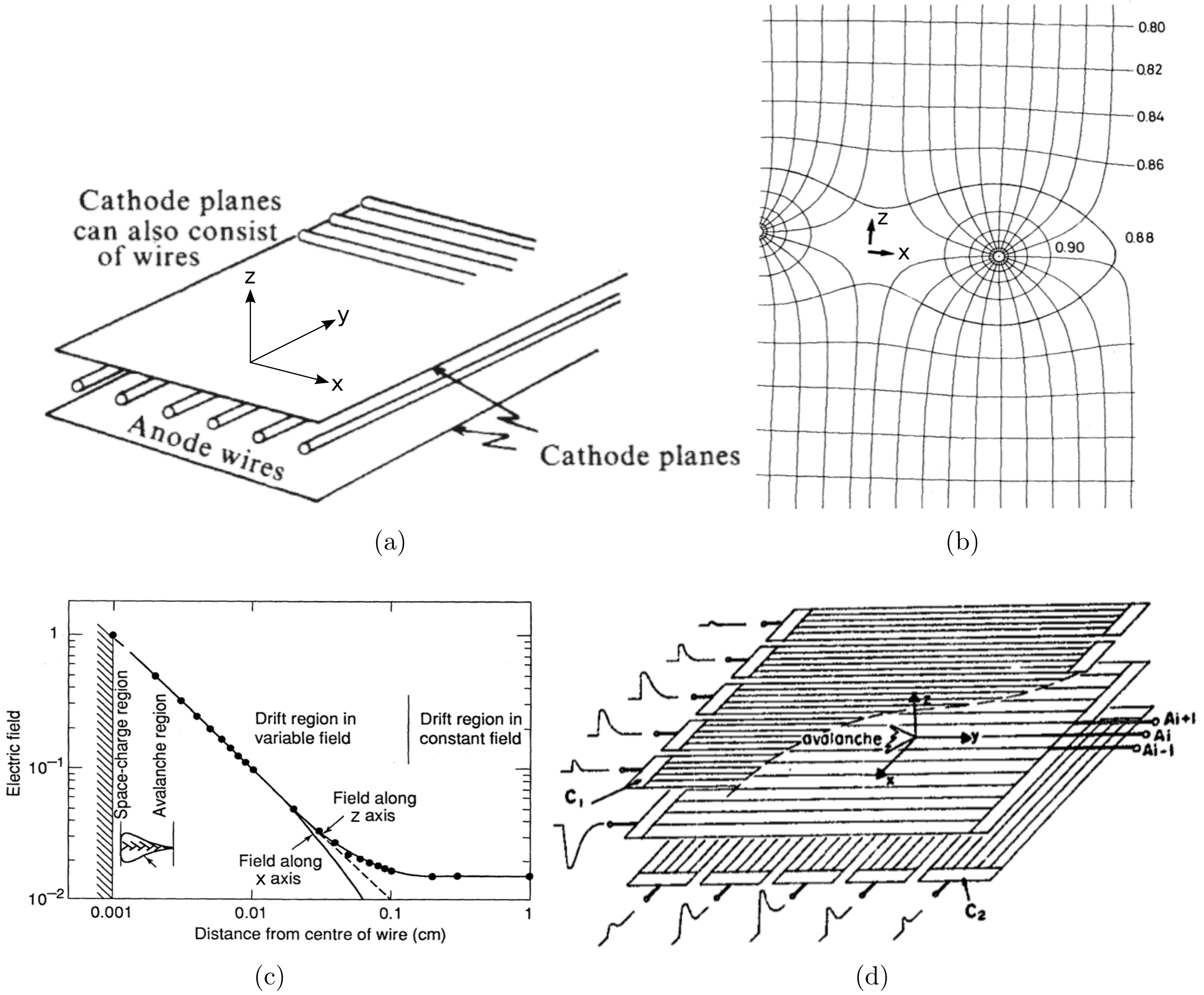

(a) (b)

(c) (d)

Figure 4.1: (a) Schematic of a multiwire proportional chamber (MWPC) invented by Georges Charpak in 1968. (b) Equipotential lines close to the thin anode wire. (c) Electric field strength between the anode wire and one of the cathode planes. Schematic of a MWPC with two orthogonally segmented cathode planes for two-dimensional position sensing for radiation imaging. From Ref. [51] and Ref. [46].

A necessary condition for complete charge collection is that the carrier lifetime exceeds the transit time across the detector thickness. In amorphous solids, charge transport properties can be substantially different for holes and electrons and this condition is generally met by only one type of carrier that has a higher mobility-lifetime product.

The canonical method for transport studies of highly resistive, low mobility solids such as amorphous selenium is the time-of-flight (TOF) transient photoconductivity experiment [56]. In TOF experiments, a sheet of carriers is injected with an optical impulse-like excitation from the top surface into the photoconductor and the transport of photoinduced carriers across the bulk is studied under a certain applied field. Transport of carriers in disordered solids is either *dispersive* or *non-dispersive*. In dispersive (or non-Gaussian) transport, Scher-Montroll (SM) *universality* of the photocurrent is applicable and the propagating carrier packet experiences highly incoherent broadening, where fluctuations of bulk parameters extend into the time range of transit time and cause the carrier to be immobilized for a long period of time [44], [57]. This anomalous stochastic transport can typically be avoided by proper selection of operating temperature, applied electric field, and material morphology. Our study, however, only considers materials with non-dispersive Markoffian transport, where Scher-Montroll (SM) *universality* of the photocurrent is not applicable and the propagating carrier packet experiences broadening which is described by Gaussian statistics [44], where the position of the peak of carrier distribution coincides with its spatial mean.

In this chapter, we investigate the deteriorating effect of poor carrier transport on the temporal resolution and the counting rate of an amorphous selenium (a-Se) spectrometer. We propose a modified photoconductive device structure, based on unipolar charge sensing, for circumventing the problem of poor carrier transport in not just a-Se, but also any solid with any degree of disorder. Using the new device, we show that the temporal resolution can be improved substantially and reach the intrinsic physical limit set by the spatial dispersion of the photoinduced carrier packets.

4.2 Selenium Spectrometer

4.2.1 Experimental setup for single photon counting

To characterize the operation of amorphous selenium (a-Se) films as radiation detectors in photon-counting mode, we used the experimental spectroscopy setup shown with schematic in Fig. 4.2 and with actual photograph in Fig. 4.3 [58]. The unique feature of this setup is the generation of monoenergetic x-rays from an x-ray tube. Polyenergetic photons are incident on a fluorescent elemental target and cause emission of characteristic x-rays due to K-shell fluorescence, and the energy of this secondary monoenergetic beam can be increased with higher atomic number targets [59]. The selenium detector, with its properties summarized in Table 4.1, was biased with the low-noise ORTEC459 high-voltage power supply and the induced ionization current pulses were integrated with a low-noise cooled AMPTEK-A250CF charge sensitive preamplifier. The collected charge from a single ionization event was amplified and filtered with the APTEC6300 semi-Gaussian unipolar shaper. In standard spectroscopy experiments, the shaping time τ_s of the pulse shaper is set substantially larger than the transit time of the slower carrier type to guarantee complete charge collection and eliminate ballistic deficit. Thus, performance trade-off is

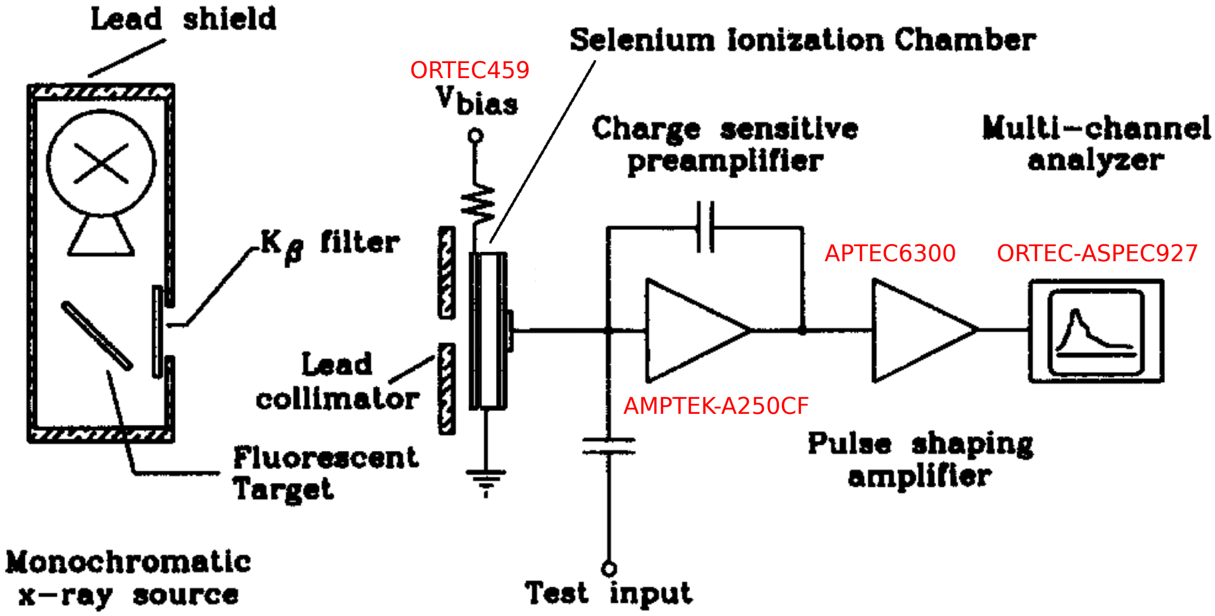

Figure 4.2: Schematic of the x-ray spectrometer using a-Se as the radiation detector (from Fig. 3 in Ref. [58]).

Table 4.1: Typical carrier mobilities for amorphous selenium films. Measurements were done at an applied external field of 10 V/μm for a film thickness of 150 μm. Data is extracted from Table I in Ref. [58].

e^-/h^+ Mobility μ (cm^2/Vs)	e^-/h^+ Lifetime τ (μs)	Film Thickness L (μm)	Field F (V/μm)	e^-/h^+ Transit Time t_T (μs)
0.002/0.12	300/50	150	10	75/1.25

between photon count rate, limited by the shaping time, and charge collection efficiency. As a reasonable compromise and due to low electron mobility in a-Se (see Fig. 4.4), we chose a shaping time of 60 μs, which was the largest selection available on the shaper and was approximately equal to the electron transit time at $F = 10$ V/μm. The shaped signal was processed by the ORTEC-ASPEC927 multi-channel analyzer (MCA).

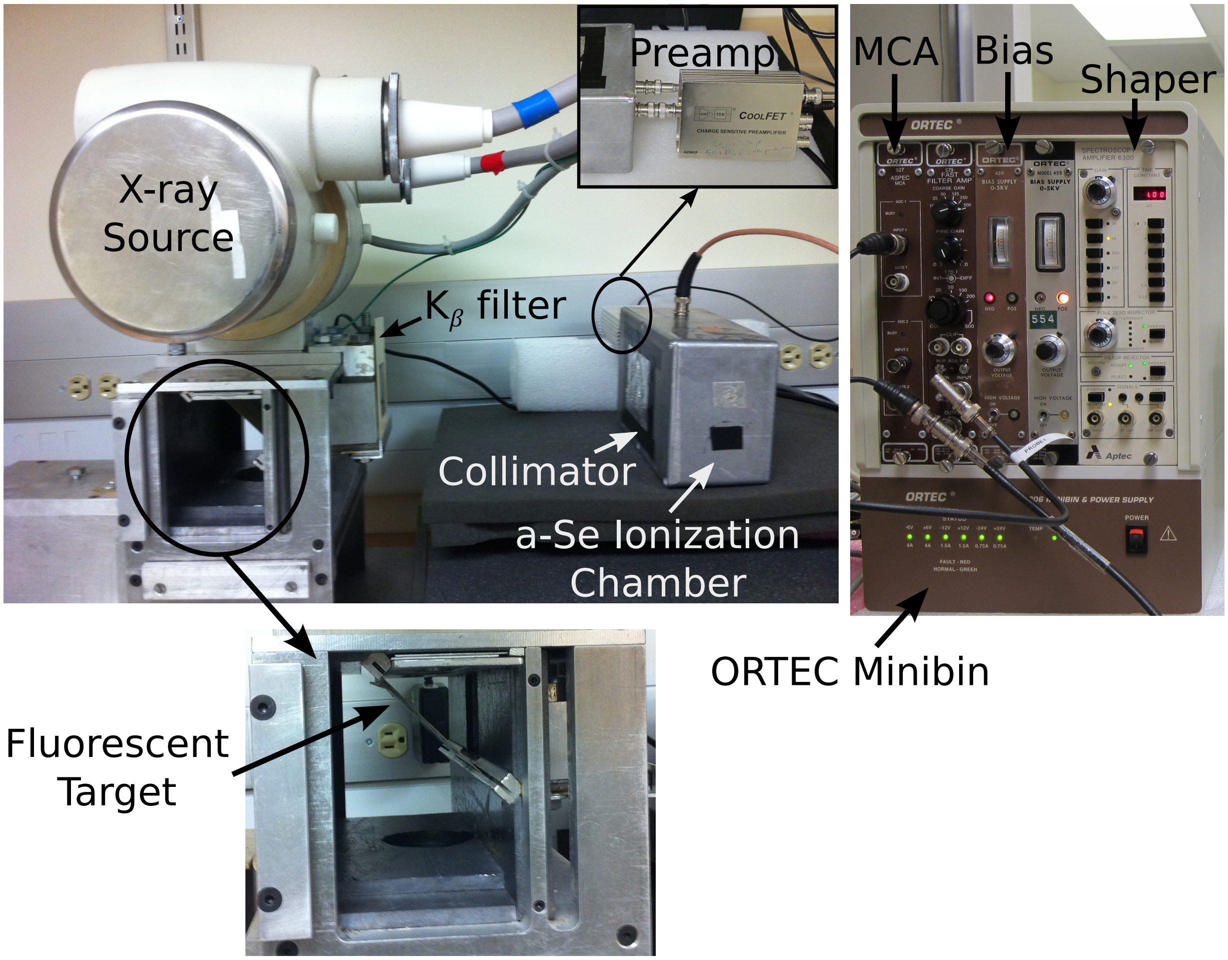

Figure 4.3: Photographs of the experimental setup shown with schematic in Fig. 4.2 (courtesy of Rowlands' group at TBRRI).

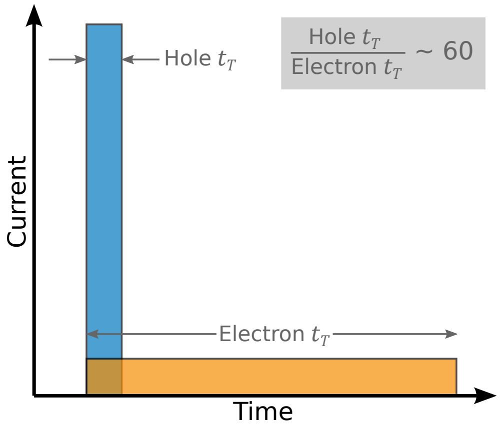

Figure 4.4: Idealized current pulses due to a single carrier drift across a detector thickness. The response is for a typical amorphous photoconductor where the charge transport for one carrier type (e.g., hole) is superior to that of the other carrier type (e.g., electron). For amorphous selenium, the transit time of holes is ~60 times higher than that of electrons.

4.2.2 Spectroscopy results from characteristic x-ray fluorescence

The raw pulse-height spectra for a 74 KeV monoenergetic beam are shown in Fig. 4.5. Table 4.2 shows spectral information of the results in Fig. 4.5a and indicates a sublinear field dependence of the mean signal $S \propto F^{2/3}$ (and consequently an inverse field dependence of the conversion gain $W_{\pm} \propto F^{-2/3}$), as expected from previous work [60], [58]. The spectral widths, represented in full width at half-maximum (FWHM), were corrected for the measured readout electronic noise (i.e., width of the pulser in Fig. 4.5a), the signal shot noise (i.e., $S^{1/2}$ in root mean square or rms), and the uncertainty associated with the energy of the fluorescent source (i.e., ~8% of the mean signal in FWHM). The much larger spectral width at higher fields is attributed to increased leakage shot noise due to substantially higher charge injection at the selenium contacts.

To show the effect of shaping time on charge collection efficiency, we reduced the shaping

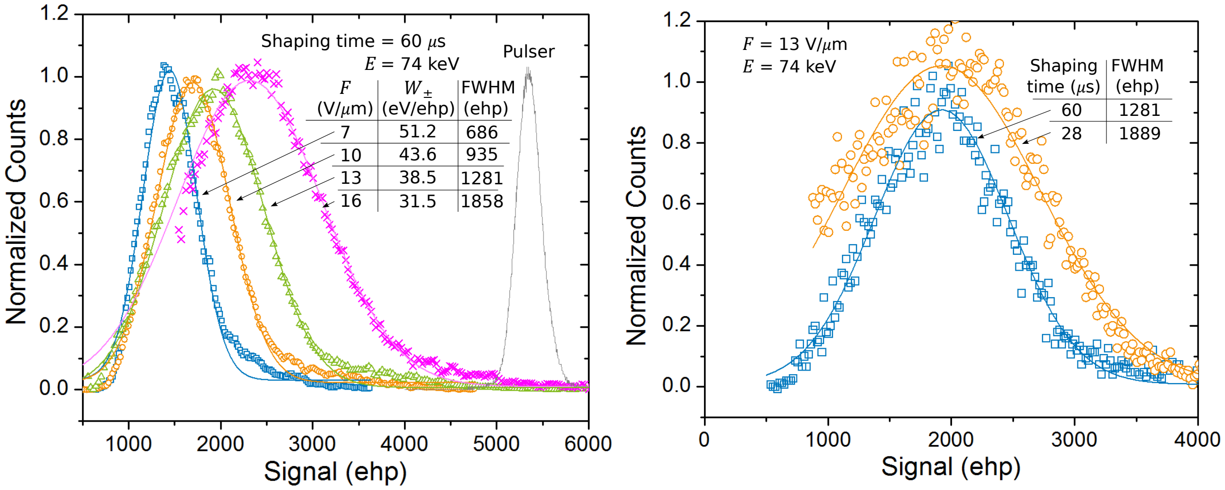

(a) (b)

Figure 4.5: (a) Monoenergetic spectra of a-Se film at E =74 keV, parametric in F. (b) Spectroscopy results showing larger FWHM at smaller shaping time due to incomplete charge collection.

Table 4.2: Tabulated results of the spectra in Fig. 4.5a.

Field, F (V/μm)	Mean Signal, S (ehp)	Conversion Gain, $W_{\pm}$ (eV/ehp)	Spectral Width (ehp FWHM)	Corrected Width (ehp FWHM)
7	1445	51.2	686	588
10	1697	43.6	935	863
13	1922	38.5	1281	1226
16	2349	31.5	1858	1817

time while keeping the electric field constant at $F = 13$ V/μm. As seen in Fig. 4.5b, the shorter shaping time of 28 μs had a detrimental effect on the spectral width with a FWHM that was 1.5 times larger than that of the longer shaping time (i.e., 60 μs). This extra noise was due to incomplete charge collection for the portion of the induced signal due to the movement of slow-mobility electrons in a-Se.

4.2.3 Photon count-rate

Using the $CR-(RC)^3$ model for our semi-Gaussian pulse shaper, the peaking time τ_p is equal to $2.2\tau_s$ and the pulse width τ_w is approximately $6\tau_s$ [61]. Assuming Poisson distribution density for the incident x-ray beam, the probability of photon pileup p_p during τ_w is

$$p_p = 1 - \exp(-r_c \tau_w). \tag{4.1}$$

Thus, the maximum count rate R_c for any acceptable pileup ratio during a pulse width is given as

$$R_c = -\frac{\ln(1-p_p)}{\tau_w} = -\frac{\ln(1-p_p)}{6\tau_s}. \tag{4.2}$$

For $\tau_s = 60\ \mu s$ and 20% probability of pileup, the selenium count-rate is only ~600 quanta/s. Let's now calculate the x-ray fluence given the entrance exposure X [1]

$$\zeta(\bar{E}) = \frac{5.43 \times 10^5 X}{\bar{E}(\mu(\bar{E})/\rho)_{\text{air}}}, \tag{4.3}$$

where $\zeta(\bar{E})$ is in units of photons/mm^2, X is in units of mR, $\bar{E}$ is the average energy of the incident x-ray in units of keV, and $(\mu(\bar{E})/\rho)_{\text{air}}$ is the mass energy absorption coefficient of air in units of cm^2/g. Thus, the rate of photons R_i incident on a radiation detector during an exposure time t_X is calculated to be

$$R_i = \frac{\zeta(\bar{E}) A \exp\{-\alpha(\bar{E}) d\}}{t_X}, \tag{4.4}$$

where A is the pixel area, and $\alpha(\bar{E})$ and d are the linear attenuation coefficient and thickness of the breast tissue, respectively. For mammography tomosynthesis, the average exposure per image can be as high as 30 mR with 0.1 s exposure time [62]. For a pixel area of 0.15 mm^2 and a 4.5 cm breast thickness, the calculation yields an incident photon rate of ∼50,000 quanta/s.

This incident photon rate (i.e., ∼50,000 quanta/s) far exceeds the maximum count rate (i.e., ∼600 quanta/s) of a selenium-based ionization chamber. In the next section (section 4.3), we propose a modified photoconductive device structure, based on unipolar charge sensing, to substantially improve the temporal resolution and increase the photon count-rate.

4.3 Unipolar Charge Sensing

Several methods have been proposed to circumvent the problem of poor carrier mobility in photoconductors, which add complexity to the readout circuit or the physical detector structure or both. The first group of methods is purely based on electronic readout techniques and is only applicable to photon counting mode of operation. These methods are pulse-shape discrimination and pulse correction [63], [64]. Pulse-shape discrimination improves energy resolution by selecting signals with fast risetimes [63], but it dramatically degrades detection efficiency (or sensitivity) because it rejects valid photons based on the amplitude of the shaped signal. Pulse correction (or charge-loss compensation) is based on the generalization that the photopeak shifts linearly towards lower energies for longer signal rise-times. Thus, by using electronic techniques, it may be possible to correct for incomplete charge collection due to low-mobility carriers and resolve for the actual full-energy signal amplitude [64]. Although this correction method improves the photopeak efficiency considerably, the photopeak shift may not correspond linearly to the increase in signal rise-times, especially for amorphous solids where the adverse effect of inhomogeneity in electron/hole mobility, field distribution, trapping and recombination of carriers cannot be neglected. As such, the enhanced readout technique, which requires sophisticated electronic circuitry, does not present a viable solution for large area radiation imaging.

Conventionally, a planar photoconductor material is fitted between two contacts to form a sandwich cell: one is the drift electrode that is kept at a certain potential, V_D, with proper polarity and magnitude, and the second is the collecting electrode (or the collector) that is generally biased at zero potential and connects to the readout electronics for signal capture. To circumvent the problems that originate from poor bulk transport properties in disordered solids, we propose the decoupling of the radiation absorbing photoconductor from the collector. In bipolar solids (such as chalcogenide glass amorphous selenium), where charge induction is due to the drift of both electrons and holes in a conventional planar device, this decoupling has the added advantage of sensing only the carrier type with a higher mobility-lifetime product (i.e., the primary carrier) and providing insensitivity of the collector to the transport properties of the slower carrier type. Such localized preferential sensing of primary carriers, which is also referred to as unipolar (or single-polarity) charge sensing, can be implemented by (1) proper potential biasing of the sandwich electrodes to drift primary carriers towards the collector, and (2) establishing the *near-field effect* [1] in

---

[1] The word "field" implies the *weighting field* which in some special cases (e.g., the cylindrical proportional counter, or the MWPC) has the same distribution as the actual applied field. The concept of weighting field is explained in the next section (section 4.3.1).

the immediate vicinity of the collector. The near-field effect can be established directly using (i) the hemispherical detector structure [65], or (ii) the small-pixel geometry [66], or (iii) the electrostatic shielding technique [67], and indirectly using (iv) the coplanar pixel electrodes [68], [69].

The hemispherical detector structure achieves unipolar charge sensing by introducing a logarithmic field inside the detector to collect high-mobility carriers and erase the collection of slow ones [65]. This detector structure is challenging to realize (especially for pixel array detectors), the sensitive volume is less than that of a planar detector, and most importantly, the large non-uniform electric field distribution causes severe ballistic deficit. Another method is to use interdigitated coplanar electrodes with two preamplifiers and a subtraction circuit as the pixel readout [69]. The disadvantages with this technique are the stripped collector design with two distinct output lines per pixel, and the additional readout noise and complexity associated with the second preamplifier and the subtraction circuit. A more preferable technique, which has shown to be especially useful for Cadmium Zinc Telluride (CZT) detectors, is based on the small pixel geometry for planar detector structures, which does not require additional electronic setup for signal processing. The near-field effect is established for a pixel pitch p that is smaller than the detector thickness L. For very small pixels (i.e., $p < 0.1L$), and with proper biasing of the electrodes, the near-field effect is very strong and collected ionization signal becomes almost independent of photon interaction depth and slower carrier motion [66]. Such effect, however, is not strong for existing large area direct conversion photoconductors because of the relatively thin bulk layer compared to the pixel pitch. For example, commercial amorphous selenium (a-Se) mammography panels have a photoconductive layer thickness of 200 μm and a pixel pitch of 85 μm, and thus, experience a weak near-field effect [70].

To achieve the same strong near-field effect for larger pixels, we propose the use of a conductive grid electrode between the anode and the cathode within the detector material [71], [17]. This technique was first proposed by Frisch to solve the trapping effect of positive ions in conventional gas detectors [67]. An illustration of the Frisch grid is shown in Fig. 4.6. The grid establishes an electrostatic shield so as to eliminate charge induction on the collector due to the movement of carriers inside the interaction region. Only after the desired carriers (e.g., holes for a-Se) have passed the grid and entered the detection region is the signal induced on the collector and detected by the readout electronics. Thus, by placing the grid as close to the collector as possible, and with proper biasing of the electrodes and the grid, we can substantially shorten signal risetime and eliminate depth dependent signal variations. Also, the signal induced on the collector becomes insensitive to the movement, trapping and release of the slower carriers (e.g., electrons for a-Se).

In this section, analytical expressions are derived for the operation of unipolar charge-sensing solid-state photoconductors with an integrated electrostatic shield.

4.3.1 Concept of weighting potential

In the early days of vacuum tube techniques, the instantaneous current on any electrode was considered to be proportional to the total number of electrons received by that electrode. This low-frequency concept was discarded soon after the tubes were capable of operating at much higher frequencies where the transit time of electrons across a tube became comparable to the systems operating period. Measurements showed that current

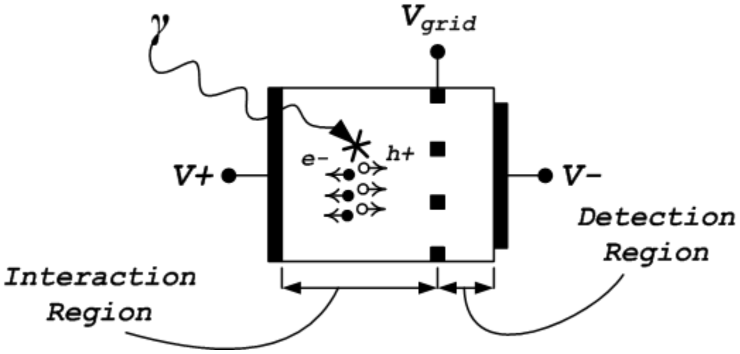

Figure 4.6: The Frisch grid inside a solid-state radiation detector. Faster carriers (e.g., holes in a-Se) drift from the interaction region into the detection region, at which charge is induced on the collector only due to the movement of faster carriers from the grid towards the collector.

is induced in the collector circuit while an electron was still moving towards the positive electrode. Later, the correct concept was first qualitatively presented by Shockley [72] and then mathematically proved by Ramo [73] for the case of charge induction on any electrode due to a single electron motion in a vacuum tube. They showed that the computation of the induced current I_i on an electrode must consider the instantaneous change in the electrostatic flux terminating on that electrode

$$I_i = q\vec{v} \cdot \vec{F_W} \tag{4.5}$$

where q is the charge of an electron, $\vec{v}$ is the instantaneous velocity vector, and $\vec{F_W}$ is the weighting field vector under the following conditions: 1) no space charge, 2) corresponding collecting electrode raised to unit potential, 3) all other electrodes grounded. The induced charge Q_i on the electrode due to a single carrier motion is also given as

$$Q_i = qV_W \tag{4.6}$$

where V_W is the weighting potential under identical conditions. The unit for the weighting field is m^{-1} and the weighting potential is dimensionless. The Schockley-Ramo theorem was initially solved for vacuum tubes and ionization chambers but was later extended to semiconductors with the presence of space-charge [74], [75].

4.3.2 Concept of time-differential photoresponse

Let's consider a photoconductive material within which a single drifting excess electron is contained. Conventionally, a planar photoconductor structure is fitted between two contacts to form a sandwich cell: one is the drift electrode that is kept at a certain potential V_D with proper polarity and magnitude, and the second is the collecting electrode (or the collector) that is generally biased at zero potential and connects to the readout electronics for signal capture. The weighting potential for this device is zero at the common electrode and rises linearly to one at the collector (dashed line in Fig. 4.7). Such a distribution means that the collector is sensitive to real-time bulk transport, and thus, photoresponse is limited by the carrier transit-time t_T across the photodetector thickness L (top inset plot in Fig. 4.7)

$$I_{i1}(t) = \frac{q}{t_T}(H(t) - H(t - t_T)) \tag{4.7}$$

where $H(t)$ is the Heaviside step function. Equation 4.7, with its well-defined plateau, assumes: (1) medium homogeneity, (2) coherent carrier drift with non-dispersive Gaussian transport properties, (3) homogeneous field distribution, (4) $RC \ll t_T \ll \tau_D$, and (5) $t_T \ll \tau_{rel}$, where RC is the time constant of the readout circuit, τ_D is the deep-trapping lifetime, and τ_{rel} is the dielectric relaxation time [76], [77].

Now consider a new device with its weighting potential at zero everywhere in the bulk except for a very small region near the collector where it rises sharply to one (solid line in Fig. 4.7). The induced photocurrent due to a single carrier drift is an impulse (bottom inset plot in Fig. 4.7)

$$I_{i2}(t) = q\delta(t - t_T) \propto \frac{\mathrm{d}}{\mathrm{d}t} I_{i1}(t)\bigg|_{t=t_T} \tag{4.8}$$

where $\delta(t)$ is the impulse function. In this case, the collector is completely insensitive to bulk event times of the drifting excess carrier and photoresponse is independent of photoconductor material (whether single crystalline or disordered, organic or inorganic) and its carrier transport mechanism (whether coherent or incoherent drift via band transport, multiple-trapping, or hopping). Note that the shape of I_{i2} is the time-derivative of I_{i1} at t_T and that response time at the collector is only limited by the overall rise time of the readout electronic equipment. The only exception to Eq. 4.8 is if the photoconductor material is disordered with highly incoherent and dispersive (non-Gaussian) transport properties where fluctuations of bulk parameters extend into the time range of t_T and cause the carrier to be immobilized for a long period of time [44], [57]. This anomalous stochastic transport can typically be avoided by proper selection of operating temperature, applied electric field, and material morphology.

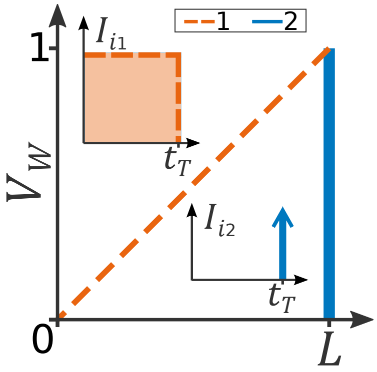

Figure 4.7: A: Weighting potential distributions for the conventional planar (dashed line) and the new hypothetical (solid line) detectors. The two insets show the induced photocurrent due to a single excess carrier drift.

4.3.3 Theoretical performance improvement: in orders of magnitude

As discussed earlier, to circumvent the problems that originate from poor bulk transport properties in disordered solids, one must use the new device with its modified V_W distribution by decoupling the radiation absorbing photoconductor from the collector. In bipolar solids (such as chalcogenide glass amorphous selenium), where charge induction is due to the drift of both electrons and holes in a conventional planar device, this decoupling has the added advantage of sensing only the carrier type with a higher mobility-lifetime product (i.e., the primary carrier) and providing insensitivity of the collector to the transport properties of the slower carrier type. To realize unipolar charge sensing, we proposed an implementation based on the following criteria: (1) proper potential biasing of the sandwich electrodes to drift primary carriers towards the collector, and (2) establishing a strong near-field effect in the immediate vicinity of the collector using a conductive electrostatic

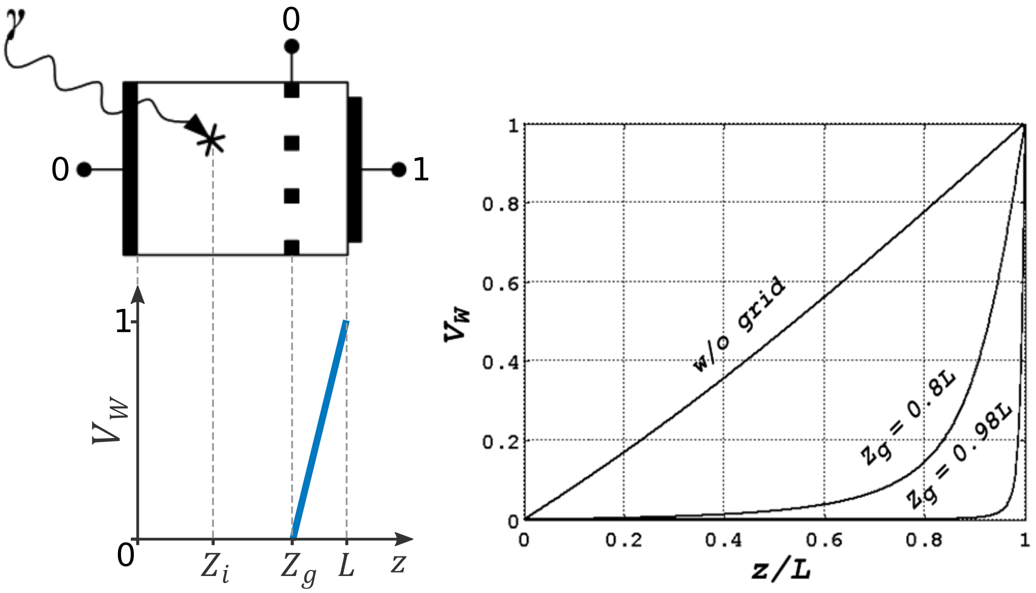

(a) (b)

Figure 4.8: Weighting potential distributions for the three-terminal unipolar device where the shielding grid is at $z = Z_g$. Weighting potentials are simulated by setting non-collecting electrodes (i.e., the high-voltage and the grid) to zero and the collector to unity. The (a) ideal and (b) simulated distributions are shown.

shield [67]. For such a detector, the weighting potential is zero in the interaction region and rises linearly to one in the detection region, as illustrated in Fig. 4.8a. The location of the intermediate shielding grid Z_g determines the boundary between the two regions. Figure 4.8b shows the simulation results of a more practical scenario where the finite gap between the evenly spaced grids has caused a slight rise in V_W in the interaction region. The smaller the gap and the closer the shielding grid to the collector, the closer is our unipolar detector to the ideal impulse response of Fig. 4.7.

The effective mobility of carriers in disordered solid-state detectors is substantially different for holes and electrons. In addition, trapping effects may result in schubweg limited charge transport and reduce charge collection efficiency. Thus, the temporal shape of the collected charge $Q_c(t)$ when a single photon is incident on the detector depends on the interaction depth Z_i. The electron and hole components of the collected charge is given below with the assumption that higher mobility carriers drift towards the collector

$$Q_{c+} = \begin{cases} q[V_W(\mu_+ Ft + Z_i) - V_W(Z_i)] \exp(-t/\tau_+) \ , & 0 \le t \le (L - Z_i)/\mu_+ F \\ q[V_W(L) - V_W(Z_i)] \exp\{-(L - Z_i)/\mu_+ \tau_+ F\} \ , & t > (L - Z_i)/\mu_+ F \\ 0 \ , & t < 0 \end{cases} \tag{4.9}$$

$$Q_{c-} = \begin{cases} q[V_W(Z_i) - V_W(Z_i - \mu_- Ft)] \exp(-t/\tau_-) \ , & 0 \le t \le Z_i/\mu_- F \\ qV_W(Z_i) \exp(-Z_i/\mu_- \tau_- F) \ , & t > Z_i/\mu_- F \\ 0 \ , & t < 0 \end{cases} \tag{4.10}$$

where subscripts +/− designate the type of carrier with higher/lower mobility μ depending on the photoconductive material (e.g., holes/electrons for a-Se) and τ is the carrier lifetime before it becomes immobilized by trapping in deep-trap states.

Figure 4.9 depicts the collected charge from a single photon interaction inside a-Se, with its hole and electron components given in Eq. 4.9 and Eq. 4.10, respectively. Results are simulated at $F = 13$ V/μm for varying photon interaction depths and according to the detector parameters summarized in Table 4.1. We observe from Fig. 4.9a that the magnitude of the collected charge for a conventional planar detector (i.e., without the shielding grid) is highly depth dependent during hole transit time, and thus, for nearly complete charge collection, the shaping time must be set according to the transit time of electrons. As shown in Fig. 4.9b and Fig. 4.9c, however, unipolar devices (with their weighting potentials shown in Fig. 4.8b) have a substantially reduced signal risetime due to the strong near field effect created by the shielding grid at Z_g. Note that the risetime improvement is twofold. First, the collector is mostly insensitive to the low-mobility electrons, and second, charge induction is due to the drift of holes only in the detection region between the grid and the collector. Thus, the new minimum value for the shaping time τ_{s2} can be set equal to the transit time of the higher mobility carriers in the detection region, and not across the photoconductor bulk

$$\tau_{s2} \geq \frac{L - Z_g}{\mu_+ F} \tag{4.11}$$

Recall from section 4.2.3 that for the conventional planar selenium spectrometer, with *electron-transit-time-limited* photoresponse, the photon count-rate was only ~ 600 quanta/s at $\tau_s = 60$ μs and $p_p = 0.2$. However, using the new shaping time τ_{s2} in Eq. 4.2, the maximum count-rate achieved with the unipolar devices are 1.5×10^5 and 1.5×10^6 quanta/s for Z_g equal to $0.8L$ and $0.98L$, respectively. Thus, the performance improvement factor f in signal risetime, and consequently photon count-rate, is in orders of magnitude

$$f = \left(\frac{\mu_+}{\mu_-}\right)\left(\frac{L}{L - Z_g}\right) \tag{4.12}$$

Depicting the theoretical performance improvement in Fig. 4.10 and knowing that f cannot increase indefinitely, one must ask the question: "what is the intrinsic physical limit for the temporal resolution of a unipolar device?"

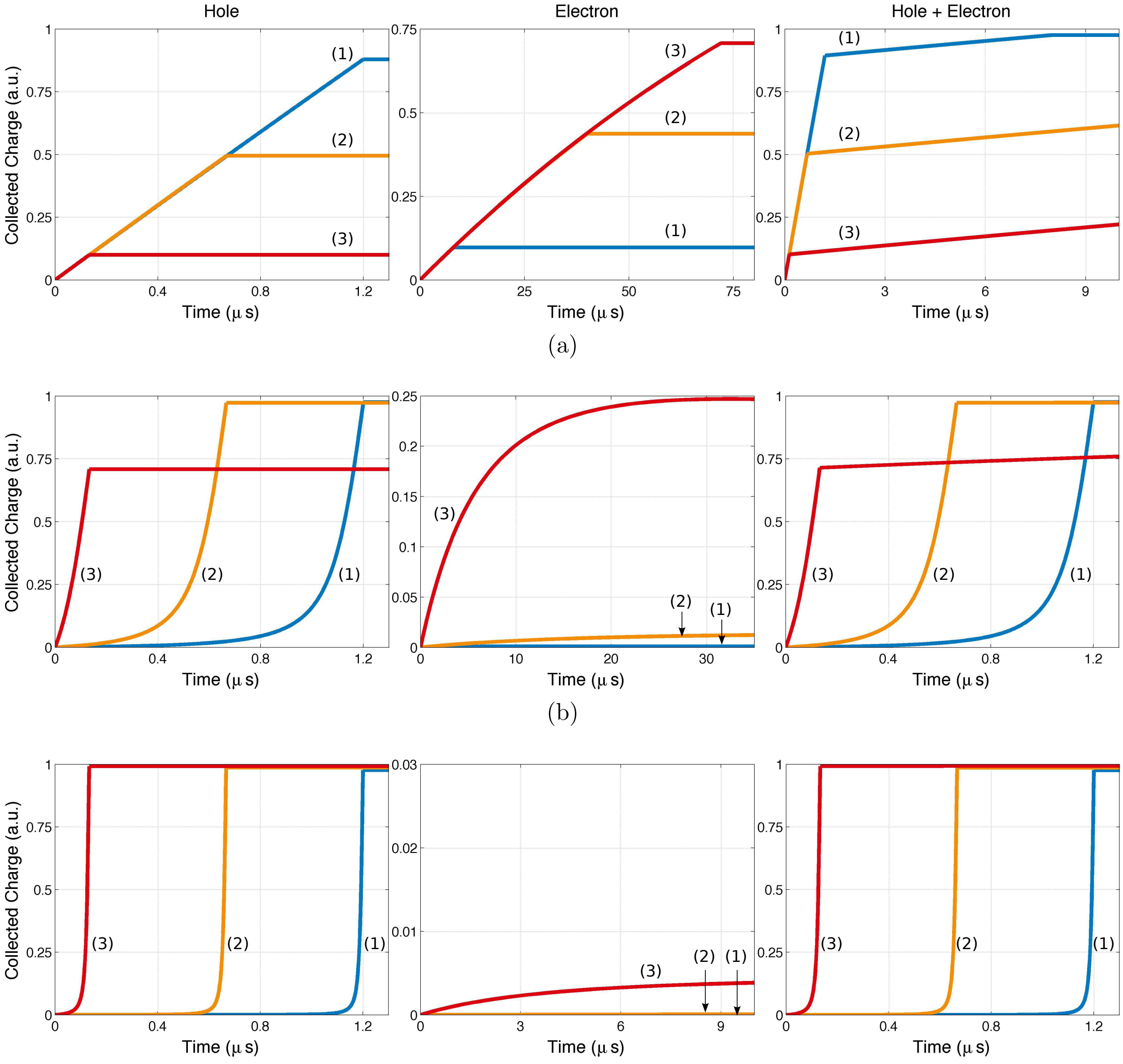

(a)

(b)

(c)

Figure 4.9: Normalized collected charge as a function of time for three interactions depths, Z_i = (1) $0.1L$, (2) $0.5L$, and (3) $0.9L$. Simulations are performed for (a) a conventional planar selenium detector without the grid (i.e., $Z_g = 0$), (b) a unipolar selenium detector with $Z_g = 0.8L$, and (c) a unipolar selenium detector with $Z_g = 0.98L$.

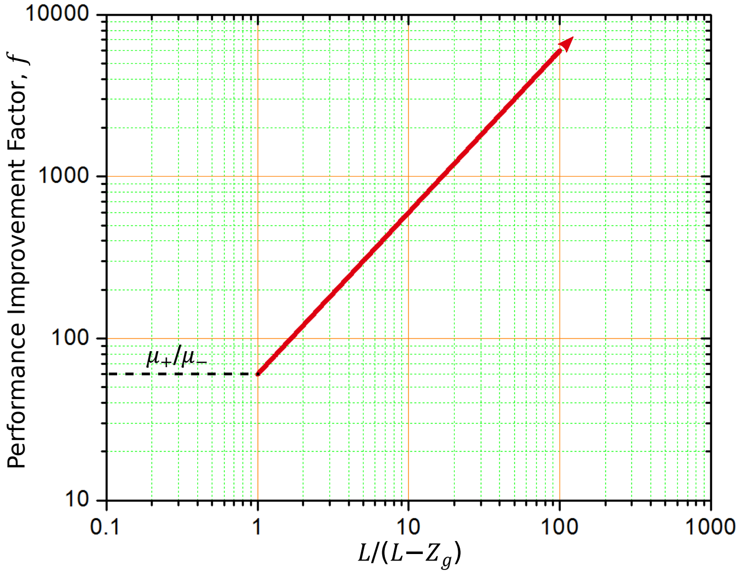

Figure 4.10: Performance improvement factor in orders of magnitude as an inverse function of the normalized grid distance from the collector.

4.3.4 Dispersion-limited photoresponse: reaching the intrinsic physical limit

In our time-of-flight (TOF) transient photoconductivity experiments[2] at room-temperature ($T = 295$ °K), we injected a sheet of carriers from the top surface into the photoconductor with a dye laser tuned to 337 nm wavelength and 5 ns pulse duration. The transient of the carriers was time-resolved and captured on a digital oscilloscope. The incident light intensity was kept relatively low for the *small-signal* case, not to appreciably distort the applied external field F [78].

Our study thus far has been based on the assumption of non-dispersive Markoffian transport in disordered solids. In such photoconductors, Scher-Montroll (SM) *universal-*

---

[2] See section 6.2 for details of the TOF experimental setup.

ity of the photocurrent is not applicable and the propagating carrier packet experiences broadening which is described by Gaussian statistics [44], where the position of the peak of carrier distribution coincides with its spatial mean, as illustrated in Fig. 4.11a. This broadening, which is observed as an extended exponential decay in the tail of our TOF experiments in Fig. 4.11b, is due to (1) diffusion, (2) fluctuations of the shallow-trap release time, and (3) mutual Coulombic repulsion [79], [80], [81]. However, in the small-signal case, we can neglect spreading due to mutual Coulomb repulsion of the free charge density. The Gaussian statistics for the dispersion σ_D and the mean carrier displacement ℓ obey time dependencies $\sigma_D \propto t^{1/2}$ and $\ell \propto t$, which yield the well-known relation $\sigma_D/\ell \propto t^{-1/2}$ [45].

Hole dispersion in a-Se was extrapolated from the exponential decay at the tails of the measured TOF photocurrent transients in Fig. 4.12 for various operating fields. The tail data, which theoretically represents a Gaussian integral, was processed using the following steps: (1) weighted-average smoothing, (2) sigmoidal fitting, (3) differentiating, and finally (4) Gaussian fitting.

Another reason for the spatial dispersion of the ionization charge is the Gaussian cloud which is formed around the primary interaction site of each absorbed photon, as depicted schematically in Fig. 4.13. This dispersion of the charge cloud, which depends on the range of the produced photoelectron in the material, obeys the relation $\sigma_C \propto E^2$, where E is the energy of the absorbed high-energy photon [82].

In summary, the spreading of the radiation induced carrier packet initially depends on the range of the produced photoelectron at the onset of ionization. Then, the Gaus-

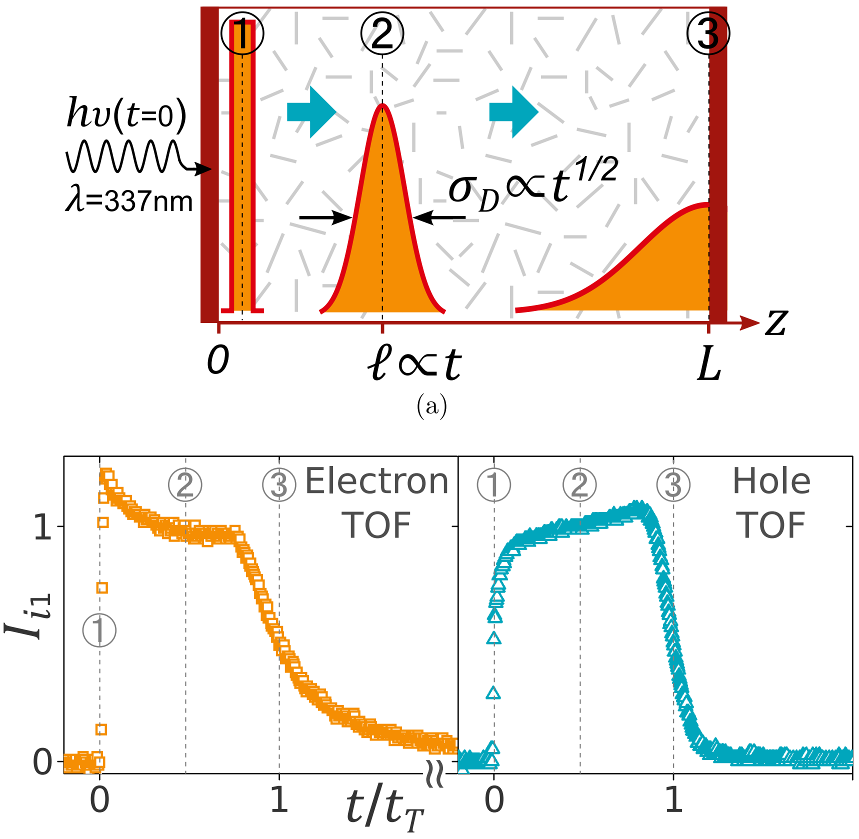

(a)

(b)

Figure 4.11: (a) Schematic representation of carrier packet transport in a non-dispersive solid. (b) Optical TOF transients for electrons and holes in a planar a-Se detector.

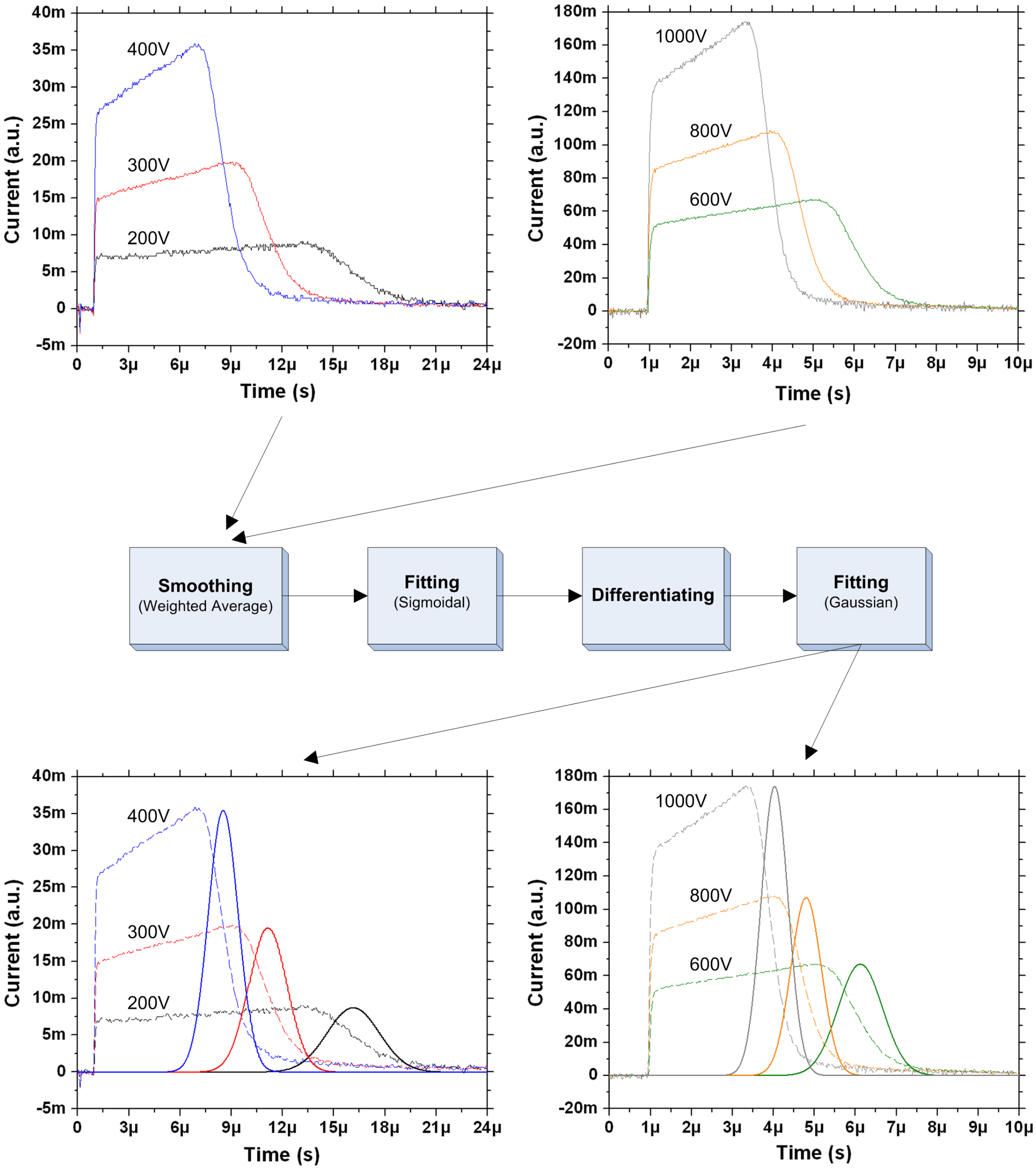

Figure 4.12: Extrapolated hole dispersion in a-Se TOFs, parametric in F.

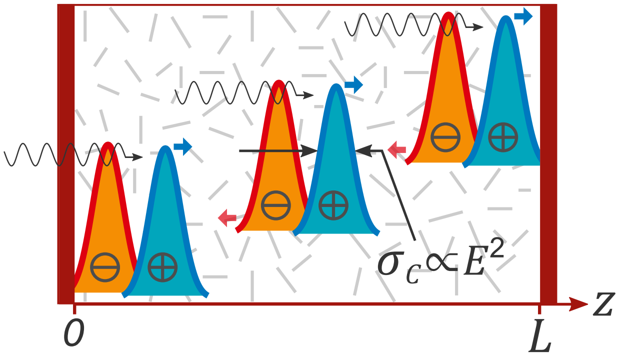

Figure 4.13: Schematic representation of Gaussian photoelectron clouds created at the onset of radiation ionization.

sian cloud drifts in the presence of an applied field towards the collector while experiencing further transit dispersion due to diffusion, multiple trapping, and mutual Coulombic repulsion. Using the joint spatial distribution function for the statistically independent carrier spreading variables, total spatial dispersion, which sets the intrinsic physical limit for the temporal resolution, is given as $\sigma = \sqrt{{\sigma_D}^2 + {\sigma_C}^2}$. Thus, the upper limit of Eq. 4.12 is determined by the width of the higher-mobility Gaussian cloud

$$f = \left(\frac{\mu_+}{\mu_-}\right)\left(\frac{L}{L - Z_g}\right) \leq \left(\frac{\mu_+}{\mu_-}\right)\left(\frac{L}{4\sigma}\right) \tag{4.13}$$

where 4σ accounts for 95% of the total charge in a Gaussian packet. Figure 4.14 shows the performance improvement factor saturating at the dispersion limit.

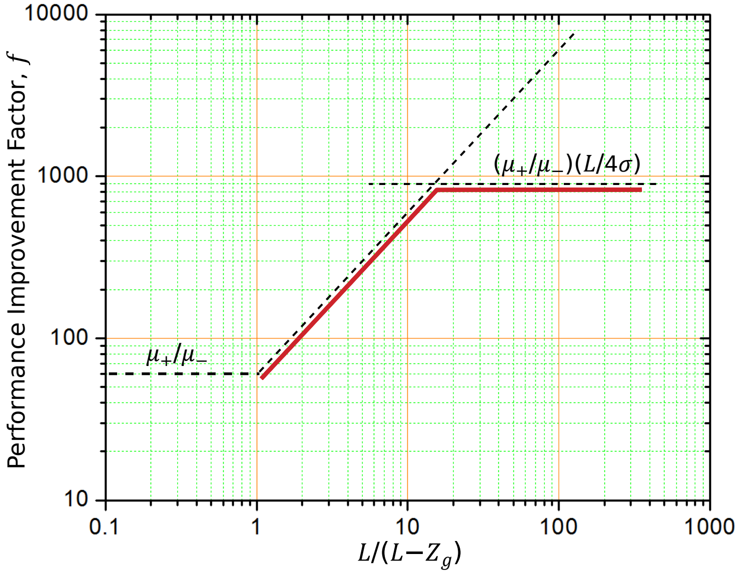

Figure 4.14: Performance improvement factor limited by charge cloud dispersion.

4.4 Conclusions

We investigated the deteriorating effect of poor carrier transport on the temporal resolution and the counting rate of an amorphous selenium (a-Se) spectrometer. To circumvent the problem of poor carrier transport, we proposed establishing a strong near field effect for unipolar charge sensing using an electrostatic shield within the detector structure. For the new device structure, we introduced the concept of time-differential photoresponse where the included current on the collector due to an impulse excitation is no longer transit-time limited and is proportional to the time-derivative of the photocurrent in a conventional planar device for the same excitation. Theoretical results showed that the temporal resolution (and consequently, the photon count-rate) can be improved substantially and one can reach the intrinsic physical limit, which is determined by the spatial dispersion of the photoinduced carrier packet.

Chapter 5

Unipolar Charge Sensing: Design and Implementation

5.1 Introduction

The proposed method for substantially mitigating the problem of poor carrier transport in disordered solids was to establish a strong near-field effect by modifying the two-terminal planar detector structure and including an electrostatic shield between the sandwich electrodes, a design that was first implemented by Frisch [67] in 1944 to solve the trapping effect of positive ions in conventional gas detectors.

In this chapter, we propose implementation techniques for establishing the electrostatic shield between the sandwich electrodes inside evaporated disordered solids. First we show the construction of a multiwire solid-state detector (MWSD) using an implementation technique similar to that of Charpak's multiwire proportional chamber [48]. This design was not operational due to permanent damage caused by *arcing* (or arc discharge) at the onset of applying the external filed. Second, we propose a microstrip solid-state detector (MSSD), which is inspired by Oed's microstrip gas chamber [52], using standard photolithography techniques. This design proved to be very successful in ensuring a stable unipolar operation.

5.2 Multiwire Solid-State Detector

The very first unipolar solid-state device we built, with its cross-section depicted in Fig. 5.1a, was based on Charpak's multiwire proportional chamber [48]. The difference in our design is that we use the intermediate multiwire electrode not for collecting but for electrostatic shielding. To establish the multiwire electrode, our design is shown in Fig. 5.1b. Wires are threaded from one hole on one side of the hollow frame to the opposite hole on the other side while residing inside V-grooves. For the wire to lay flat on the frame after its threaded, the frame must have an outside radius close to the holes. Also, V-grooves are used to guide the threaded wire along a straight path. Note that holes and grooves are drilled using laser micro-machining and the outside radius is machined with a form tool. After the wires are threaded through all the holes, a guitar-shaped frame is created which is placed over a substrate with patterned collecting pixel electrodes.

After the threaded frame is paired with a pixellated substrate, they are placed inside the deposition chamber and a photoconductive material is evaporated through the wires on the pixel electrodes. When the deposition process is complete, the pixel electrodes and the wires are entirely covered with the deposited film and the electrostatic shield is formed within the detector volume. Note that detector deposition is uninterrupted and is carried in a single-step. Finally, the common drift electrode is deposited on top to form the sandwich cell and for applying the external field. The implemented device is shown in Fig. 5.2.

Figure 5.2a shows the stainless steel frame, the threaded stainless steel wires that form the multiwire electrostatic shield, and the laser-etched V-grooves. The wires are 25 μm in diameter and have a pitch of 100 μm. Figure 5.2b shows the multiwires placed directly over a 1mm^2 pixel with 11 wires covering the entire pixel area. Once the multiwires were aligned over the pixel, they were glued to the substrate along both sides and the frame was disassembled after. Finally, Fig. 5.2c shows the fabricated MWSD with amorphous selenium (a-Se) as the photoconductive film. Although some planarization techniques were utilized during film deposition, the step coverage achieved was not sufficient and the device was permanently damaged after the application of the external field due to arc discharge.

5.3 Microstrip Solid-State Detector

Inspired by another variant of the multiwire proportional chamber, called the microstrip gas chamber [52], and for the first time, we have fabricated a solid-state detector with an internal electrostatic shield using standard photolithography techniques [83]. The proposed device is called the microstrip solid-state detector (MSSD) and as shown schematically in Fig. 5.3, it consists of an evenly spaced insulating pillars over the collector (or the pixel) with pillars' top side coated with a conductive layer to form the shielding microstrips. To

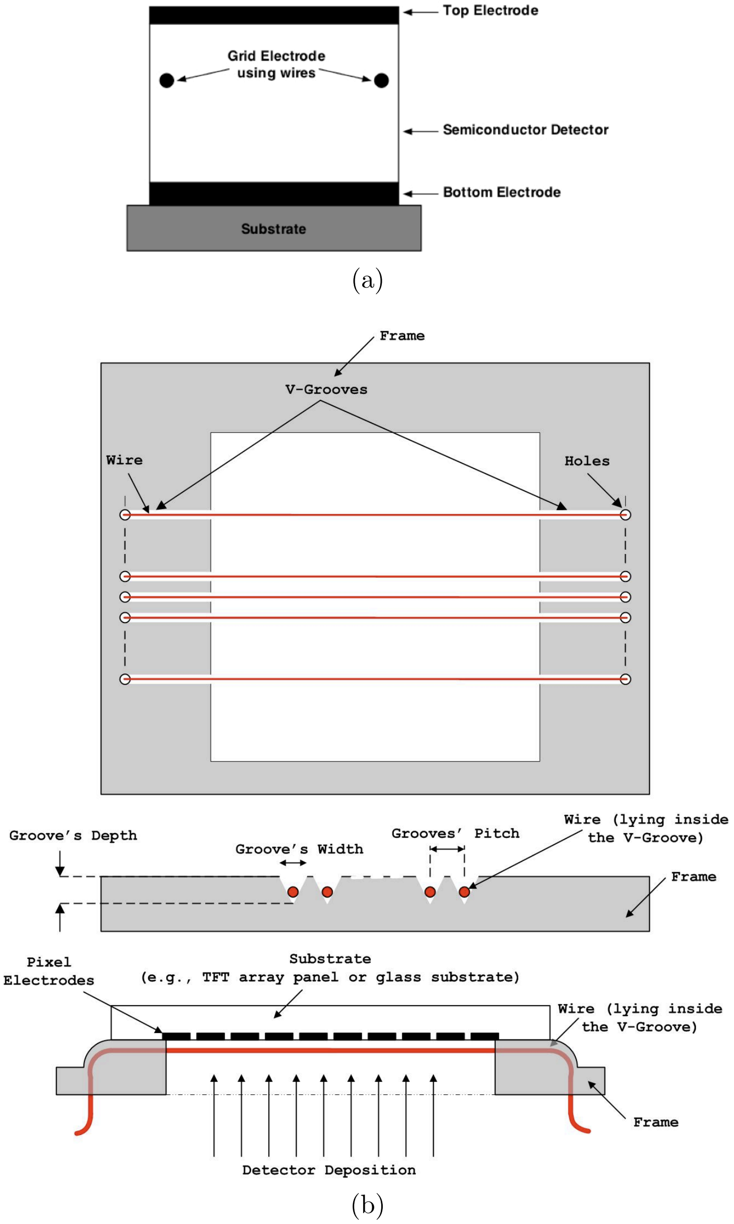

Figure 5.1: (a) Schematic representation of the multiwire solid-state detector. (b) Proposed method of establishing the multiwire electrostatic shield using wire-threading through opposite holes across a hollow frame. The threaded frame is positioned over a pixellated substrate and a photoconductive material is evaporated through the frame onto the substrate.

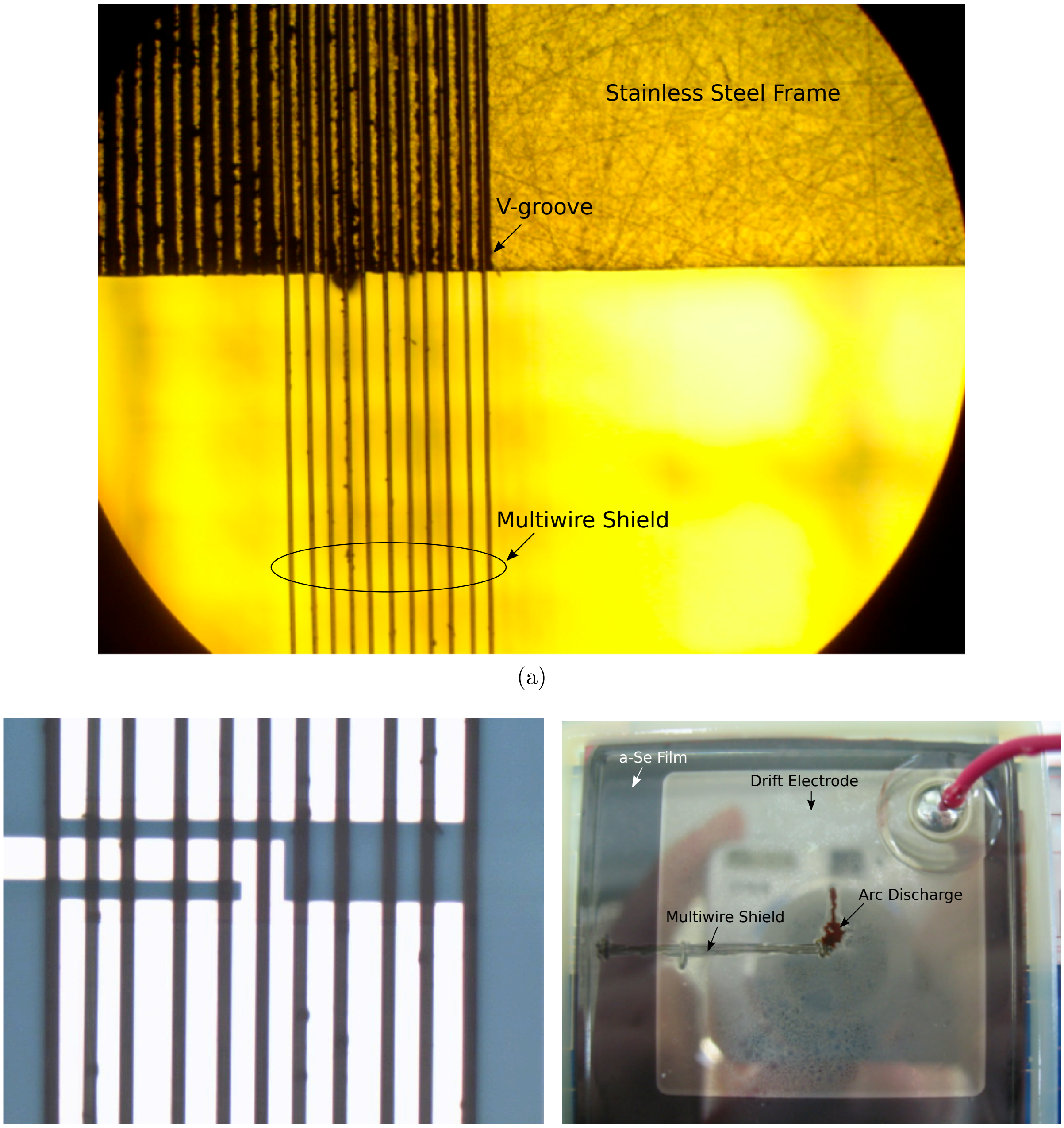

(a)

(b)

(c)

Figure 5.2: (a) Frame holder with threaded stainless steel wires sitting in laser-etched V-grooves. The diameter of the wires is 25 μm diameter with a pitch of 100 μm. (b) The multiwire shield is placed over a 1mm^2 pixel electrode. (c) Fabricated MWSD with a-Se as the photoconductive film.

ensure blocking contacts for limiting the excess charge injection, the microstrips can be surrounded by another insulating/blocking layer.

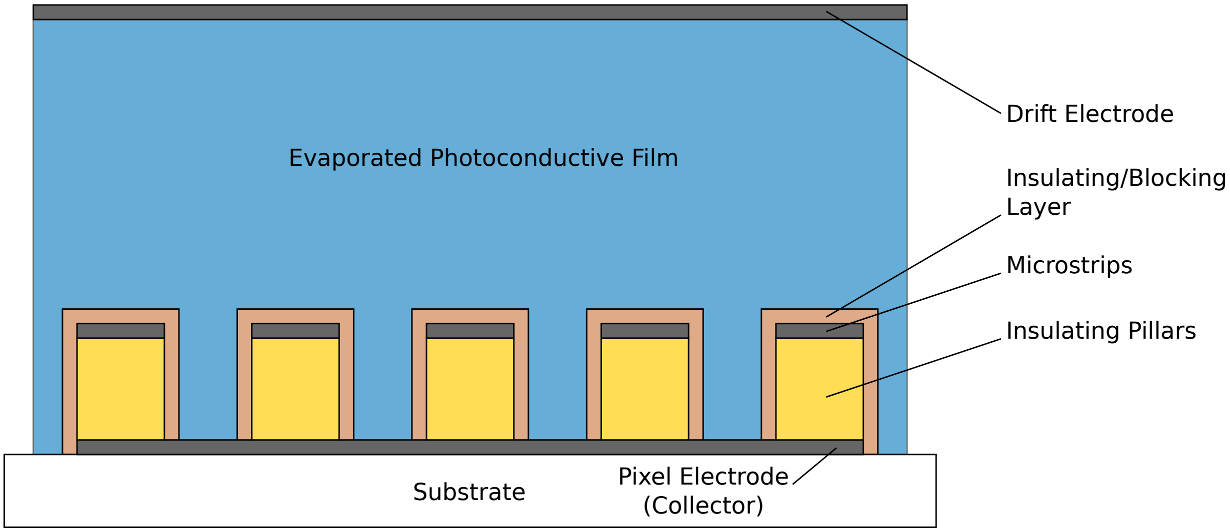

Figure 5.3: Schematic representation of the microstrip solid-state detector (MSSD).

5.3.1 Photolithography process

General lithography process steps (which are emulated with Sentaurus structure editor in Fig. 5.4) and fabrication details of the MSSD device shown in Fig. 5.6 are provided in Table 5.1. The fabricated device consists of Chromium (Cr) pixels, polyimide (PI) insulating pillars, Cr microstrips, and PI blocking layers. Amorphous selenium (a-Se) is evaporated over the structure as the photoconductive material, and finally, a semi-transparent gold (Au) layer is sputtered on top to provide the drift electrode while enabling optical excitation measurements.

Table 5.1: Explanation of the process steps shown in Fig. 5.4.

#	General process as emulated in Fig. 5.4	Fabricated device of Fig. 5.6
1)	Prepare substrate	3.3″×3.3″ Corning glass
2)	Deposit conductor to form the bottom electrode	Sputtered 70 nm Cr
3)	Pattern the bottom electrode to form the pixellated collectors	Patterned[†] with mask 1 of Fig. 5.5
4)	Deposit insulator (via plasma-enhanced chemical vapour deposition or spin casting)	Spin-cast PI[††] and cured to form a thick layer
5)	Deposit conductor to form the internal electrode	Sputtered 150 nm Cr through shadow mask of Fig. 5.5
6)	Pattern the internal electrode to form the shielding microstrip grid	Patterned with mask 2[†††] of Fig. 5.5
7)	Etch insulator to form the microstrip pillars and to expose the collectors	Reactive ion etching (RIE) with O_2 plasma
8)	Deposit insulator to form the blocking layer	Spin-cast PI and cured to form ∼1 μm-thik layer
9)	Pattern blocking layer to extend slightly beyond microstrips' edges	Patterned with mask 3 of Fig. 5.5
10)	Deposit the photoconductive film	Evaporated 200 μm a-Se
11)	Deposit the drift electrode	Sputtered 10 nm Au

[†] For *patterning*, we first spun AZ3312 photoresist over the substrate followed by a soft bake. Second, we aligned the corresponding chromium mask (shown in Fig. 5.5) to the alignment marks on the substrate and exposed the structure to ultraviolet (UV) light. Third, we developed the resist with AZ300-MIF developer followed by a hard bake. The regions of the resist that were exposed to UV were removed and the desired pattern appeared. Finally, we etched the developed pattern on the sputtered metal using the liquid etchant prepared.

[††] Thickness of the PI layer depends on the material (i.e., polyimide precursor and solvent), spin speed, curing temperature, and finally, curing time. We used polyimide PI-2600 series from HD Microsystems [84] and achieved layer thicknesses ranging from 1 to 50 μm. Thicknesses exceeding 10 μm were obtained by multiple spin-casting and curing.

[†††] Microstrips' spacing is equal to strip's width and ranges from 5 to 20 μm for the fabricated device.

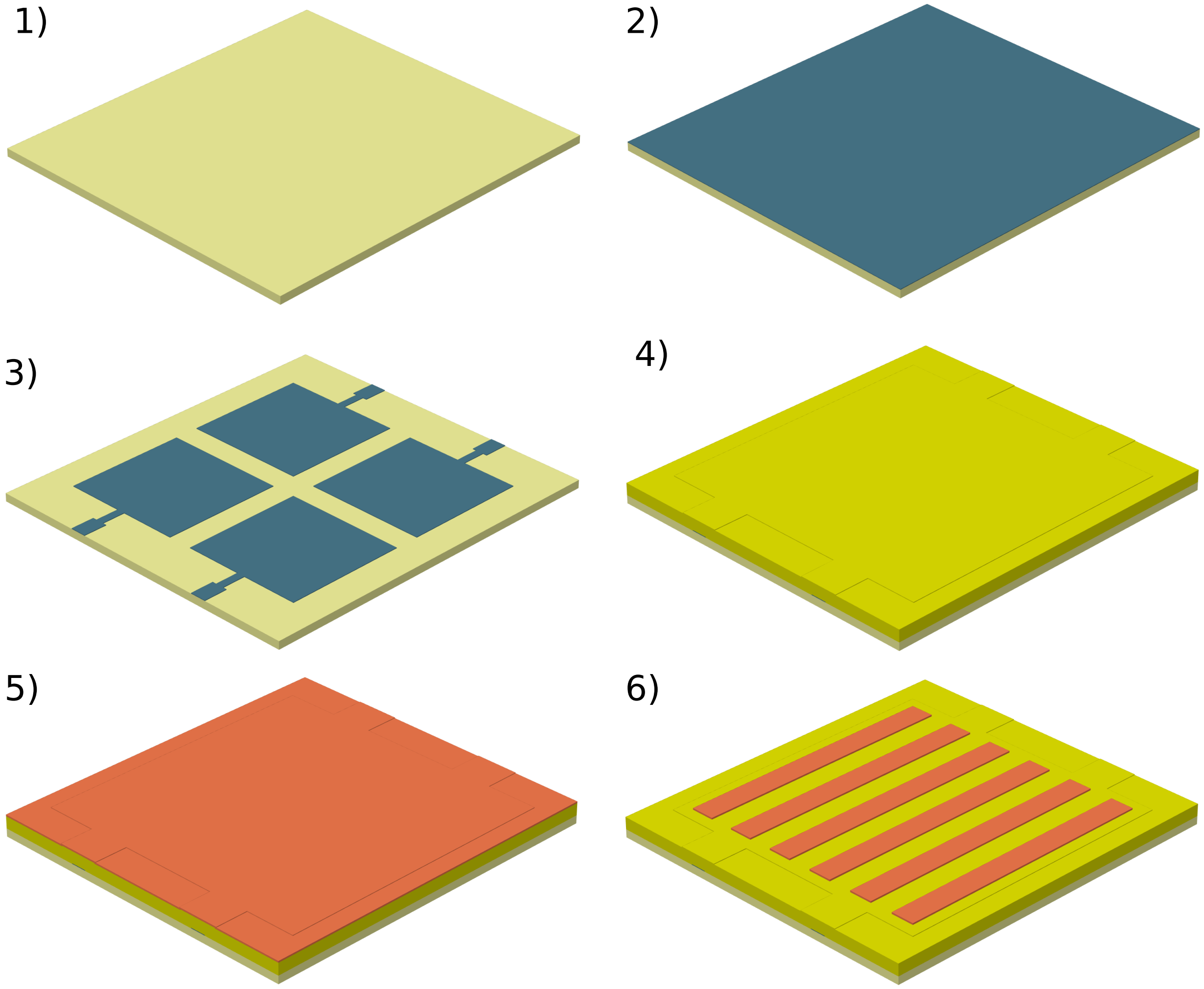

(a)

Figure 5.4: (a) Emulated lithography process steps for fabrication of the MSSD using Sentaurus Structure Editor. Steps 1 to 6 of Table 5.1.

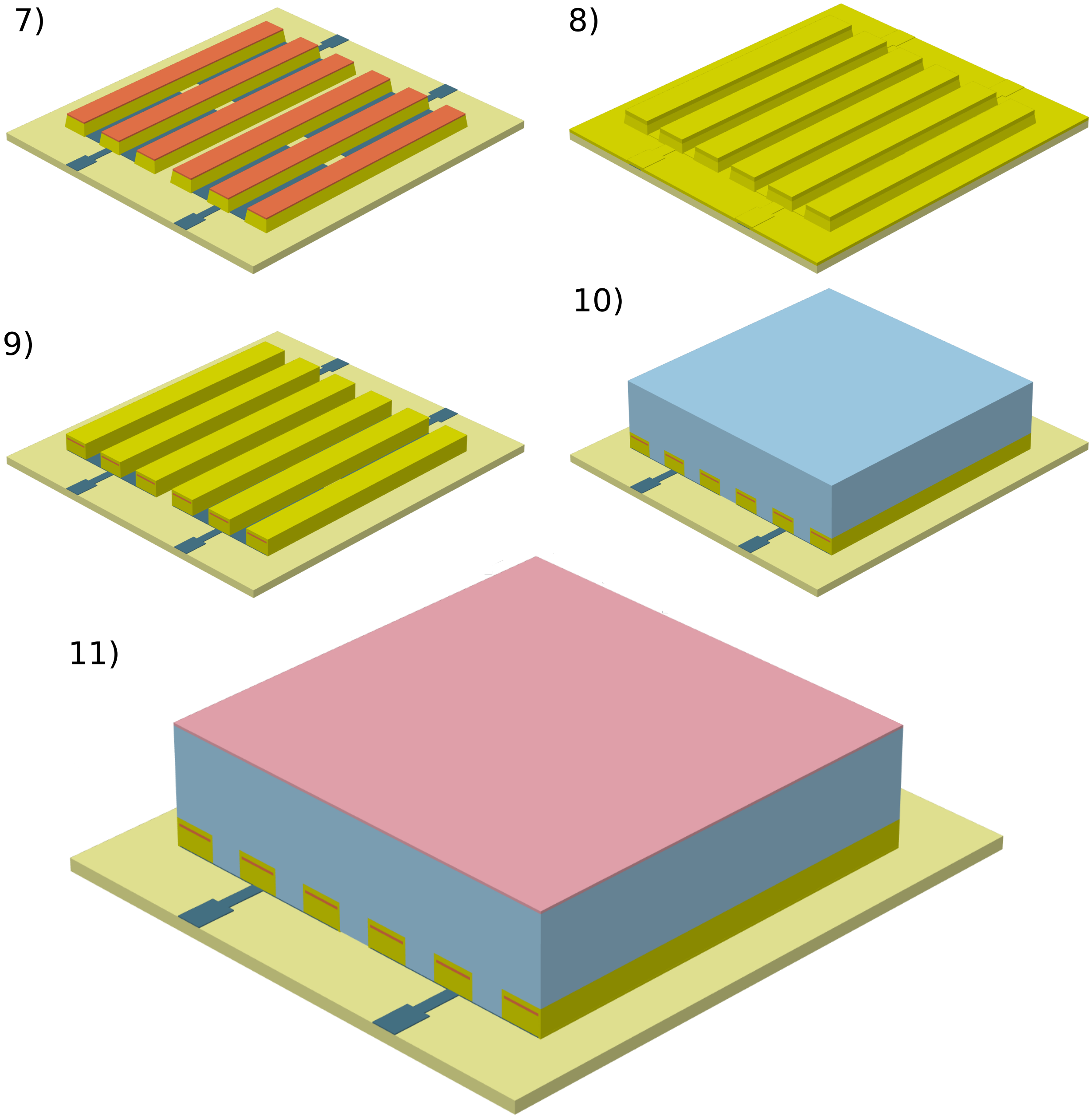

(b)

Figure 5.4: (b) Emulated lithography process steps for fabrication of the MSSD using Sentaurus Structure Editor. Steps 7 to 11 of Table 5.1.

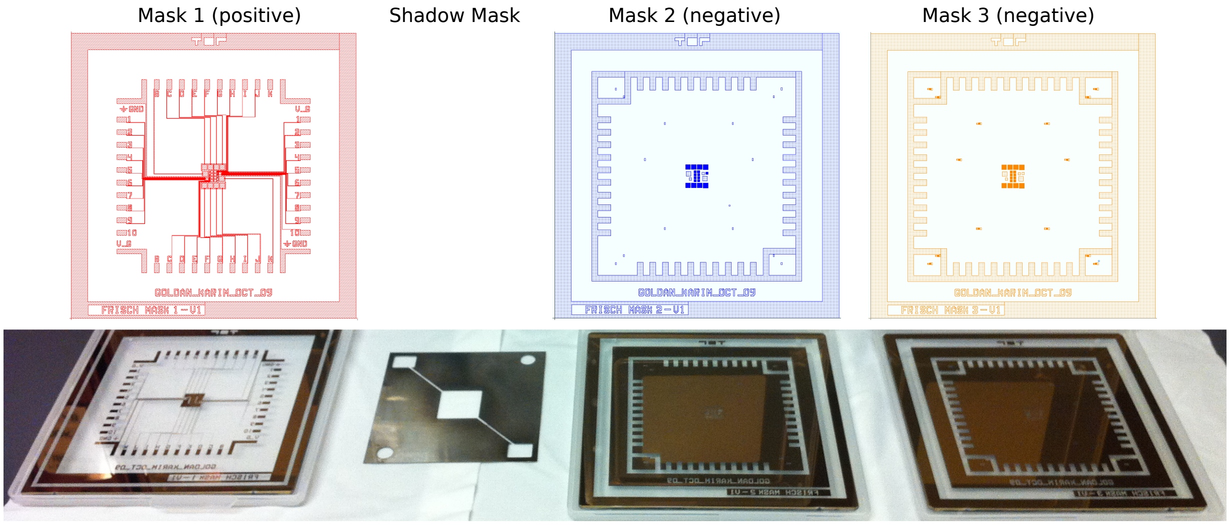

Figure 5.5: Photolithography chromium masks used for the fabrication of the MSSD.

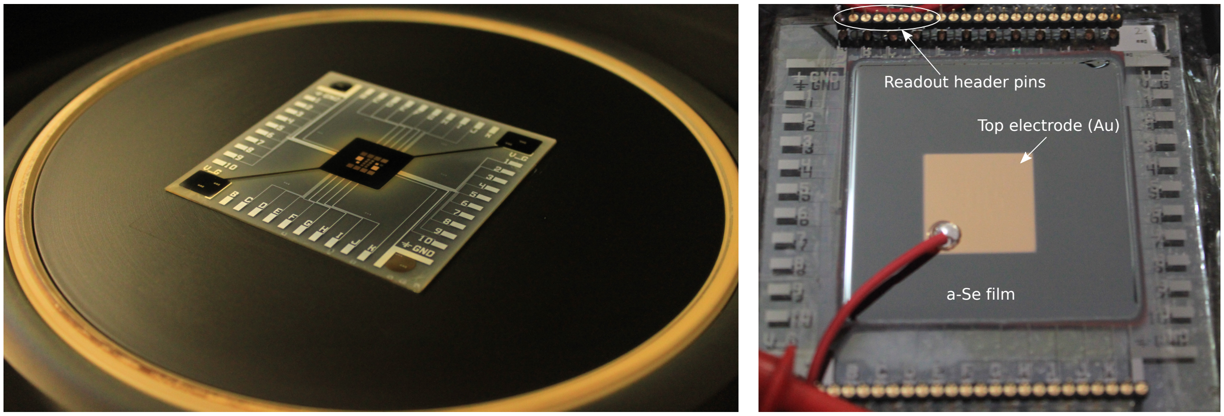

(a)

(b)

Figure 5.6: Fabricated MSSD on a $3.3'' \times 3.3''$ corning glass substrate (a) without and (b) with evaporated selenium film.

5.3.2 Polyimide residue

For anisotropic etching of the polyimide (PI) layer, one must use pure oxygen (O_2) plasma during reactive ion etching (RIE). However, after etching residues are left behind on the surface in the form of speckles, and the thicker the thickness of the etched PI layer, the bigger the speckle residues formed (see Fig. 5.7a). The roughness of the residues was measured with atomic force microscopy (AFM) and results are shown in Fig. 5.7b for three PI thicknesses. As an example, after we etched 5.2 μm of PI film, the surface roughness peaked to about 4 μm. The AFM technique also serves as a good measure of the speckle grain size.

One method to remove the residues is to use a gas mixture containing O_2 and carbon tetraflouride (CF_4). The problem with introducing CF_4 in the RIE chamber is that it reduces selectivity due to damaging ion bombardment of the chromium microstrips (which are used as masks for etching PI) and increases isotropy of the etching process. The less anisotropic the etching process, the more undercut pillars will experience and for small microstrip widths, the pillar structure can collapse altogether.

Because we must maintain maximum anisotropy for prolonged RIE etching of thick PI layers, we used O_2 as the only plasma etchant. However, to remove PI residues, we added a *lift-off* process (described in Table 5.2) to our lithography steps and coated the pixel electrode (where PI residues reside) with a thin Aluminum (Al) layer as the sacrificial layer. Note from Fig. 5.8 that when the sacrificial layer was etched, the speckle residues were also washed away from the surface.

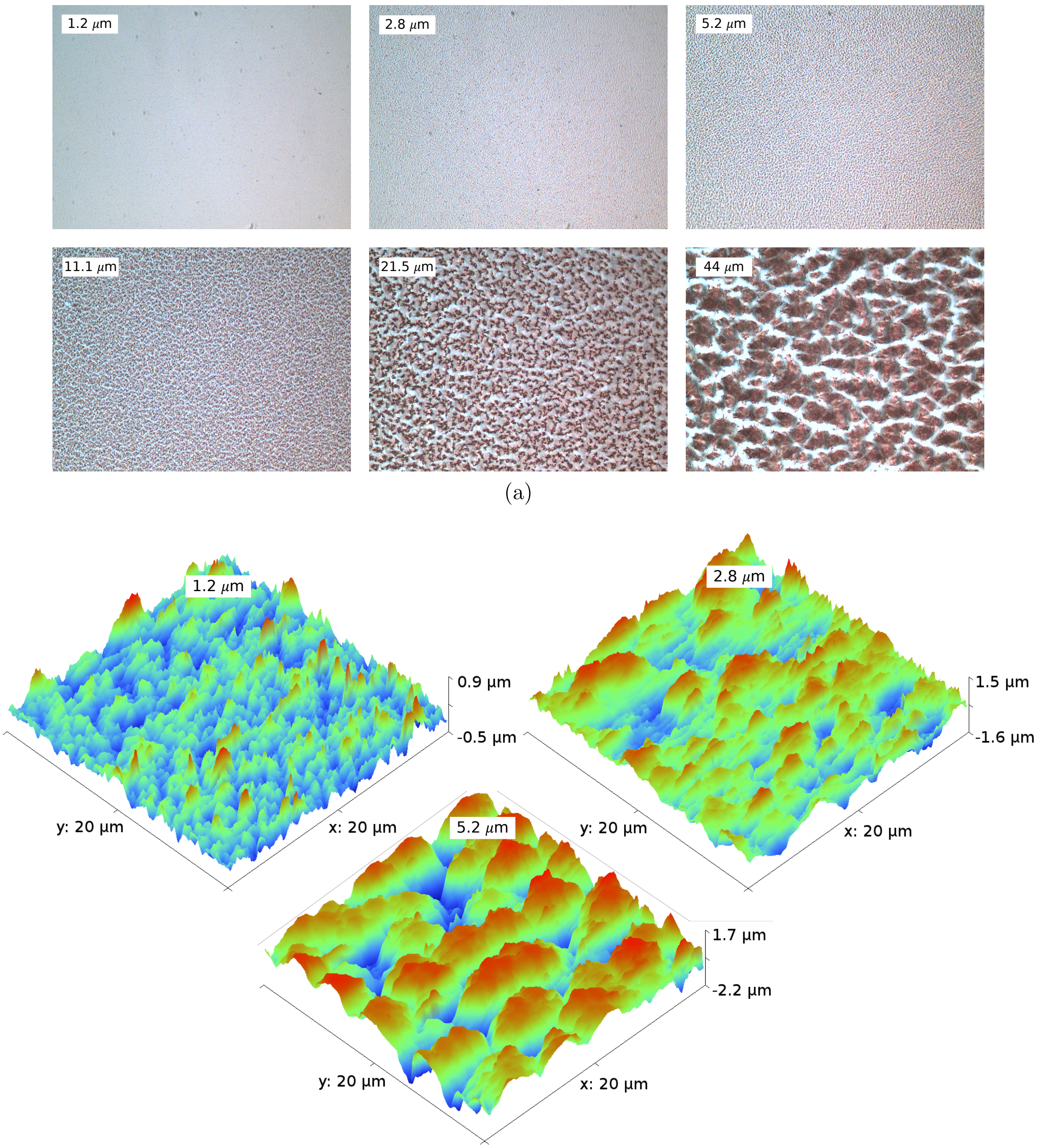

(a)

(b)

Figure 5.7: (a) Speckle residues formed on the surface after etching varying thickness of the PI layer (i.e., from 1.2−44 μm). (b) AFM of the speckle roughness for 3 PI thicknesses.

Table 5.2: Lift-off process steps.

Steps	General process	Fabricated device of Fig. 5.6
2.1)	Deposit conductor to form the sacrificial layer	Sputtered 50 nm Al
7.1)	Etch the sacrificial layer	Etched Al with PAN etchant

* Note that steps are numbered according to the lithography process steps in Table 5.1.

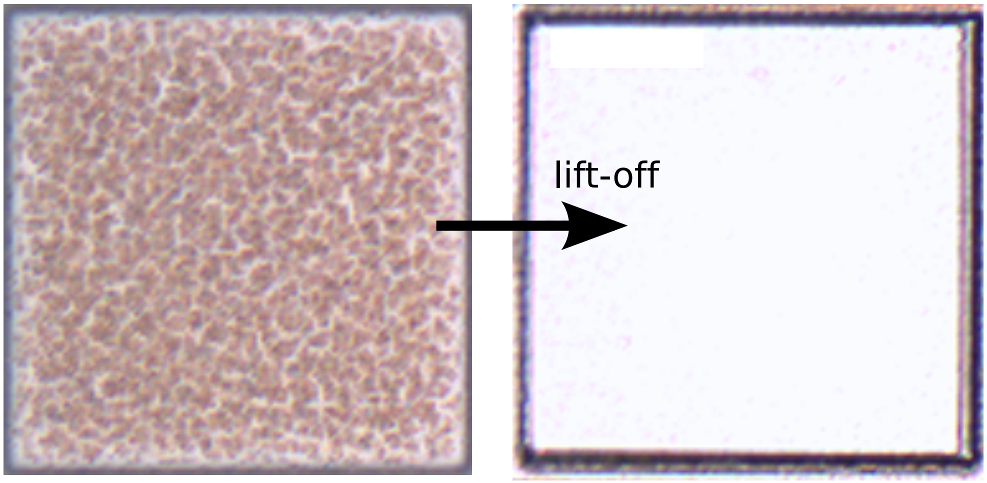

Figure 5.8: Speckle residues were washed away with the lift-off process.

5.3.3 Structural and functional analysis of the optimal device

To study the structure of the fabricated microstrip solid-state detectors, we used scanning electron microscopy (SEM). Because the substrate for our device is corning glass and the deposited films are non-crystalline, the substrate cannot be cleaved to obtain a sharp cross-section (or edge) suitable for SEM. Instead, we diced the substrate in a direction orthogonal to that of the microstrips and polished the diced edges using the process explained in Appendix A. The difference in quality of the SEM images before and after polishing can be seen from Fig. A.1 and Fig. A.3, respectively.

While initial insights were obtained from simulation results, varying pillar heights and spacings were fabricated to determine empirically optimal values. Given practical limitations, such as (1) imperfections of our in-house photolithography (2) and the ability of our selenium evaporator to cover surface topology with the utilization of some planarization techniques, our empirical data suggested optimal strip pitch of ~ 30 μm and pillar height of ~ 7.5 μm for the fabricated device, as shown in Fig. 5.9a. Larger pitch reduced the effectiveness of the shield and for smaller pitch shown in Fig. 5.9b, the operation was limited to low fields due to discharges and breakdown of the very thin insulator (~ 50 nm) at the strip edges which resulted in enormous charge injection from the microstrip electrode. Because of the large ($> 1\mu$m) pillar height, and for simplicity of fabrication, the insulator over the collector was not etched.

The weighting potential contour of the optimal device is simulated in Fig. 5.10a which shows a very small change in V_W in the region between the drift electrode at $z = 200$ μm and the microstrips at $z = 7.5$ μm, also called the interaction region. However, V_W changes substantially in the region between the microstrips and the collector at $z = 0$ μm, also called the detection region. Figure 5.10b further illustrates the weighting potential distribution for carrier drifts terminating on the collector along $x = 22.5$ μm and on the microstrip along $x = 7.5$ μm. For comparison purposes, a conventional planar device without the shielding microstrips was also fabricated on the same substrate and Fig. 5.10 shows its constant-slope V_W distribution.

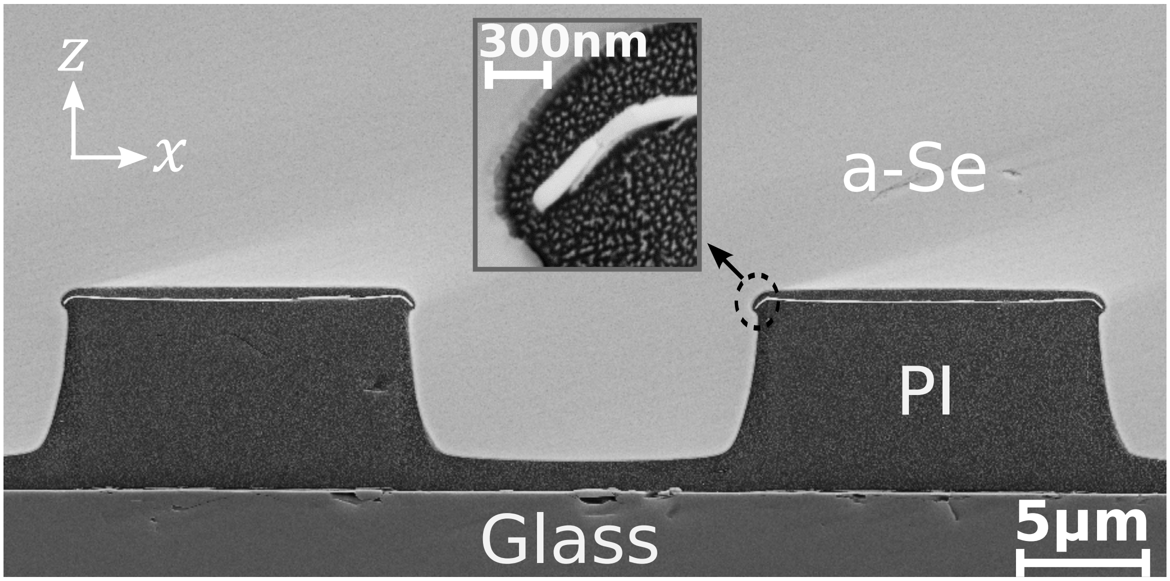

(a)

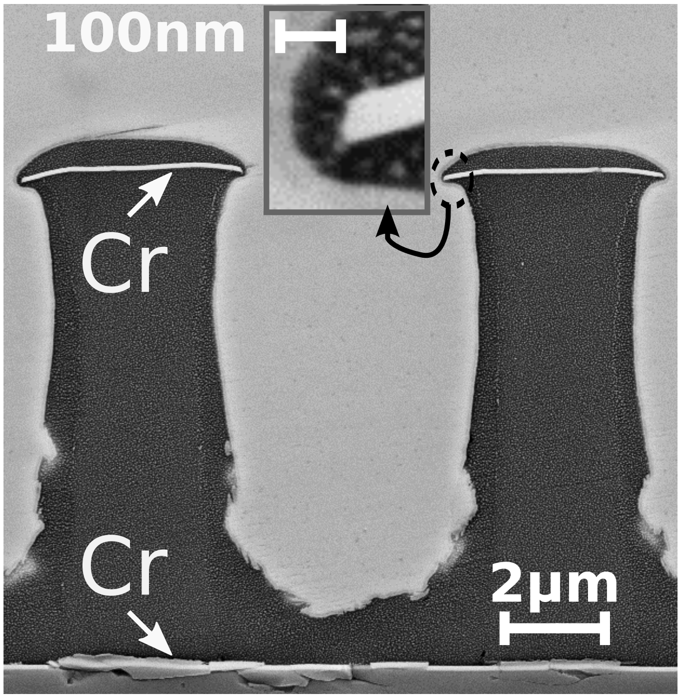

(b)

Figure 5.9: SEM of representative devices with the pillar height of 7.5 μm and the strip pitch of (a) 30 μm and (b) 10 μm.

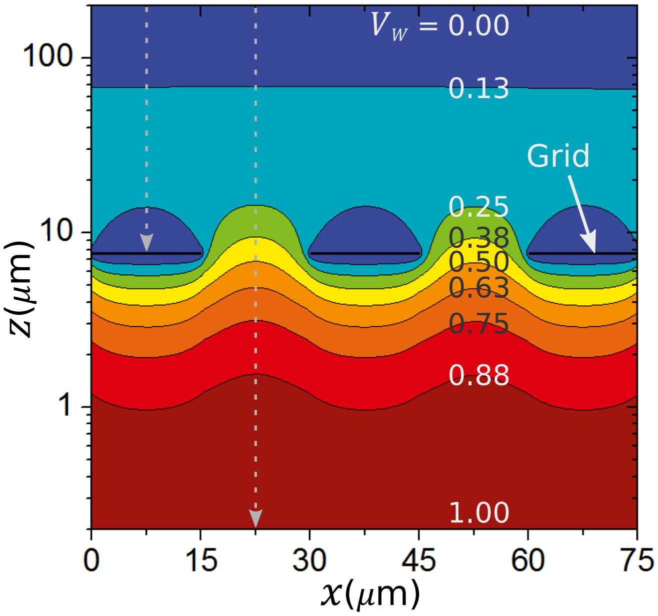

(a)

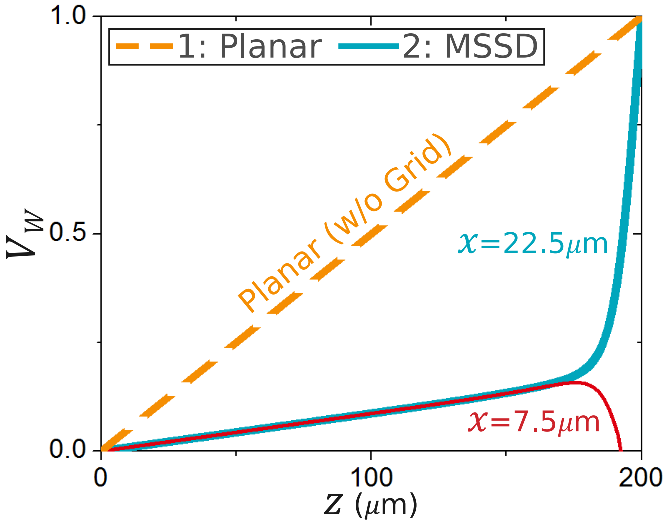

(b)

Figure 5.10: (a) Weighting potential contour of the fabricated optimal device with the strip pitch of 15 μm. (b) Weighting potential distributions along $x = 7.5$ μm and $x = 22.5$ μm for carriers terminating on the microstrip and the collector, respectively.

5.4 Conclusions

For the first time, we implemented an electrostatic shield inside a solid material using the proposed lithography-based microstrip solid state detector (MSSD). The device consisted of an evenly spaced insulating pillars over the collector where their top side was coated with a conductor to form the electrostatically shielding microstrips. To ensure blocking contacts for limiting the excess charge injection, the microstrips were surrounded by another thin insulating layer. After the fabrication of the blocking microstrips on the collector, a-Se film was evaporated over the structure as the photoconductive material, and finally, a semi-transparent layer was sputtered on top to provide the drift electrode. We also determined empirically optimal pillar height and pitch to be ~ 7.5 μm and ~ 30 μm, respectively.

Chapter 6

Unipolar Charge Sensing: Characterization and Performance

6.1 Introduction

The invention of the gas-filled multiwire proportional chamber (MWPC) by Charpak revolutionized the field of radiation detection and instrumentation [48], [49]. The work was evolved with the introduction of microstrip gas chambers (MSGC) [52], microgap gas chambers (MGC) [53], micromesh gas chambers (MICROMEGAS) [54], and gas electron multipliers (GEM) [55]. However, in most applications, the use of a solid detection medium is preferable because solid densities are about three orders-of-magnitude greater than gas, and thus, they yield much smaller detector dimensions that are ideal for high spatial and temporal resolution. The problem is that disordered solids, which are easier and less expensive to develop than single crystalline solids, have been ruled out as a viable radiation detection medium because of low carrier mobilities and transit-time-limited photoresponse. Inspired by Charpak's MWPC and its variants, we proposed for the first time a microstrip solid-state detector (MSSD) and theoretically showed another distinct property of the microstrip array, which is the *time-differential electrostatic shielding* for ultra-fast response. For the case of a single carrier drifting in any medium, this property results in an impulse photoresponse at the onset of carrier neutralization at the collector.

We use the proposed novel device in section 5.3 to experimentally verify our theoretical predictions which were the time-differential property of the electrostatic shield (see section 4.3.2), orders of magnitude performance improvement (see section 4.3.3), and the dispersion-limited photoresponse (see section 4.3.4). We consider more realistic experimental cases, as opposed to a single drifting excess carrier, where (1) a sheet of excess carriers is photoinduced close to the drift electrode with an optical laser excitation and (2) Gaussian carrier clouds are generated uniformly across the bulk with a high energy x-ray beam. Emphasis is on measured results obtained from chalcogenide glass amorphous selenium (a-Se) but conclusions drawn can be extended to other inorganic and organic photoconductive materials because of the universal feature of disordered solids, characterized by a broad distribution of individual event times, that is independent of their atomic or molecular structure [45]. This feature leads to Arrhenius-type temperature-dependent mobility, Poole-Frenkel-type field-dependent mobility, and transition from non-dispersive to anomalous dispersive transport at relatively lower temperatures [85], [86], [87] [88], [89]. Amorphous selenium (with a relative permittivity, ϵ_{Se}, of 6.3), which was perviously developed for photocopying machines, has been commercially revived as a direct x-ray photoconductor for digital imaging because it has high x-ray sensitivity and can be uniformly evaporated over large area as a thick film [90]. In addition, a-Se has shown to produce continuous and stable avalanche due to non-activated hot holes at fields exceeding 70 V/μm [91], [92], [93].

6.2 Comments on the Optimal Device

The structure of the optimal device is shown in Fig. 6.1 with strip pitch of 30 μm and pillar height of 7.5 μm. To ensure blocking contacts for limiting the excess charge injection, the microstrips were coated with another thin PI layer. A 200 μm-thick a-Se film was evaporated over the structure as the photoconductive material, and finally, a semi-transparent gold (Au) layer was sputtered on top to provide the drift electrode while enabling optical excitation measurements. The top contact is non-blocking not to impede the extraction of optically induced carriers. Also, for simplicity of fabrication, the insulator over the collector was not etched and this inhibits neutralization of the drifting charge by the collector. However, we have limited the build-up of this surface space charge using low-level excitation for a rested specimen, and thus, space charge perturbation is minimized. Note that the collector area, A, is 4 mm^2 with $\sim$130 interconnected microstrips. The reason for this pixel size is to achieve a good compromise between small detector capacitance and detectable signal at low-level excitation at low fields.

Also, recall the weighing potential distribution of the optimal device in Fig. 5.10 in section 5.3.3. According to Eq. 4.6, no net charge is induced on the collector due to the drift of those primary carriers that terminate on the microstrips because the change

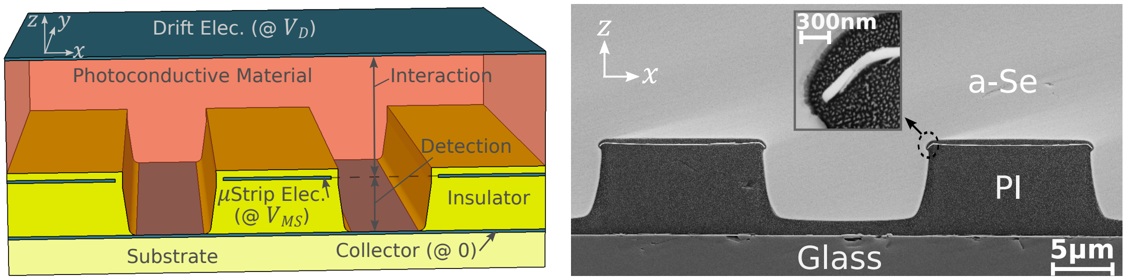

(a) (b)

Figure 6.1: (a) Schematic of the fabricated device as explained in section 5.3. (b) SEM of the optimal device with strip pitch of ~ 30 μm and pillar height of ~ 7.5 μm.

in the weighting potential (ΔV_W) is zero. To avoid this problem, one must bend the electric field lines in the drift volume so that all primary carriers are steered away from the microstrips and channeled towards the collector. For our devices, where the pillar height is much smaller than the photoconductor thickness, we found that the ratio, r, of the microstrip bias V_{MS} to the drift electrode voltage V_D for 100% charge collection efficiency is approximately one-fifth ($r = V_{MS}/V_D \approx +0.2$).

6.3 Experimental Setup for Transient Photoconductivity Measurements

Figure 6.2a schematically represents the setup for our photoconductivity experiments with impulse-like optical laser and x-ray excitations. The selenium ionization chamber, with its photograph shown in Fig. 6.2b, has three connectors: (1) the high voltage (HV) which provides the external field to a-Se and is the same as the drift voltage, (2) the grid voltage which provides bias to the shielding microstrips, and (3) the signal output (SIG) which connects to a current amplifier. The current amplifier is made with an RC circuit at the feedback of the OPA655/BB operational amplifier. Also note that the high voltage, supplied from an ORTEC556 HV power supply (HVPS), is applied to the photoconductor only a few milliseconds before the impulse-like excitation through a HV relay. In our optical laser TOF experiments at room-temperature ($T = 295$ °K), as shown in Fig. 6.2c, we injected a sheet of carriers from the top surface into the photoconductor with a VSL337 dye laser. Finally, in our x-ray TOF experiments, the impulse-like excitation was generated with a XR200 pulsed x-ray source. Figure 6.2d shows the photograph of this experimental setup. The transient of carriers after amplification was time-resolved and captured on a Tektronix TDS360 digital oscilloscope.

To characterize detector risetime in pulse mode, we used single photon counting experiments. The experimental setup is identical to that of Fig. **??** with the exception that the energy source was replaced with a ^{22}Na radioactive source, which annihilates to produce 511 keV gamma rays, and the output signal was taken from the AMPTEK-A250CF preamplifier to measure signal risetime.

6.4 Optical Time-of-Flight

The canonical method for transport studies of highly resistive, low mobility solids such as a-Se is the time-of-flight (TOF) transient photoconductivity experiment [56]. In addition, one can use this technique to deduce the spatial distribution of the weighting potential in the bulk. In our TOF experiments at room-temperature ($T = 295$ °K), we injected a sheet

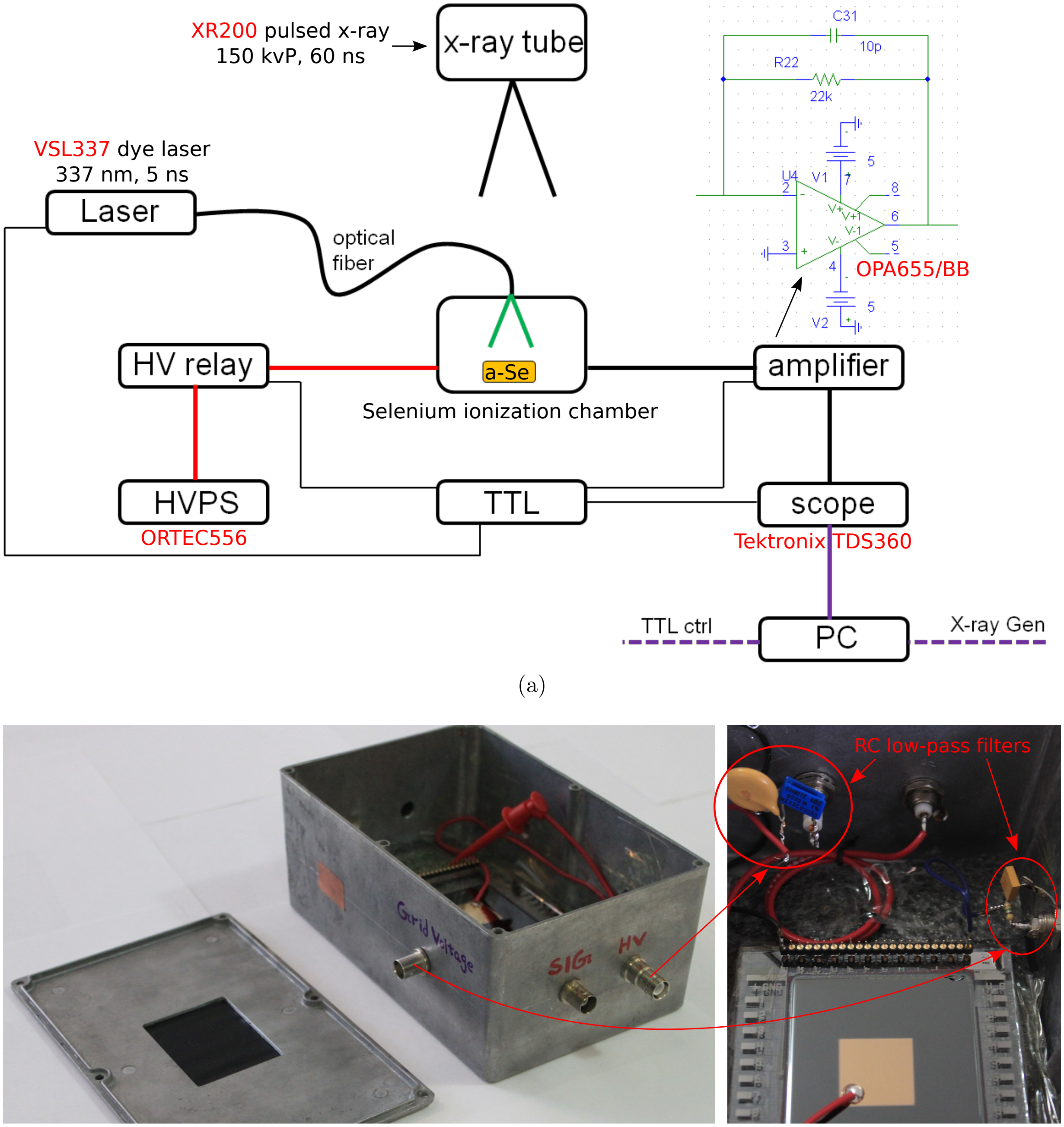

(a)

(b)

Figure 6.2: (a) Schematic of photoconductivity experiments with impulse-like optical laser and x-ray excitations (courtesy of ANRAD Corporation). (b) Photograph of the selenium ionization chamber.

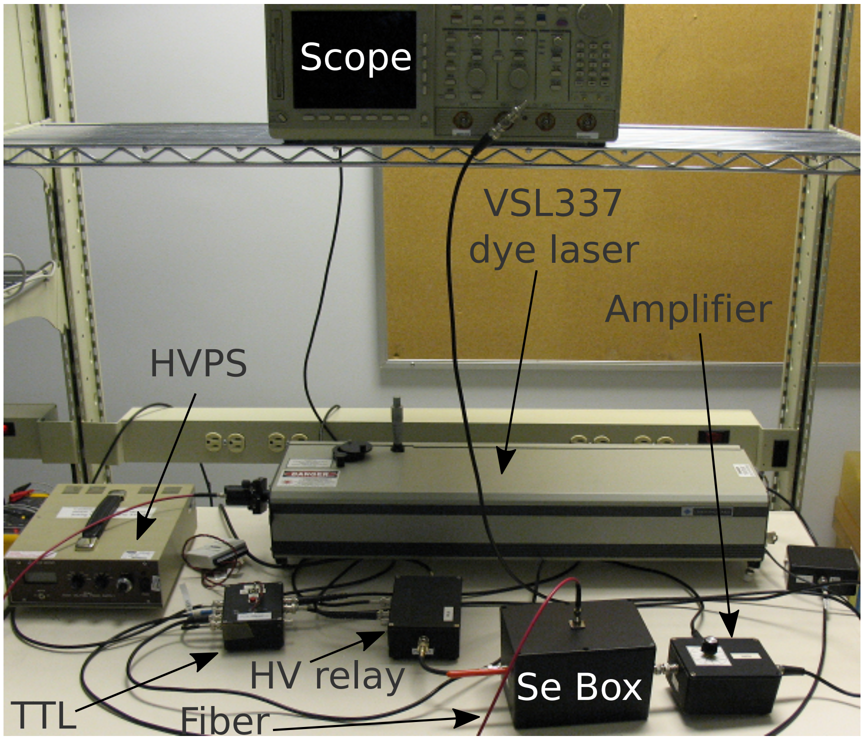

(c)

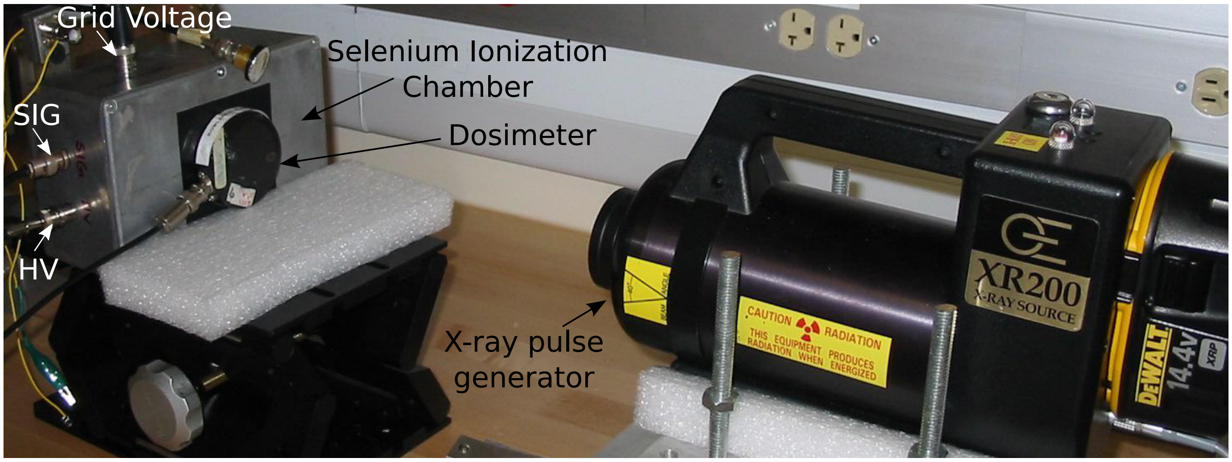

(d)

Figure 6.2: (c) Photograph of the optical TOF setup (courtesy of ANRAD Corporation). (d) Photograph of the x-ray TOF setup.

of carriers from the top surface into the photoconductor with a dye laser tuned to 337 nm wavelength and 5 ns pulse duration. The transient of the carriers was time-resolved and captured on a digital oscilloscope. The incident light intensity was kept relatively low for the *small-signal* case, not to appreciably distort the applied external field, F [78]. In the case of non-dispersive Markoffian transport in a-Se at room-temperature, Scher-Montroll (SM) *universality* of the photocurrent is not applicable and the propagating carrier packet experiences broadening which is described by Gaussian statistics [44], where the position of the peak of carrier distribution coincides with its spatial mean (see Fig. 4.11a in section 4.3.4). This broadening is mainly due to fluctuations of the shallow-trap release time and, in the small-signal case, we can neglect spreading due to mutual Coulomb repulsion of the free charge density. The Gaussian statistics for the dispersion σ_D and the mean carrier displacement ℓ obey time dependencies $\sigma_D \propto t^{1/2}$ and $\ell \propto t$, which yield the well-known relation $\sigma_D/\ell \propto t^{-1/2}$ [45]. Figure 4.11b in section 4.3.4 shows electron and hole photocurrent transient pulses for the fabricated conventional planar device (i.e., without the electrostatic shield) with V_D equal to -500 V and $+500$ V, respectively. Examining the features of Fig. 4.11b, we observe a soft plateau due to inhomogeneous field distribution followed by an exponential decay which is the Gaussian integral of the dispersion. Note that the transit time is identified at a point when the peak of the Gaussian charge packet strikes the collector and the current pulse falls to 50% of its steady value, and accordingly, the measured effective electron and hole mobilities at $T = 295$ °K and $F = 2 \times 10^6$ V m^{-1} are 0.002 and 0.1 cm^2 V^{-1} s^{-1}, respectively.

For the first time, we show unipolar Gaussian TOF transients in Fig. 6.3a using the new unipolar MSSD structure of Fig. 6.1 where the photoconductive film is a non-dispersive disordered solid. The main feature of these time-resolved measurements, parametric in r with $F = 2$ V/μm, is the Gaussian response centred at t_T that verifies the dispersion-limited photoresponse and the time-differential property of the electrostatic shield. Secondly, immediately after optical excitation, we observe a small steady photocurrent induced on the collector due to a small linear change in V_W in the interaction region ($\Delta V_W > 0$), which is expected from the non-ideal V_W distribution of Fig. 5.10. Reexamining this non-ideality in Fig. 5.10 for carriers terminating at the grid, we note that V_W rises from zero to a maximum along the path, and reaches zero again at the grid. This induces a bipolar photocurrent which results in a transient signal but no net charge after integration. The components of this bipolar current, considering a dispersed charge packet and not a single carrier, are a slow positive rectangular pulse due to a gradual positive ΔV_W, and a fast negative (or flipped) Gaussian pulse due to a sharp negative ΔV_W. The top two insets of Fig. 6.3a show the electric field lines from the drift volume terminating on the microstrips and on the collector for r equal to -0.20 and $+0.20$, respectively. Note that for the fabricated device of Fig. 6.1b, the drifting primary carriers, whether terminating on the microstrips or on the collector, do not experience full change in V_W because they become immobilized at the selenium-polyimide (Se-PI) interface before reaching the collector. Thus, the Boltzmann-like transition curve for the normalized collected charge in Fig. 6.3b starts from $\sim$0.1 at $r = -0.2$ and reaches $\sim$0.85 at $r = +0.2$. As illustrated in Fig. 6.3c, when plotted in units of t_T, the normalized standard deviation of the measured Gaussian TOF pulse decreases with longer transit time, by increasing the detector thickness [94] or lowering the external field, according to the expected Gaussian statistics $(\sigma_D/\ell)_{t_T} \propto {t_T}^{-1/2}$.

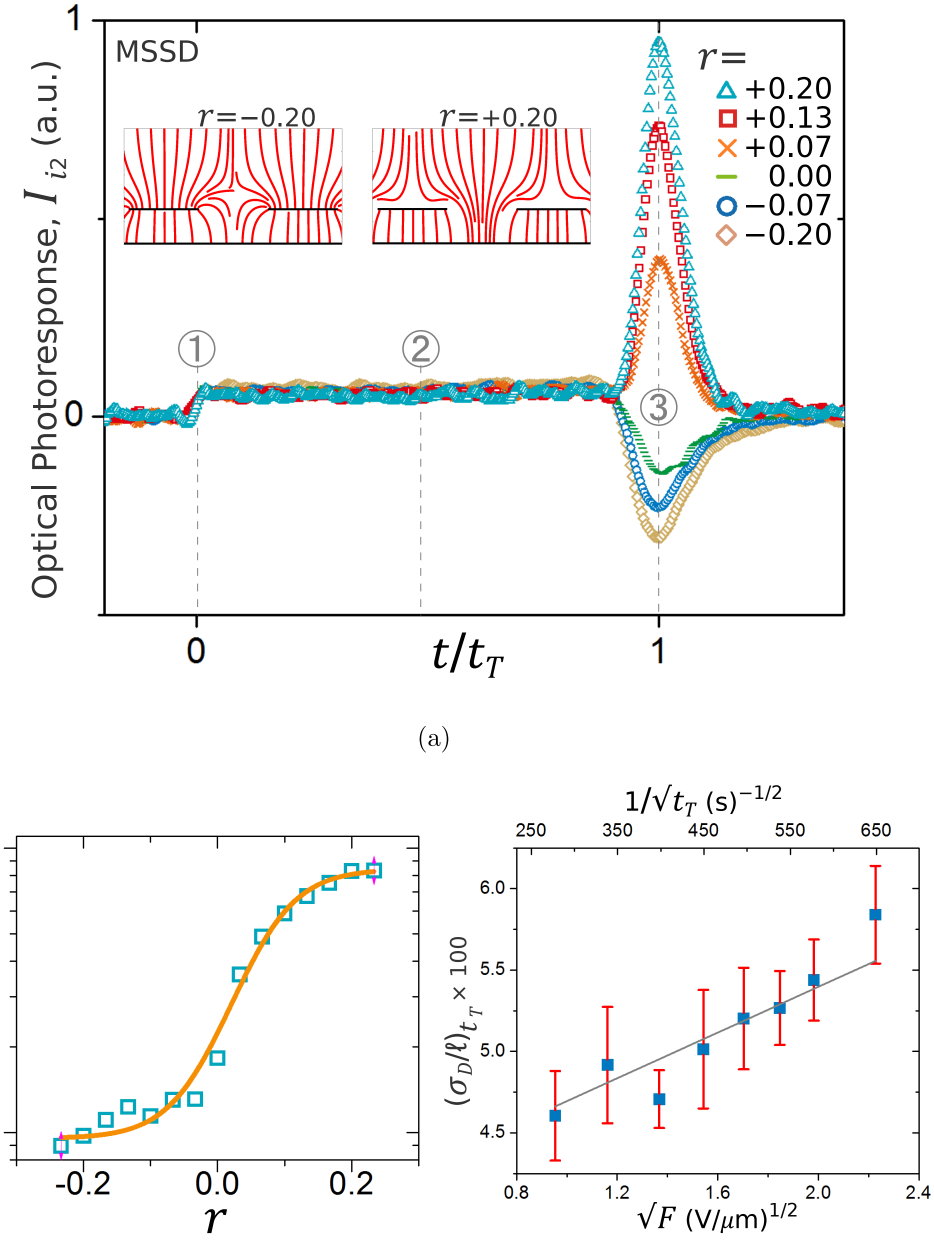

(a)

(b)

(c)

Figure 6.3: (a) Unipolar Gaussian TOF transients of the MSSD, showing the time-differential property of the electrostatically shielding microstrips. (b) Boltzmann-like transition curve for the charge collection efficiency as a function of the normalized microstrip bias. (c) Non-dispersive Gaussian statistics where $(\sigma_D/\ell)_{t_T} \propto {t_T}^{-1/2}$.

6.5 X-ray Time-of-Flight

The second experiment extends the concept of optical TOF to x-rays that is also applicable to a blocking drift electrode [95]. The x-ray TOF is different from optical TOF in that (1) photon absorption can occur throughout the photoconductor, and (2) a Gaussian charge-cloud is formed around the primary interaction site of each absorbed photon (see Fig. 4.13 in section 4.3.4). The dispersion σ_C of the charge cloud obeys the relation $\sigma_C \propto E^2$, where E is the energy of the absorbed x-ray photon [82]. The impulse-like x-ray excitation was tuned to 150 kvP (for a nearly uniform charge-cloud generation density across the photoconductor thickness), 3 mR exposure (for maintaining the small-signal case), and 60 ns pulse duration. The measured time-resolved transients in Fig. 6.4a at $F = 2$ V/μm show a linear decay (i.e., *triangular* response) for the conventional planar device due to carrier neutralization at the collector (or more correctly, carrier immobilization at the Se-PI interface), and a nearly constant response (i.e., *rectangular*) for the new unipolar MSSD, verifying once again the time-differential property of the shield.

Note that the linear decay for the planar device is achieved for a rested a-Se specimen with negligible trapping at low-level excitation; however, in the case of significant trapping an exponential decay is obtained [95]. Also, the spike observed immediately after the x-ray pulse is the result of surface space-charge perturbation. The magnitude of this spike is larger for the MSSD because of its higher field in the detection region, as shown in Fig. 6.4b. Another important feature of the time-differential response is the observed exponential tail, which is no longer a Gaussian-integral but its derivative, representing the actual Gaussian of the last drifting hole packet that was initially generated close to the drift electrode. This response at the tail verifies the dispersion-limited photoresponse. Using the joint spatial distribution function for the two statistically independent carrier spreading variables, total dispersion is given as $\sigma = \sqrt{\sigma_D{}^2 + \sigma_C{}^2}$. The normalized charge spread due to transit dispersion at 2 V/μm is 0.05 (see Fig. 6.3c) and due to x-ray photoelectron cloud ranges from 0.0025 at 20 keV to 0.25 at 150 keV given the relation $\sigma_C \propto E^2$ [82]. Thus, the measured total spreading for the Gaussian tail ($(\sigma/\ell)_{t_T}$=0.07), considering an average photon energy of 60 keV for the 150 kVp spectrum, is well within expectation.

6.6 Temporal Response in Pulse Mode

We used single photon excitations to measure the detector's signal risetime as a figure-of-merit for the temporal response in pulse mode. Recall from Fig. 4.9 that the magnitude of the collected charge for a conventional planar detector without the grid is highly depth dependent during hole transit time and that a unipolar device with a strong near-field effect can substantially reduce signal risetime. Also, recall from Fig. 4.14 that the performance improvement factor in the best case is limited by the dispersion of the higher-mobility carrier-cloud. All theoretical predictions are verified experimentally in Fig. 6.5. For a-Se planar detector, signal risetime has a faster component due to the drift of holes and a slower component due to the drift of electrons with risetimes ranging from hole-only 1.2 μs to electron-only ~70 μs. However, for a-Se MSSD, depth-independent risetime is a mere 200 ns. This shows a reduction in signal risetime by a factor of 350, comparing hole-dispersion-limited response with that of electron-transit-time-limited.

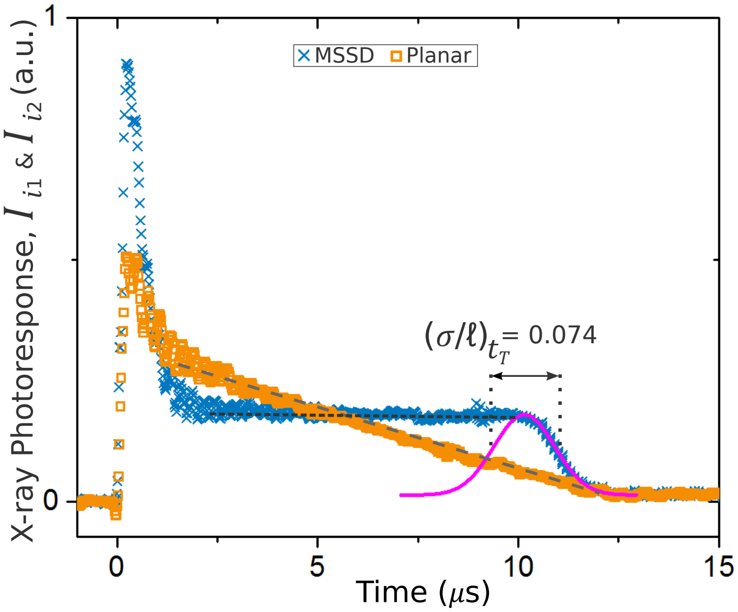

(a)

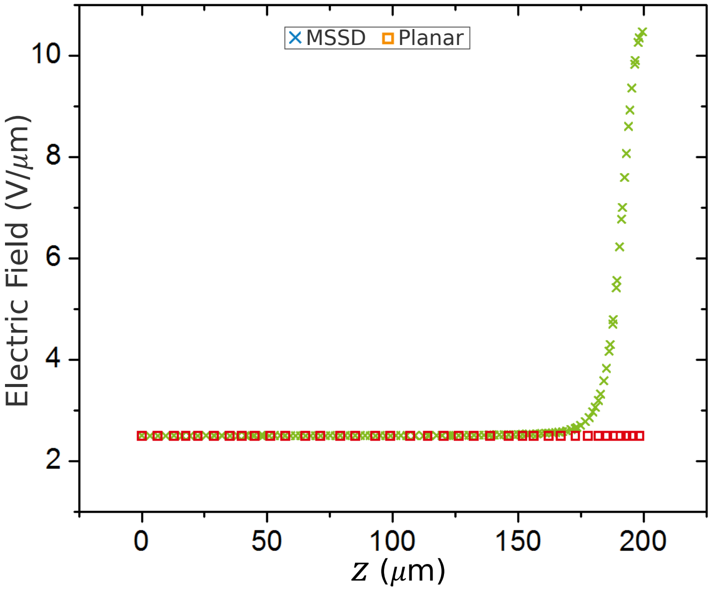

(b)

Figure 6.4: (a) Unipolar rectangular x-ray TOF of the MSSD, showing once again the time-differential property of the electrostatically shielding microstrips, compared to the triangular response for the planar device. (b) Electric field distribution in the bulk.

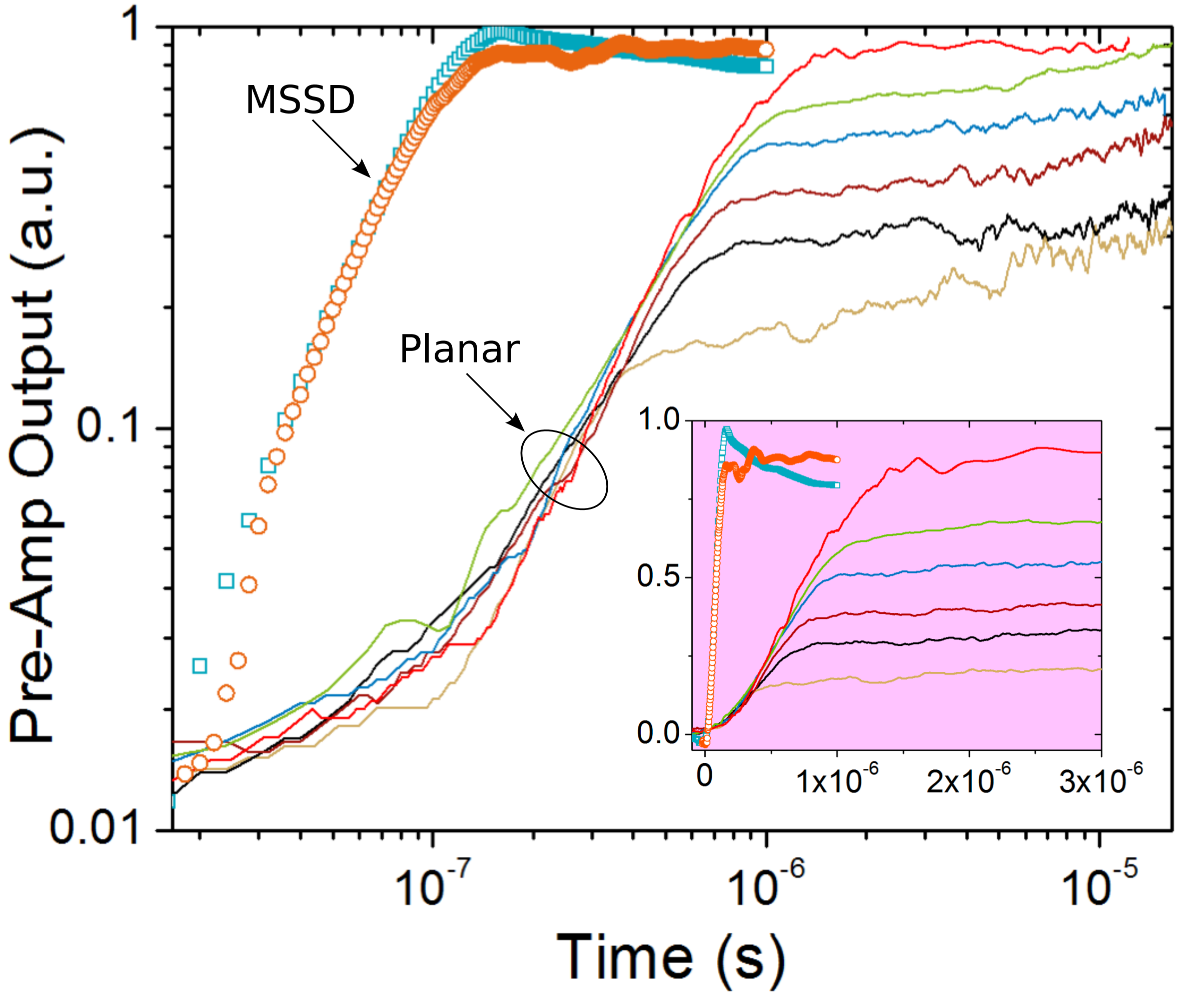

Figure 6.5: Collected charge as a function of time at $F = 13$ V/μm for a single gamma-ray photon interaction. For the conventional planar detector, signal risetime is highly depth dependent and in the worst-case it is electron-transit-time-limited. However, for the unipolar MSSD with a strong near-field effect, signal risetime is hole-dispersion limited.

6.7 Conclusions

For device characterization, we considered three experiments. First, a sheet of excess carriers was photoinduced close to the drift electrode with an impulse-like optical laser excitation for time-of-flight (TOF) transient photoconductivity measurement. In the case of non-dispersive Markoffian transport in a-Se at room-temperature, the propagating photoinduced carrier packet experiences broadening which is described by Gaussian statistics. For the first time, we showed unipolar Gaussian TOF transients using the new MSSD structure, instead of a rectangular TOF with a Gaussian-integral at the tail which is a typical response for a conventional planar device. The Gaussian response centred at the hole transit-time verified the time-differential property of the electrostatic shield and the practicality of the dispersion-limited photoresponse. Second, Gaussian carrier clouds were generated uniformly across the bulk with an impulse-like high energy x-ray beam. The measured time-resolved transients showed a linear decay (i.e., triangular response) for the conventional planar device and a nearly constant rectangular response for the new unipolar MSSD, proving once again the time-differential property of the shield to impulse excitations. Finally, we used single-photon excitations to probe detector's temporal response in pulse mode for photon counting. For the MSSD, we obtained a depth-independent signal for photon absorption across the bulk and a reduction in signal risetime by a factor of 350, comparing performance limiting factors being hole-dispersion for the MSSD and electron-transit-time for the conventional planar device.

Chapter 7

Unipolar Charge Sensing in Energy-Integrating Imagers

7.1 Introduction

Energy integrating systems, aside from their limitations, are still being actively pursued by flat-panel detector (FPD) manufacturers as a basis technology for commercially available area-imaging x-ray tomosynthesis systems. This is because of two technological advances: 1) the availability of cost-effective, large area a-Si TFT readout panels, and 2) successful and reliable coupling of the evaporated amorphous selenium photoconductor to these large-area readout panels. Thus, this chapter investigates incremental performance improvements provided by the proposed unipolar photoconductors in energy integrating mode, which are higher charge collection efficiency, higher spatial resolution, and lower image lag.

7.2 Theory

7.2.1 Sensitivity

The sensitivity model of direct conversion radiation detectors has been reported in literature [96], [97], [98], [99]. However, our focus is the advantage presented by preferential sensing of faster carriers for improved charge collection efficiency, and consequently, increased x-ray sensitivity. Thus, unlike all sensitivity analysis presented in the past, we cannot assume that the spatial derivative of the weighting potential distribution is a constant. The x-ray sensitivity of a photoconductor is defined as

$$S = \frac{Q_c}{AX} \tag{7.1}$$

where Q_c is the total collected charge under small-signal operating conditions [98], A is the pixel area, and X is the x-ray exposure. Considering spatial x-ray absorption profile, temporal carrier trapping, and negligible bulk recombination, the continuity equation for carrier concentration is given by

$$\frac{\partial c(z,t)}{\partial t} = -\mu_c F \frac{\partial c(z,t)}{\partial z} - \frac{c(z,t)}{\tau_c} \tag{7.2}$$

where $c(z,t)$ is the carrier concentration at space z and time t, μ_c is the effective carrier mobility, F is the applied bias per detector thickness (or the electric field), and τ_c is the effective carrier lifetime (or the deep trapping time).

The initial carrier concentration at the time of x-ray interaction, or $c(z,0)$ is equal to

$(\alpha_{en}E\phi_0/W_{\pm})\exp(-\alpha z)$, where α is the linear attenuation coefficient, α_{en} is the energy absorption coefficient, E is average energy of the incident x-ray spectrum, ϕ_0 is the mean x-ray fluence (photons per unit area), and $W_{\pm}$ is the electron-hole pair creation energy. Thus, solving the continuity equation using the preceding initial condition and under the assumption that higher mobility carriers are moving towards the pixel electrode yields

$$c_+(z,t) = \begin{cases} (\alpha_{en}E\phi_0/W_{\pm})\exp(-\alpha(z-\mu_+Ft))\exp(-t/\tau_+), & \mu_+Ft < z < L \\ 0, & z < \mu_+Ft \text{ and } z > L \end{cases} \tag{7.3}$$

$$c_-(z,t) = \begin{cases} (\alpha_{en}E\phi_0/W_{\pm})\exp(-\alpha(z+\mu_-Ft))\exp(-t/\tau_-), & 0 < z < L-\mu_-Ft \\ 0, & z < 0 \text{ and } z > L-\mu_-Ft \end{cases} \tag{7.4}$$

Using Eq. 7.3 and Eq. 7.4, the total collected charge in the external circuit due to the carrier concentration and the weighting potential distribution is

$$Q_c = qAF\left[\mu_+\int_0^{L/\mu_+F}\int_{\mu_+Ft}^{L} c_+(z,t)\frac{\mathrm{d}V_W}{\mathrm{d}z}\,\mathrm{d}z\,\mathrm{d}t + \mu_-\int_0^{L/\mu_-Ft}\int_0^{L-\mu_-Ft} c_-(z,t)\frac{V_W}{\mathrm{d}z}\,\mathrm{d}z\,\mathrm{d}t\right] \tag{7.5}$$

where $\mathrm{d}V_W/\mathrm{d}z$ for pixels without the near-field effect is constant and equal to $1/L$.

Finally, the normalized sensitivity s is the product of the charge collection efficiency and the quantum efficiency η

$$s = \frac{Q_c}{Q_0}\eta = \frac{Q_c}{q\alpha_{en}E\phi_0A/\alpha W_{\pm}} \tag{7.6}$$

where Q_0 is the initial number of electron-hole pairs (ehp) generated which equals $q\alpha_{en}E\phi_0 A\eta/\alpha W_\pm$ and η equals $1 - \exp(-\alpha L)$.

7.2.2 Detective quantum efficiency

The detective quantum efficiency (DQE) of an imaging system is a valuable performance metric in that it characterizes each stage for its ability to transfer the input signal and noise, and is defined as

$$\mathrm{DQE} = \frac{\mathrm{SNR}_{\mathrm{out}}^2}{\mathrm{SNR}_{\mathrm{in}}^2} \tag{7.7}$$

where SNR is the signal-to-noise ratio. The DQE analysis of our new imaging detector is based on the x-ray system model presented previously by Rabbani [100], [101] and Cunningham [102]. Figure 7.1 shows the cascaded linear system model for a direct x-ray photoconductor consisting of three amplification stages (absorption, conversion, and charge collection) and an additive readout electronic noise stage. Assuming that all the amplification stages are stationary random processes characterized by their mean $\overline{m}$ and variance σ^2, the signal and the noise transfer equations are [100]

$$S_i(f) = \overline{m}_i S_{i-1}(f) \tag{7.8}$$

$$N_i(f) = \overline{m}_i^2 N_{i-1}(f) + \sigma_i^2 S_{i-1}(f) \tag{7.9}$$

where $S_i(f)$ and $N_i(f)$ are the signal spectrum and the noise power spectrum (NPS) of the i^{th} stage at the spatial frequency f, respectively. Assuming negligible signal spreading due to the reabsorption of the K-fluorescent photons and the lateral diffusion of the photon-

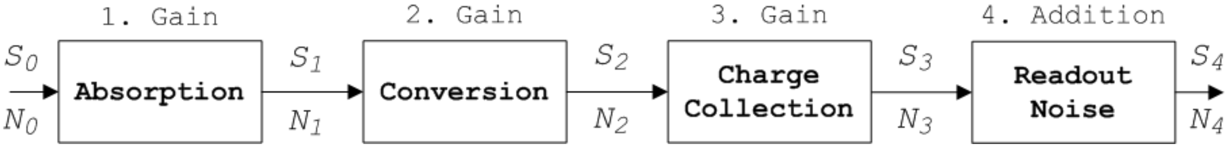

Figure 7.1: Linear system model for direct x-ray detection.

generated carriers, the amplification stages become independent of the spatial frequency. Thus, the analysis in this section examines the transfer characteristics at $f = 0$. Note that the input signal S_0 to the system is the mean x-ray fluence that obeys the Poisson distribution. Thus, the input noise density N_0 is equal to S_0.

The x-ray absorption is a binary selection process with binomial probability distribution [103] where the mean and the variance of its gain are depth independent and are given by

$$\overline{m}_1 = \eta \tag{7.10}$$

$$\sigma_1^2 = \eta(1 - \eta) \tag{7.11}$$

The study of the x-ray conversion gain in amorphous Selenium (a-Se) is to determine the photogeneration efficiency in the presence of the geminate [104] or the columnar [105] recombination processes, or both [60]. The photoconversaion gain factor, $W_{\pm}$, of a-Se has been measured using the pulse-height spectroscopy technique [60]. Results show the dependence of $W_{\pm}$ on both the applied electric field, F, and the photon energy, E, over the diagnostic energy range. For our analysis of the second gain stage, however, we use the mean value of $W_{\pm}$ reported in Ref. [60] for a given F and E, and neglect the wide spectrum width attributed to the stochastic geminate and columnar recombination processes. Thus, the mean number of the drifting EHP generated in the conversion stage is

$$\overline{m}_2(z) = \frac{E_{ab}(z)}{W_{\pm}} \tag{7.12}$$

The depth dependency of the absorption energy E_{ab}, and consequently $\overline{m}_2$, is because of the emission of K-fluorescent photons and their reabsorption probability $P_r(z)$ at an interaction point z. Though the exact calculation of E_{ab} is a complex task, a simple yet effective model is represented below [106]

$$E_{ab}(z) = (\alpha_{en}/\alpha)E + f_{ph}P_K Y_K E_K P_r(z) \tag{7.13}$$

where f_{ph} is the fraction of photoelectric interaction from total attenuation, P_K is the probability of photoelectric interactions with K-shell electrons, Y_K is the K-shell fluorescent yield, and E_K is the mean energy of K-fluorescent photons. Also, assuming isotropic emission of such characteristic x-rays, the reabsorption probability is given by [107]

$$P_r(z) = 1 - \frac{1}{2}\left(\int_1^{\infty} e^{-\alpha(d-z)w} w^{-2}\,\mathrm{d}w + \int_1^{\infty} e^{-\alpha z w} w^{-2}\,\mathrm{d}w\right) \tag{7.14}$$

where α in Eq. 7.14 is for E_K and not the average incident photon energy E. The statistical spread around for uncorrelated partitioning of the absorbed energy into ionizing and non-ionizing mechanisms (i.e., Fano-factor ≈ 1) is given by the Poisson distribution

$$\sigma_2^2(z) = \overline{m}_2(z) \tag{7.15}$$

The advantage of unipolar charge sensing using the Frisch grid technique is realized in the charge collection stage. The gain of this stage is analyzed for the following two cases: 1) a large-pixel detector without the near-field effect and 2) an ideal unipolar charge sensing detector. The mean and the variance for case 1 has been previously reported by calculating the first and the second moment using the joint probability density function for the two statistically independent random deep trapping variables of electrons and holes [108]. We summarize the results for case 1 and utilize the same technique to calculate the mean and the variance of the charge collection stage for the unipolar photoconductor with a strong near-field effect. As shown in Fig. 7.2a, for a photon interaction at location z inside the detector bulk, the generated low-mobility carriers (electrons in this case) move towards the common electrode with instantaneous position z', and high-mobility carriers (holes in this case) drift towards the grid and the pixel electrode with instantaneous position z''. Thus, the gain random variables for case 1 and case 2, as depicted in Fig. 7.2b and Fig. 7.2c, respectively, are given as

$$\text{case 1: } g_3(z,\, z',\, z'') = \begin{cases} 1, & z' \leq 0 \text{ and } z'' \geq L \\ (L - z')/L, & 0 < z' < z \text{ and } z'' \geq L \\ z''/L, & z' \leq 0 \text{ and } z < z'' < L \\ (z'' - z')/L, & 0 < z' < z \text{ and } z < z'' < L \end{cases} \tag{7.16}$$

$$\text{case 2: } g_3(z'') = \begin{cases} 1, & z'' \geq L \\ 0, & \text{elsewhere} \end{cases} \tag{7.17}$$

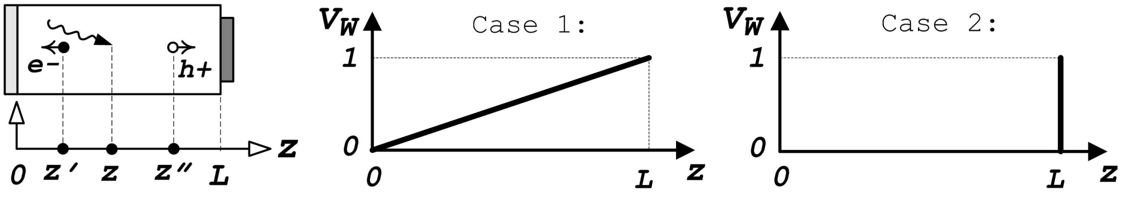

(a) (b) (c)

Figure 7.2: (a) The cross section of a direct conversion x-ray detector. The weighting potential distribution for (b) a large-pixel detector without the near-field effect and (c) an ideal unipolar charge sensing detector.

Hence, solving the first moment of Eq. 7.16 and Eq. 7.17 yields the mean of the collection stage

$$\text{case 1: } \overline{m}_3(z) = \frac{1}{L}\left[\frac{1}{\beta_-}\left(1-\exp\left(-\beta_- z\right)\right) + \frac{1}{\beta_+}\left(1-\exp\left(-\beta_+\left(L-z\right)\right)\right)\right] \tag{7.18}$$

$$\text{case 2: } \overline{m}_3(z) = \exp\left(-\beta_+\left(L-z\right)\right) \tag{7.19}$$

where $\beta_{+/-}$ is the linear trapping attenuation coefficient for higher/lower mobility carriers and is equal to $\left(\mu_{+/-}\tau_{+/-}F\right)^{-1}$. Also, the variance is the second moment minus the squared mean

$$\text{case 1: } \sigma_3^2(z) = \left[\begin{array}{c} \frac{1}{\beta_-^2} - \frac{1}{\beta_-^2}\exp\left(-2\beta_- z\right) - \frac{2z}{\beta_-}\exp\left(-\beta_- z\right) + \frac{1}{\beta_+^2} - \frac{1}{\beta_+^2}\exp\left(-2\beta_+\left(L-z\right)\right) \\ -\frac{2L}{\beta_+}\exp\left(-\beta_+\left(L-z\right)\right) + \frac{2z}{\beta_+}\exp\left(-\beta_+\left(L-z\right)\right) \end{array}\right] \tag{7.20}$$

$$\text{case 2: } \sigma_3^2(z) = \exp\left(-\beta_+\left(L-z\right)\right) - \exp\left(-2\beta_+\left(L-z\right)\right) \tag{7.21}$$

The fourth stage is an additive white Gaussian noise (AWGN) with zero mean value.

Its variance σ_4^2 is calculated from the total input referred noise spectral density and the bandwidth of the readout electronics. Finally, the DQE at the detector output is

$$DQE(0) = \frac{S_4^2(0)/N_4}{S_0^2(0)/N_0} = \frac{S_3^2(0)/N_4}{\phi_0^2/\phi_0} = \frac{S_3^2(0)}{\phi_0\left(N_3 + \sigma_4^2\right)} \tag{7.22}$$

where the signal S_3 and the noise density N_3 are

$$S_3(0) = \eta\phi_0 \int\limits_0^L \overline{m}_2(z)\overline{m}_3(z)\rho(z)\ \mathrm{d}z \tag{7.23}$$

$$N_3(0) = \eta\phi_0 \int\limits_0^L \overline{m}_2(z)\left[\overline{m}_3^2(z)\overline{m}_2(z) + \overline{m}_3^2(z) + \sigma_3^2(z)\right]\rho(z)\ \mathrm{d}z \tag{7.24}$$

and $\rho(z)$ is the probability density function for the random x-ray interaction inside the detector bulk

$$\rho(z) = (\alpha/\eta)\exp\left(-\alpha z\right) \tag{7.25}$$

7.2.3 Modulation transfer function

The spatial resolution of an imager is characterized by the modulation transfer function or MTF, which describes the ability of the system to process the signal. The MTF plot illustrates image degradation and blurring as a function of spatial frequency in response to a stimulus. A practical way to measure MTF is to use a linear stimulus by exposing the detector to x-ray through a narrow lead or tungsten slit, for example. The slit, if aligned properly to the x-ray tube focal spot, collimates the radiation into a very thin line and the system's response is recorded as the line spread function (LSF). For theoretical purposes, however, we can calculate the point spread function (PSF) based on the detector's response to a point (or point-like) stimulus. The MTF is then computed by the Fourier transform of the PSF or the LSF.

The intrinsic resolution of x-ray photoconductors has been previously investigated and the major contributors to signal spreading and loss of spatial resolution have been identified [82], [109]. Amongst these, signal spreading due to charge induction of bulk-trapped carriers on neighbouring pixels is of interest in this section. As shown in Fig. 7.3, because carrier trapping occurs mostly in the interaction region, signal spreading is shielded by the grid and charge induction of trapped carriers happens on the grid rather than on the collecting pixels. Hence, the imager's resolution is improved. The degree of insensitivity to trapped charge induction depends on the weighting potential distribution and how close it is to the ideal unipolar case of Fig. 7.2c.

The net trapped space charge distribution, c_t, based on the radiation induced carrier concentration of Eq. 7.3 and Eq. 7.4, and under small-signal operating conditions, is given by [110]

$$c_t(z) = \left[\int\limits_0^{z/\mu_+ F} \frac{c_+(z,t)}{\tau_+}\,\mathrm{d}t - \int\limits_0^{(L-z)/\mu_- F} \frac{c_-(z,t)}{\tau_-}\,\mathrm{d}t \right], \quad 0 < z < L \tag{7.26}$$

To calculate the point spread function, we consider a point-like stimulus with a finite radius r_s incident on the centre pixel, as shown in Fig. 7.4. The resulting trap-induced charge density σ_t on the pixel plane is calculated by constructing an infinite series of images

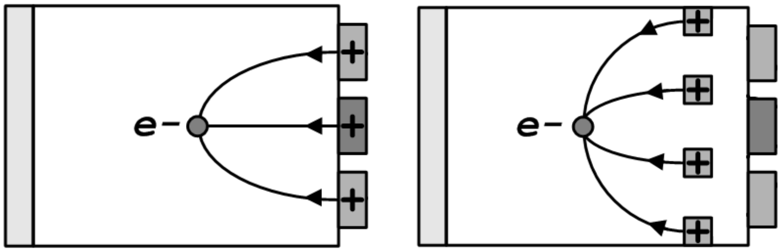

(a) (b)

Figure 7.3: Trapped carriers in the photoconductor induce charge on (a) the collecting pixels and (b) the shielding grid. The grid forms an electrostatic barrier to shield against the blurring effect of trapped carriers.

of a trapped carrier between two parallel conducting planes [111]

$$\sigma_t(x,y,d) = \begin{array}{c} \frac{q}{2\pi}\frac{-d}{\left(x^2+y^2+d^2\right)^{1.5}} \\ +\frac{q}{2\pi}\sum_{n=1}^{\infty}\left[\frac{-2n(L-Z_g)-d}{\left(x^2+y^2+(2n(L-Z_g)+d)^2\right)^{1.5}}+\frac{2n(L-Z_g)-d}{\left(x^2+y^2+(2n(L-Z_g)-d)^2\right)^{1.5}}\right] \end{array} \tag{7.27}$$

where d is the distance of the trapped charge from the pixel plane along the $(0,0,z)$ line and equals $L-z$, and Z_g is the grid distance from the non-collecting common electrode (note that for regular detectors without the shielding grid, Z_g is equal to 0). Consequently, the total trap-induced charge density σ_{tt} due to a point-like stimulus is

$$\sigma_{tt}(x,y) = \pi r_s^2 \int_0^{L-Z_g} c_t(z)\sigma_t(x,y,L-z)\,\mathrm{d}z \tag{7.28}$$

A two-dimensional view of the point spread function can be constructed by energy-integrating

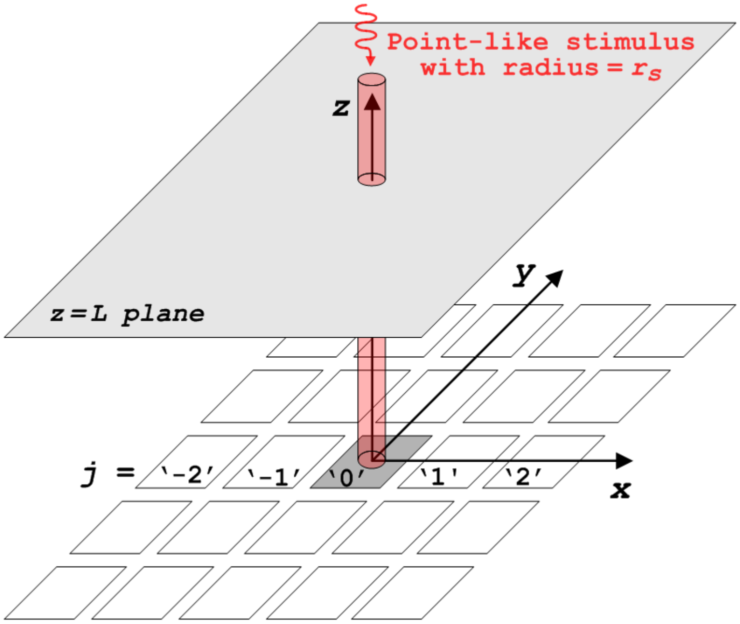

Figure 7.4: A schematic diagram for calculating the MTF. A point-like stimulus with radius r_s is incident on the pixel centred at $(0, 0, 0)$ and trapped carriers along the $(0, 0, z)$ line cause image blur by inducing charge on the neighbouring pixels.

σ_{tt} over the pixels along the $(x, 0, 0)$ line

$$\mathrm{PSF}(j) = \begin{cases} Q_c + \int_{-a/2}^{a/2} \int_{-a/2}^{a/2} \sigma_{tt}(x, y)\ \mathrm{d}x\ \mathrm{d}y, & j = 0 \\ \int_{-a/2}^{a/2} \int_{j-a/2}^{j+a/2} \sigma_{tt}(x, y)\ \mathrm{d}x\ \mathrm{d}y, & j \neq 0 \end{cases} \tag{7.29}$$

where Q_c is calculated using Eq. 7.5 for the area of the point-like stimulus (i.e., $A = \pi r_s^2$). Finally, the Fourier transform of the PSF yields the imager's MTF.

7.3 Results and Discussions

The results presented in this section are mostly the application of the theory of section 7.2 to positively biased amorphous selenium (a-Se) photoconductors, where the subscript $+/-$ for higher/lower mobility carrier corresponds to hole/electron. Also note that the results are representative of the performance improvements provided by direct-detection solid-state unipolar charge sensing photoconductors with a strong near-field effect using electrostatically shielding grids.

7.3.1 Sensitivity

Preferential sensing of faster carriers by establishing the intermediate grid as an electrostatic shield inside a radiation detector improves charge collection efficiency, and consequently, increases x-ray sensitivity. Figure 7.5 shows the universal sensitivity curves versus normalized photon interaction depth $\Delta = 1/(\alpha L)$ for various normalized carrier schubwegs

$\lambda_{+/-} = \mu_{+/-}\tau_{+/-}F/L$, using Eq. 7.5 and Eq. 7.6. Figure 7.5a illustrates higher trapping for lower λ, and thus, lower sensitivity is observed. For the hole-only selenium detector, decreasing λ_+ while keeping λ_- at infinity exaggerates such reduction in sensitivity, as shown in Fig. 7.5b, because charge induction on the collecting pixel electrode is due to the movement of holes only and the benefit of long electron lifetime is not gained. However, for the same hole-only selenium detector, decreasing λ_- while keeping λ_+ at infinity has no effect on the detector's charge collection process, and thus, the same sensitivity curves are realized, as shown in Fig. 7.5b. An important point to note here is that one may optimize the mobility-lifetime product for the faster carrier, with less concern about possible degradation of that of the slower carrier. In a-Se, for example, adding less than a percent Arsenic (As) improves the lifetime of electrons while acting as traps for holes and degrades hole lifetime, and vice versa for adding parts per million of Chlorine (Cl) [96]. Thus, one may choose a composition of As and Cl that yields the highest achievable hole lifetime.

7.3.2 Detective quantum efficiency

As mentioned earlier, the advantage of unipolar charge sensing is realized in the charge collection stage, which means higher DQE. We calculate the transfer characteristics of a-Se detectors at zero spatial frequency, i.e., DQE(0), for fluoroscopy imaging applications, using Eq. 7.22. The incident x-ray spectrum is a 70kVp beam (as recommended by IEC Standard 1267 - radiation condition RQA5) hardened with 23.5 mm Aluminum (Al) filtration, which has a mean energy E of 52.1 keV. The X-ray exposure X for real-time fluoroscopy ranges from $0.1 - 10$ μR with a mean exposure level of 1 μR [112]. The a-Se carrier transport

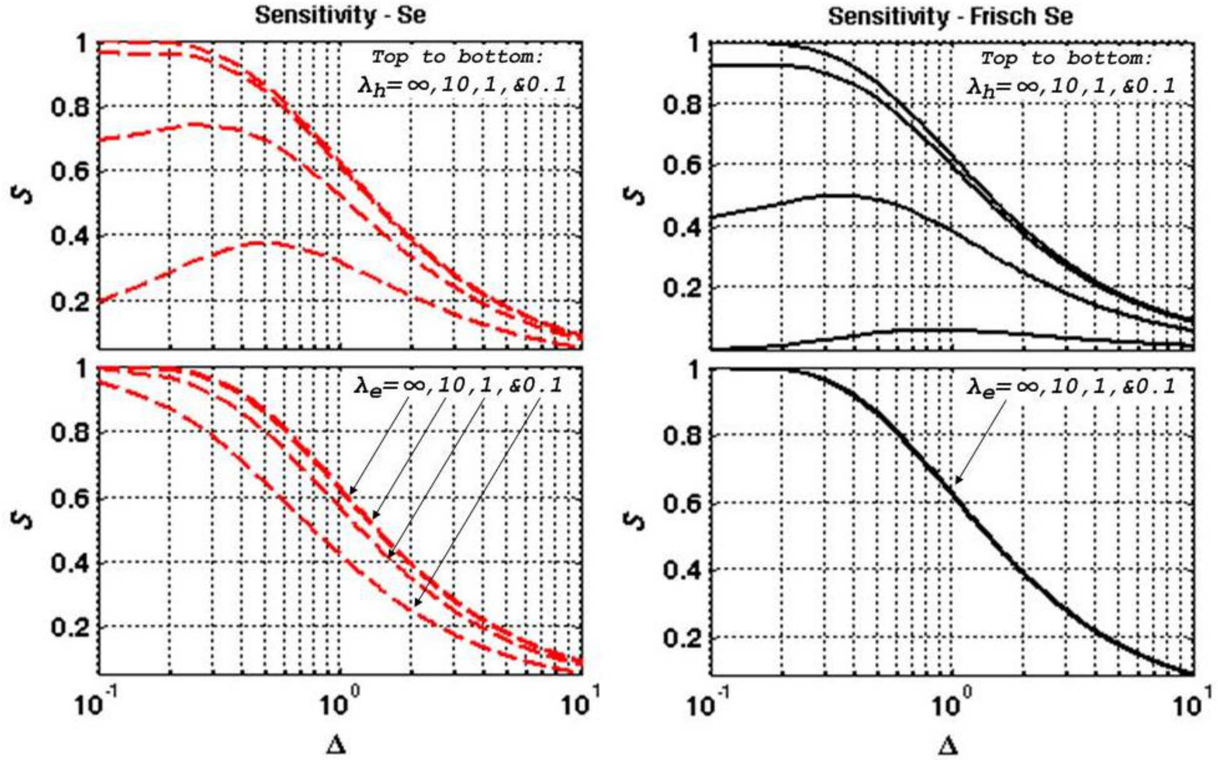

(a) (b)

Figure 7.5: Normalized x-ray sensitivity versus normalized photon interaction depth for various hole (top) and electron (bottom) schubwegs using (a) a regular a-Se detector and (b) a hole-only a-Se detector with the electrostatic shield.

properties used are $\mu_+ = 0.14$ cm^{2}V^{-1}s^{-1}, $\tau_+ = 100$ μs, $\mu_- = 0.003$ cm^{2}V^{-1}s^{-1}, $\tau_- = 200$ μs. The detector is assumed to have 100% effective fill factor, with a pixel aperture of 150 μm, and is operated at $F = 10$ v/μm with EHP creation energy $W_\pm$ of approximately 50 eV. The X-ray attenuation and K-fluorescent related parameters, which are α, α_{en}, f_{ph}, P_K, Y_K, and E_K, are taken from Table 1 in Ref. [106]. The root-mean-square (rms) value of additive readout noise is taken to be around 2500 ehp (i.e., $\sigma_4 \approx 2500$ ehp).

Figure 7.6a shows the normalized collected charge (Q_c/Q_0) versus detector thickness at $X = 1$ μR, where significant improvement in charge collection is observed by switching the polarity of the high voltage bias from negative to positive. Thick selenium films suffer from schubweg limited electron transport and collection efficiency is reduced due to significant electron trapping. Switching the high voltage bias from negative to positive causes the collection process to depend mostly on long-ranged hole transport with reduced trapping, and thus, the collection efficiency is improved. In addition, further improvement in charge collection efficiency can be achieved by completely erasing the dependency of the charge collection process to short-ranged electrons using a positively biased, hole-only a-Se detector. Consequently, the highest possible detective quantum efficiency, given the detector parameters and the operating conditions, is obtained from the hole-only detector design with the shielding grids, as shown in the DQE(0) versus detector thickness and x-ray exposure plots in Fig. 7.6b and Fig. 7.6c, respectively.

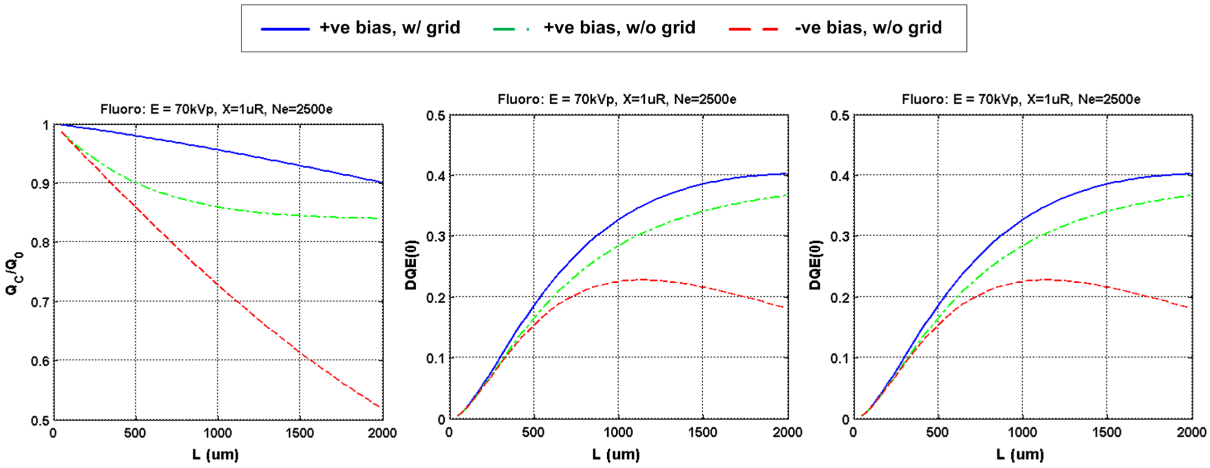

(a) (b) (c)

Figure 7.6: (a) Normalized collected charge versus detector thickness at 1 μR exposure. DQE(0) versus (b) thickness and (c) x-ray exposure. Note that simulations are performed for a negatively biased, a positively biased, and a positively biased hole-only a-Se detectors.

7.3.3 Modulation transfer function

The trap-induced blurring, characterized by the point spread function (PSF), is calculated using Eq. 7.29 for a point-like stimulus of radius r_s, incident at the centre of a pixel, and the spatial resolution is calculated by taking the Fourier transform of the PSF. To validate the PSF-based MTF model, our theoretical curves are fitted to published experimental results for polycrystalline Cadmium Zinc Telluride (CZT) [113] and polycrystalline Mercuric Iodide (HgI2) [114] radiation detectors. Fig. 7.7a shows the MTF results of a CZT detector with $L = 300$ μm, $a = 150$ μm, $F = 0.25$ V/μm, while exposed to a 80 kV x-ray beam with 26 mm Al filtration [113]. For our model, CZT electron and hole $\mu\tau$ products used are 2.4×10^{-4} cm^{2}V^{-1} and 3.2×10^{-6} cm^{2}V^{-1}, respectively [115].

Figure 7.7b shows the MTF results of a HgI$_2$ detector with $L = 130$ μm, $a = 139$

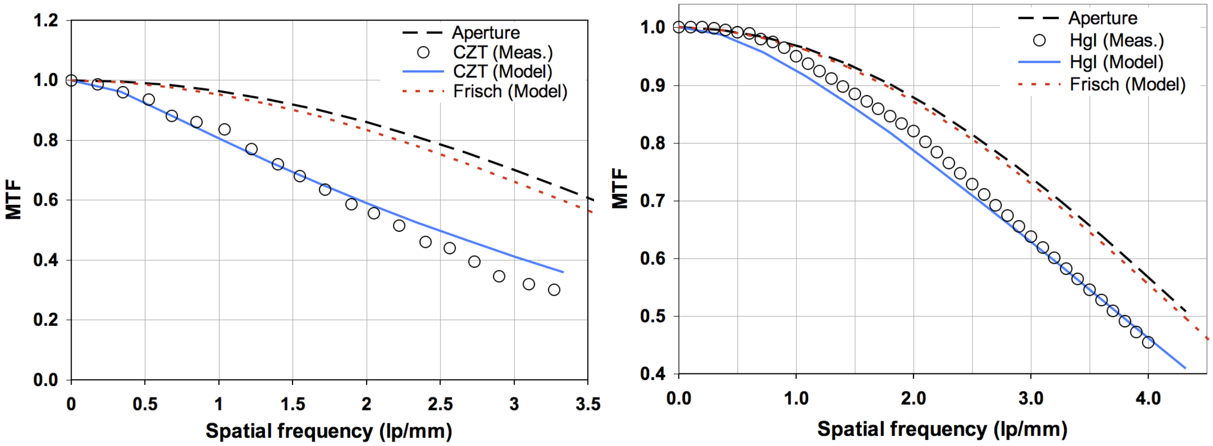

(a) (b)

Figure 7.7: MTF simulations for (a) a Poly-crystalline CZT with $L = 300$ μm and (b) a poly-crystalline $\mathrm{HgI_2}$ with $L = 130$ μm. The theoretical model is based on the calculated trap PSF while the measured result is the pre-sampling MTF from the captured LSF using a tungsten slit. The modelled MTFs are calculated for detectors without and with the shielding grid, where Z_g is equal to 0 and $0.85L$, respectively. (Note: Measured results are extracted from Fig. 10 in Ref. [113] and Fig. 7 in Ref. [114] for parts (a) and (b), respectively.)

μm, $F = 0.2$ V/μm, and electron and hole $\mu\tau$ products of 5×10^{-5} cm^{2}V^{-1} and 1×10^{-6} cm^{2}V^{-1}, respectively, while exposed to a 60 kV x-ray beam [114], [116]. Theoretical MTF results for regular detectors without the shielding grid ($Z_g = 0$) show good agreement with the measured data. Also, modelled results of detectors with the grid ($Z_g = 0.85L$) show improved spatial resolution with near aperture MTFs.

Our PSF-based MTF model is also applied to a-Se detectors, for fluoroscopic imaging applications, with $L = 1000$ μm, $a = 150$ μm, $F = 10$ V/μm, and electron and hole $\mu\tau$ products of 2×10^{-6} cm^{2}V^{-1} and 10^{-5} cm^{2}V^{-1}, respectively, while exposed to a 70 kV x-ray beam with 21mm Al filteration [117], [118]. The PSF plots in Fig. 7.8a show, for the same trap carrier density, reduced signal spreading on the Frisch selenium pixels (where $Z_g = 0.85L$), because the grid shields traps inside the interaction region from being sensed by the collecting pixel electrodes. The improved spatial resolution is illustrated by the modelled MTFs in Fig. 7.8b. Also shown in Fig. 7.8b are measured data from real-time a-Se fluoroscopic detectors. A relatively higher reduction in MTF for type-B detector is attributed to trapped charge in the blocking layer between the pixel electrodes and the a-Se film [119]. The effect of these interface traps is not included in our model and we observe discrepancy between our modelled MTF and type-B measured results. For type-A detector, which was optimized to reduce interface traps by reducing the thickness of the blocking layer on the pixels [117], our model is an adequate representation of the measured results. Finally, for a regular fluoroscopic a-Se detector (where $Z_g = 0$), we observe close agreement between the results of our PSF-based model in FIG. 12 and that of the composite LSF technique [120], [110] shown in Fig. 7 in Ref. [121].

7.3.4 Comments on image lag

Lag is a temporal imaging characteristic of an x-ray imaging detector, and manifest itself as the carry-over image charge, from previous x-ray exposures, into subsequent image frame [19]. For amorphous selenium detectors, most holes can drift all the way across the photoconductor and contribute fully to the output signal, but short-ranged electrons are strongly trapped because of their lower $\mu\tau$ product. Time-of-flight transient photoconductivity measurements have showed that a net negative space charge is created inside a-Se after x-ray exposure [122]. Although no conclusive evidence has been presented to show

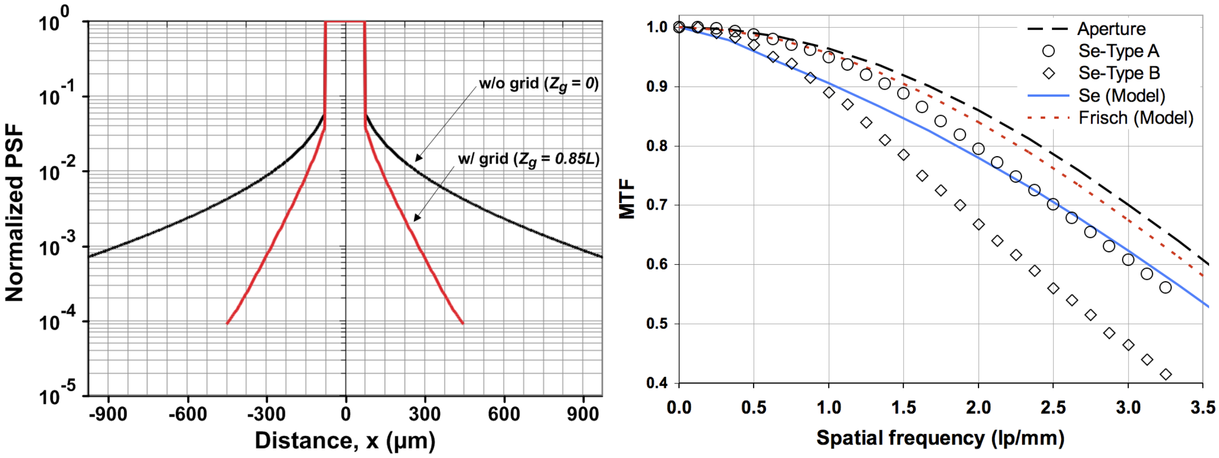

(a) (b)

Figure 7.8: The modelled trap (a) PSF and (b) MTF for a negatively biased a-Se detector with $L = 1000$ μm without and with the shielding grid, where Z_g is equal to 0 and $0.85L$, respectively. (Note: Measured results are extracted from Fig. 8 and Fig. 9 in Ref. [117].)

the dominant mechanism for lag in p-i-n a-Se detector structure (with blocking layers), the two identified sources after x-ray exposure, both of which result from the bulk negative space charge, are (1) the detrapping of the space charge and (2) the increase in the charge injection level at the x-ray receiving electrode due to the increased electric field [123], [21]. For a positively biased a-Se detector, the proposed detector design with shielding grids can nearly eliminate the first source of image lag due to the detrapping of the negative space charge, and thus, improve the temporal performance of the detector. Reduced image lag can especially benefit high frame rate imaging modalities such as real-time fluoroscopy [21], [22] and digital breast tomosynthesis [124], [125].

7.4 Conclusions

The presented work, for the first time, provides a comprehensive analysis of unipolar charge sensing photoconductors for direct detection radiation imaging in energy-integrating mode of operation. We proposed the use of electrostatic shield for erasing charge induction inside the interaction region and for preferential sensing of faster carriers inside the detection region. The insensitivity to slower carriers improves the charge collection efficiency because the induced charge only depends on the movement of long-ranged, faster carriers inside the detector. Thus, the detector yields higher x-ray sensitivity and detective quantum efficiency. Also, the insensitivity to both electron and hole trapping reduces signal spreading, and thus, the intrinsic resolution of the detector, characterized by the modulation transfer function, is improved. Finally, the insensitivity to the release of trapped slower carriers reduces image lag.

Chapter 8

Photocurrent Lag in Current-Mode Selenium

8.1 Introduction

The transport of charge carriers in most practical large-area direct conversion x-ray photoconductors, where the material structure is either amorphous or polycrystalline, is substantially different for holes and electrons due to trapping effects, which may result in schubweg-limited charge transport and reduce charge collection efficiency [97]. Memory artifacts are also seen in radiographs, which are caused by the spill-over of residual signal from previous exposures into subsequent image frames [18]. Such memory effects relax (i.e., diminish) with time and are attributed to interrupted carrier transport by traps in the photoconductor bulk and degrade the imagers temporal response. Memory effects are characterized by two important figures of merit: (1) persistent photocurrent lag, and (2) ghosting. Persistent photocurrent lag manifest itself as increased dark current after x-ray exposure. Ghosting is the change in detector sensitivity due to previous exposures, and as opposed to lag, it is measured during subsequent x-ray exposures [20], [21]. The spatial distribution of the radiation-induced trapped space charge has been previously examined using time-of-flight (TOF) transient photoconductivity measurements. Results indicate that for a positively biased amorphous selenium (a-Se) film a net negative trap space charge develops after x-ray exposure which increases the electric field at the radiation receiving electrode [122]. Also, a major contribution to the reduction in sensitivity is likely to come from the recombination of holes with the previously trapped electrons [126].

This chapter reexamines the question of whether the increased charge injection due to the increased electric field, or the detrapping of the bulk space charge is the dominant mechanism for the persistent photocurrent lag. We investigate the changes in samples dark current and lag for increased electric field. In chapter 4, we proposed a unipolar charge-sensing photoconductor using an intermediate electrostatic shield to provide insensitivity of the charge collection process to the movement, trapping, and release of the slower carriers. Here, we further investigate the level of reduction in image lag due to such insensitivity of the collector to the detrapping of the low-mobility space charge.

8.2 Coplanar Collector Geometry

Unipolar charge-sensing enables preferential sensing of the carrier type with a higher mobility-lifetime product $\mu\tau$ (e.g., holes in a-Se) and erases the collection of the other carrier type (e.g., electrons in a-Se). To build the unipolar devices and for the ease of fabrication, we chose a coplanar design where the pixel is divided into two interdigitated comb-like strip electrodes A and B [68], [69]. Figure 8.1a shows a coplanar n-type-intrinsic-p-type (n-i-p) structure with its theoretical field distribution, and Fig. 8.1b depicts the fabricated strip electrodes for the 1 mm^2 coplanar pixel (i.e., two interdigitated electrodes per pixel) where both the strips width and spacing is equal to 5 μm. Note that a conventional 1 mm ^{2} planar pixel (not shown) was also fabricated where the pixel electrode is only a single square metal plate. The intrinsic photoconductive layer deposited over the pixels are stabilized a-Se while the n-type and the p-type materials are doped a-Se and are used as blocking contact layers to limit charge injection by trapping holes and electrons, respectively. The total film thickness L evaporated on the electrodes is 200 μm. Figure 8.1c shows the weighting potential distribution for the fabricated coplanar pixel with strips A and B as collecting and non-collecting electrodes, respectively. According to the Schockley-Ramo theorem, the induced charge on an electrode Q_i due to single carrier motion is equal to the charge of the carrier q multiplied by its weighting potential V_W [72], [73]. Figure 8.1d illustrates the normalized charge induced on each strip electrode and also the subtraction of the two induced charges to obtain unipolar charge collection (i.e., hole-only collection for a positively biased a-Se). For the difference signal to yield accurate unipolar charge-sensing operation and for maintaining full sensitivity, we must ensure that 100% charge collection occurs on only one electrode. Thus, as shown in the inset field vector plot in Fig. 8.1d, the two strip electrodes are biased at different potentials (i.e., $V_B > V_A$) to direct all holes towards the collecting electrode A.

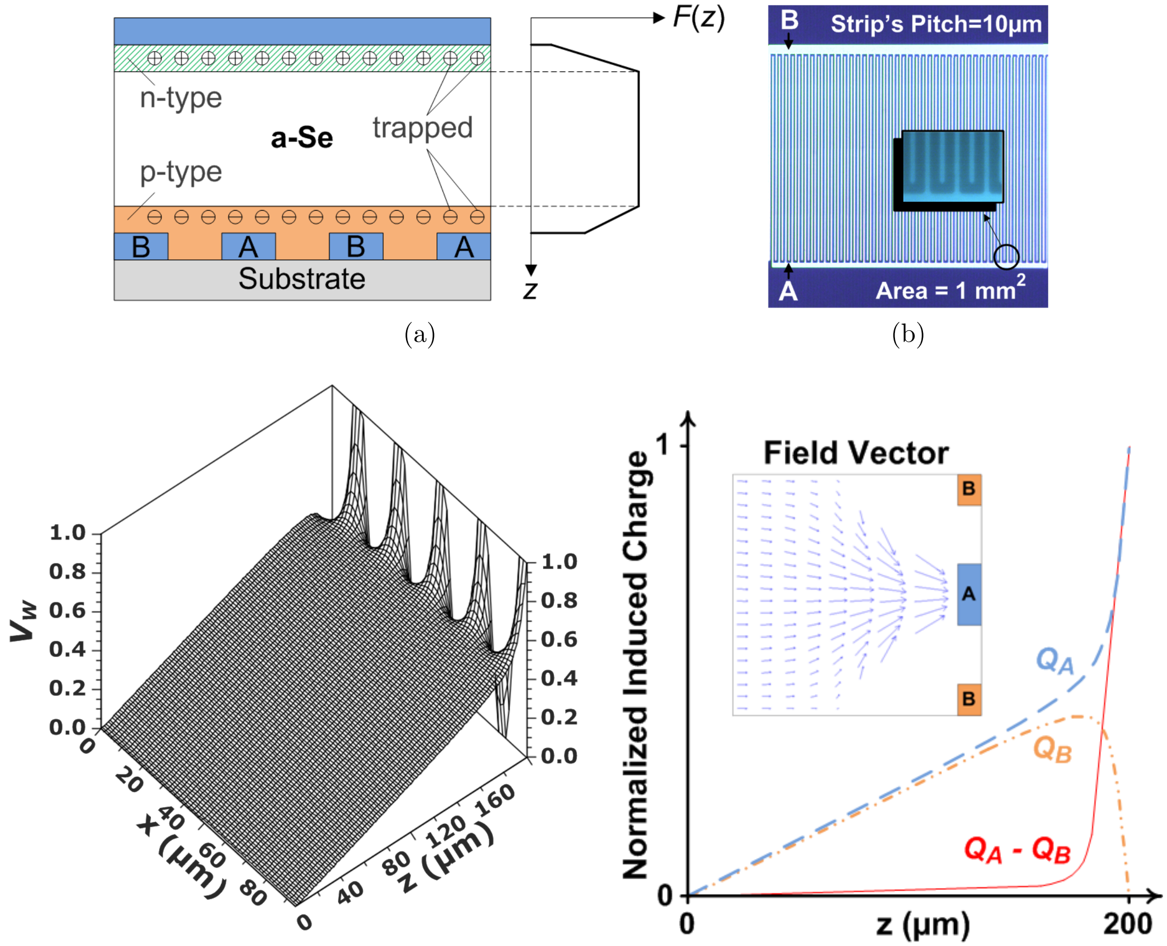

(a)

(b)

(c)

(d)

Figure 8.1: (a) Coplanar n-i-p detector structure with its theoretical field distribution $F(z)$. (b) Fabricated 1 mm^2 coplanar pixel. (c) Weighting potential distribution of the coplanar pixel. (d) Normalized induced charge for carrier drift across the detector. The inset shows the field vector inside a positively biased detector with V_B higher than V_A to collect all holes on electrode A.

8.3 Experimental Setup

The test sample shown in Fig. 8.1b was used to investigate the persistent photocurrent lag, which is measured as the percentage residual signal after the cessation of x-ray exposure. As shown in Fig. 8.2, generated x-ray pulses were absorbed in the photoconductor and the induced current at the collecting electrode A (I_A) was measured using a Keithley428 current amplifier. The analog output signal was captured on a Tektronix TDS360 digital scope. Also, the bias for the anode (V_+) and the non-collecting electrode B (V_B) was provided with a Bertan205B and an ORTEC556 high voltage power supplies, respectively. Note that because the potential at the inverting terminal of the current amplifier was fixed at virtual ground, the x-ray induced photocurrent at the collecting and non-collecting electrodes were measured sequentially, and not concurrently, under identical x-ray exposure and detector field distribution conditions. The signal at the non-collecting electrode (I_B) was measured by connecting the current amplifier to electrode B and applying a negative bias to electrode A. Furthermore, due to the small ratio of strip pitch to detector thickness (i.e., 10/200), the distributed field inside the photoconductor is uniform and equal to $(V_+ - 0.5(V_B - V_A))/L$. Thus, V_+ must be adjusted according to the electrodes bias to yield the same field for photocurrent measurements from both the collecting and the non-collecting strip electrodes.

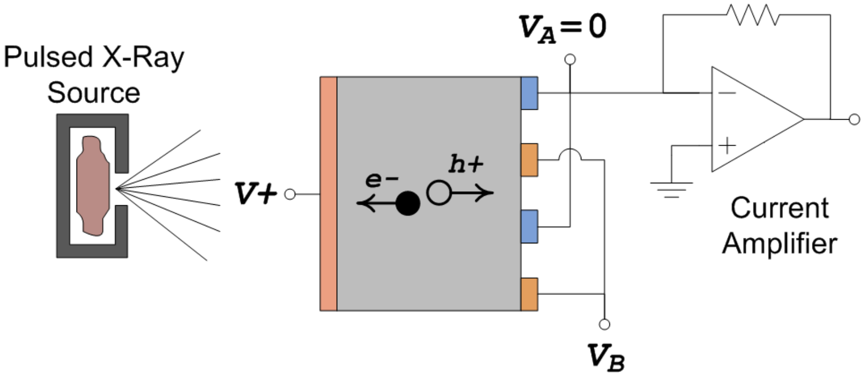

Figure 8.2: Schematic of the experimental setup for measuring the x-ray induced photocurrent.

8.4 Experimental Results and Discussions

Time-of-flight transient photoconductivity measurements have showed that a net negative space charge is created inside a-Se after x-ray exposure because the schubweg for electrons is significantly smaller than that of holes and also the trap levels for electrons are deeper in the band gap with longer release times [122]. Although no conclusive evidence has been presented to show the dominant mechanism for lag in a-Se, the two identified sources, both of which result from the bulk negative space charge, are (1) the increase in the charge injection level at the x-ray receiving electrode due to the increased electric field, and (2) the detrapping of the space charge [123]. Figure 8.3 shows the measured dark current transients of a planar n-i-p a-Se photoconductor due to contact charge injection after the applied step electric fields. Dark current results, even at the onset of a 100% step increase in field from 5 V/μm to 10 V/μm, are substantially lower than the measured lag transient of Fig. 8.4a for a planar 1 mm^2 pixel at 5 V/μm. Thus, the transient increase in the injected current from the metal contacts due to a sudden increase in electric field cannot

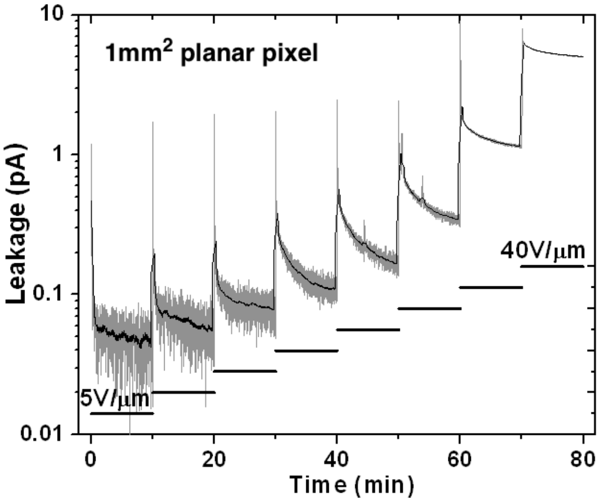

Figure 8.3: Measured dark current transients of a planar n-i-p a-Se photoconductor.

justify the measured persistent photocurrent lag, and as will be further evident below, lag must originate from the detrapping of the space charge.

Figure 8.4a also shows the measured x-ray signal from the 1 mm^2 coplanar detector configuration at 5 V/μm while exposed to a 16 mR, 80 kV x-ray beam. The cathode pixel for the planar detector and the strip electrodes A and B for the coplanar detector were all grounded. With this strip electrode biasing, the coplanar detector does not provide unipolar charge sensing because both electrodes are collecting x-ray induced photocurrent equally, as shown from lower x-ray sensitivity of I_A compared to I. Nevertheless, as shown from the spatial distribution of Q_A in Fig. 8.1d, the collected charge on strip electrode A is 50% less sensitive to the detrapping of the electrons and the normalized inset in Fig. 8.4a shows reduced lag compared to that of the planar detector. Measured lag currents are 1 nA (5.5% lag) and 0.16 nA (2.7% lag) shortly after exposure at $t = 175$ ms for the planar and the coplanar detectors, respectively.

Figure 8.4b shows the X-ray induced photocurrents I_A and I_B for the coplanar detector while exposed to a 340 mR, 80 kV x-ray beam. The applied electric field was only 0.25 V/μm to enhance trapping due to schubweg-limited electron transport and the 80 kV radiography spectrum was chosen to create a uniform x-ray absorption profile across the detector thickness. Also, V_B was biased at a higher potential than V_A to maintain full sensitivity by complete charge collection at electrode A. Thus, the measured signal on electrode B is only the photocurrent lag that is induced by the drifting detrapped electrons. Finally, for unipolar charge-sensing operation, I_B was subtracted from I_A and the results are illustrated in Fig. 8.4c. We observe further reduction in lag due to complete insensitivity of the charge collection process to the detrapping of electrons. The remaining lag is due to the detrapping of holes which are fully collected on electrode A.

8.5 Conclusions

The dominant source for the measured persistent photocurrent lag in n-i-p a-Se photoconductors is the detrapping of the space charge. For such detectors, unipolar charge-sensing can be utilized to provide insensitivity to the drifting slower carriers, and thus, reduce lag. Given that image lag is the main impediment for fast temporal performance, the proposed unipolar design can improve the performance of selenium-based imagers in applications such as x-ray tomosynthesis and real-time fluoroscopy. Moreover, such temporal performance improvements might be more prominent for emerging high gain detectors such as poly-crystalline mercuric iodide (HgI_2) and lead-oxide (PbO), which have not yet entered commercial use mainly due to longer lag decay time compared to a-Se.

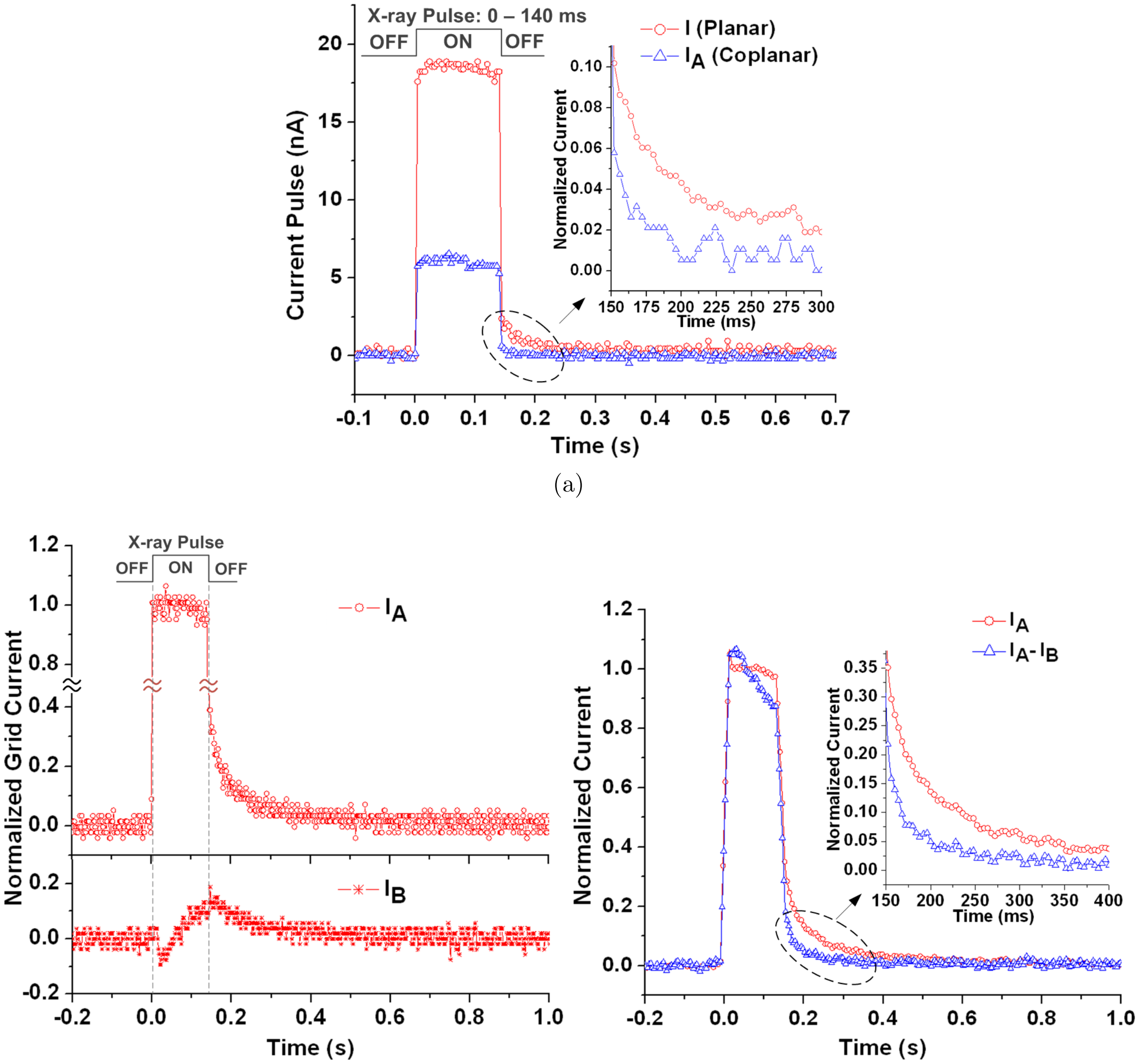

(a)

(b)

(c)

Figure 8.4: (a) Pulsed x-ray signal from a 1 mm^2 planar and coplanar detector configurations at 5 V/μm while exposed to a 16 mR, 80 kV x-ray beam. (b) X-ray induced photocurrents from the coplanar detector structure at 0.25 V/μm while exposed to a 340 mR, 80 kV x-ray beam. (c) Unipolar x-ray signal with reduced lag.

Chapter 9

Conclusions and Contributions

9.1 Conclusions

We showed that the limitations with the existing direct conversion flat panel detectors (FPDs) for digital radiography are poor dose efficiency (due to poor noise rejection and non-optimal energy weighting) and the presence of memory artifacts and anatomical noise in the radiographs. The root of these limitations is the operation of the radiation detector in *current mode* with energy-integrating readout which is susceptible to poor noise rejection and incorrect energy weighting. We showed that by switching the operation to *pulse mode* for individual photon counting, we can gain higher dose efficiency through efficient noise rejection and suboptimal energy weighting. Photon counting systems are also not susceptible to memory artifacts. However, the requirement to operate in pulse-mode is currently not met by most photoconductors used today for direct conversion digital radiography systems.

The oldest type of radiation detectors that operate in pulse-mode are cylindrical proportional counters which are based on detecting the direct ionization by the travelling radiation in a gaseous medium. In 1968, Charpak's multiwire proportional chamber revolutionized the field of radiation detection and showed spatial and temporal resolution which were orders of magnitude better than those of single-wire cylindrical structures. This technology also enabled, for the first time, x-ray and neutron imaging over large area. In most applications, however, the use of a solid detection medium is preferable because solid densities are about three orders-of-magnitude greater than gas, and thus, they can yield much smaller detector dimensions with unsurpassed spatial and temporal resolution. The problem is that amorphous solids, which are easier and less expensive to develop over large area than single crystalline solids, have been ruled out as a viable radiation detection medium because of low carrier mobilities, depth-dependent signal noise, and transit-time-limited photoresponse.

We investigated the deteriorating effect of poor carrier transport on the temporal resolution and the counting rate of an amorphous selenium (a-Se) spectrometer. To circumvent the problem of poor carrier transport, we proposed establishing a strong near field effect for unipolar charge sensing using an electrostatic shield within the detector structure. For the new device structure, we introduced the concept of time-differential photoresponse where the included current on the collector due to an impulse excitation is no longer transit-time limited and is proportional to the time-derivative of the photocurrent in a conventional planar device for the same excitation. Theoretical results showed that the temporal resolution (and consequently, the photon count-rate) can be improved substantially and one can reach the intrinsic physical limit, which is determined by the spatial dispersion of the photoinduced carrier packet.

For the first time, we implemented an electrostatic shield inside a solid material using the proposed lithography-based microstrip solid state detector (MSSD). The device consisted of an evenly spaced insulating pillars over the collector where their top side was coated with a conductor to form the electrostatically shielding microstrips. To ensure blocking contacts for limiting the excess charge injection, the microstrips were surrounded by another thin insulating layer. After the fabrication of the blocking microstrips on the collector, a-Se film was evaporated over the structure as the photoconductive material, and finally, a semi-transparent layer was sputtered on top to provide the drift electrode.

For device characterization, we considered three experiments. First, a sheet of excess carriers was photoinduced close to the drift electrode with an impulse-like optical laser excitation for time-of-flight (TOF) transient photoconductivity measurement. In the case of non-dispersive Markoffian transport in a-Se at room-temperature, the propagating photoinduced carrier packet experiences broadening which is described by Gaussian statistics. For the first time, we showed unipolar Gaussian TOF transients using the new MSSD structure, instead of a rectangular TOF with a Gaussian-integral at the tail which is a typical response for a conventional planar device. The Gaussian response centred at the hole transit-time verified the time-differential property of the electrostatic shield and the practicality of the dispersion-limited photoresponse. Second, Gaussian carrier clouds were generated uniformly across the bulk with an impulse-like high energy x-ray beam. The measured time-resolved transients showed a linear decay (i.e., triangular response) for the conventional planar device and a nearly constant rectangular response for the new unipolar MSSD, proving once again the time-differential property of the shield to impulse excitations. Finally, we used a single-photon excitation to probe detector's temporal response in pulse mode for photon counting. For the MSSD, we obtained a depth-independent signal for photon absorption across the bulk and a reduction in signal risetime by a factor of 350, comparing performance limiting factors being hole-dispersion for the MSSD and electron-transit-time for the conventional planar device.

Lastly, we showed incremental performance improvement of unipolar charge sensing in energy-integrating current mode detectors. The insensitivity to slower carriers improves the charge collection efficiency because the induced charge only depends on the movement of long-ranged, faster carriers inside the detector. Thus, the detector yields higher x-ray sensitivity and detective quantum efficiency. Also, the insensitivity to both electron and hole trapping reduces signal spreading, and thus, the intrinsic resolution of the detector, characterized by the modulation transfer function, is improved. Finally, the insensitivity to the release of trapped slower carriers reduces image lag.

9.2 Future Work

Another non-ohmic effect in disordered solids, aside from the Pool-Frenkel-type conduction, may occur in the presence of a strong field with the transport mechanism shifted from localized states into extended states where the mobility can be 100 to 1000 times higher. Such hot carriers in extended states (with mobilities near the mobility edge) can gain energy faster than they lose it to phonons, and thus, avalanche due to impact ionization is possible [127], [43]. Continuous and stable avalanche multiplication has been shown in a-Se, a feature that enabled the development of an optical camera with more sensitivity than the human eye (i.e., 11 lx at aperture F8, or 100 times more sensitive than a CCD camera) [92]. For high-energy penetrating radiation, the challenge is that avalanche-mode selenium cannot be the bulk medium because (1) avalanche layers cannot be very thick ($< 25\mu$m) and (2) a uniform avalanche field in the bulk causes depth-dependent gain variations (or ballistic deficit). In the MSSD shown in Fig. 6.1a, the low-field interaction region can be made as thick as necessary to stop high-energy radiation, and the high-field detection region can be optimized for avalanche multiplication.

The combination of the time-differential and avalanche-multiplication properties of the microstrip electrostatic shield can yield another great leap forward in the field of radiation detectors with applications ranging from high-energy [128], nuclear [129], and astro- physics [130], to industrial and medical diagnostics [3], and crystallography [131].

9.3 My Contribution to Research

Perhaps my most significant contribution would be to have proved the time-differential photoresponse in disordered solids, and thus, the transition from the conventional transit-time-limited performance to the intrinsic physical limit set by spatial dispersion. Although I showed the experimental results for evaporated amorphous selenium, the idea of time-differential response is applicable to any medium and in its simplest form it states that:

> *If we have a near field effect in the immediate vicinity of a collector in any medium and a single drifting excess carrier is confined within this medium, the total kinetic energy of the carrier during its transit is transferred to the collector only at the onset of neutralization, and thus, photoresponse is an impulse.*

Submitted manuscript:

− A.H. Goldan, O. Tousignant, J.A. Rowlands, and K.S. Karim "Solid-state Charpak Detector with Unipolar Time-Differential Pulse Response," Phys. Rev. Lett. (under review).

Journal Publications:

− A.H. Goldan, K.S. Karim, O. Tousignant, and L. Laperriere "Reduced photocurrent lag using unipolar solid-state photoconductors: application to stabilized n-i-p amorphous selenium," Appl. Phys. Lett. 96, 053507 (2010).

− A.H. Goldan, K.S. Karim, and John A. Rowlands, Single Photon Counter for Digital X-ray Mammography Tomosynthesis, Journal of Vacuum Science and Technology A 24(3), 854-859 (2006).

Conference Publications:

− A.H. Goldan, K. Wang, F. Chen, et al., "Amorphous selenium lateral Frisch photodetector and photomultiplier for high performance medical x-ray and gamma-ray imaging applications," Proceedings of SPIE Vol. 7622, 76223R (2010).

− N. Allec, A.H. Goldan, K. Wang, et al., "Amorphous silicon p-i-n photodetector with Frisch grid for high-speed medical imaging," Proceedings of SPIE Vol. 7622, 76223X (2010).

− A.H. Goldan and K.S. Karim, "Frisch grid for large-area direct detection medical x-ray imaging," RSNA 2009, Accepted for Oral Presentation.

− A.H. Goldan, Y. Fang, K.S. Karim, et al., "Amorphous selenium detector utilizing a Frisch grid for photon-counting imaging applications," Proceedings of SPIE Vol. 7258, 725816 (2009).

− A.H. Goldan, B. Hadji, K.S. Karim, et al., “A counting and integrating pixel readout chip for amorphous selenium direct radiation detectors for medical imaging applications,” Proceedings of SPIE Vol. 7258, 72583K (2009).

− A.H. Goldan, K.S. Karim, “Unipolar charge sensing using Frisch grid technique for amorphous selenium radiation detectors,” Proceedings of SPIE Vol. 7079, 70790P (2008).

− A.H. Goldan, K.S. Karim, A. Reznik, et al., “Photon counting readout pixel array in 0.18-m CMOS technology for on-line gamma-ray imaging of 103-palladium seeds for permanent breast seed implant (PBSI) brachytherapy,” Proceedings of SPIE Vol. 6913, 69130S (2008).

− A.H. Goldan, L. Ng, J.A. Rowlands, et al., “Photon counting pixel architecture for x-ray and gamma-ray imaging applications,” Proceedings of SPIE Vol. 6510, 65103V (2007).

APPENDICES

Appendix A

SEM Sample Preparation

Because the substrate for our fabrication is corning glass and the deposited films are non-crystalline, our devices cannot be cleaved to obtain a smooth and sharp cross-section (or edge) for single-electron microscopy (SEM). Thus, one must dice the substrate along the desired feature instead of cleaving. However, due to the much larger blade thickness of the dicing machine (i.e., 50-100 μm) compared to the thickness of the deposited films (which can be in the range of submicron), features are damaged and images are blurred, as shown in the SEM of Fig. A.1.

The solution is to polish the diced edges using the process explained in Table A.1. Figure A.2 shows photographs of the diced sample, the casts prepared, and the Struers polishing machine. The SEM of a polished edge, with the same structure as Fig. A.1, is shown in Fig. A.3. Note that all features, compositions, and layer thicknesses are clearly identified. More SEM images of polished samples are shown in Fig. A.4.

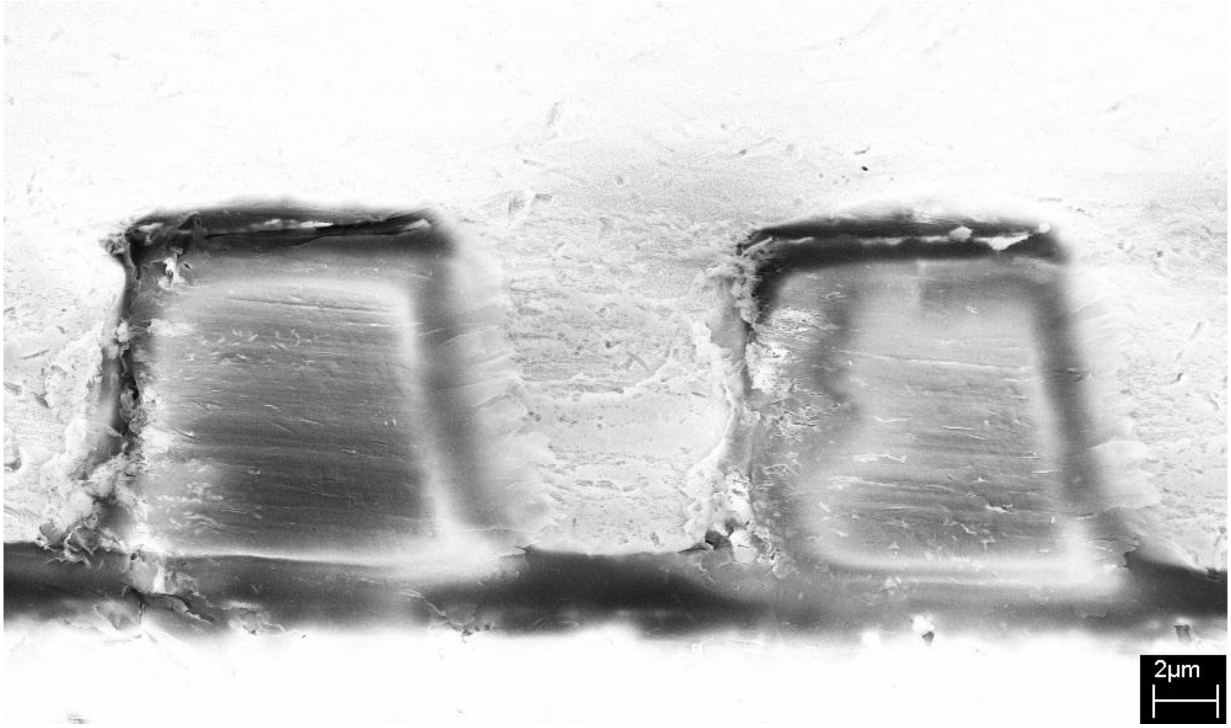

Figure A.1: SEM of a diced cross-section before polishing. Image is blurred and features are damaged.

Table A.1: Sample preparation and polishing process.

Steps	Process
p1)	Substrate was diced orthogonal to the direction of the microstrips, as shown in Fig. A.2a.
p2)	Diced edges were placed facing down inside casting cups using clips, as shown in Fig. A.2b.
p3)	Cups were filled with a transparent epoxy which was capable of curing at room-temperature.
p4)	Epoxy was cured after 24 hr and the solidified casts were removed from the cups, as shown in Fig. A.2c.
p5)	Casts were initially polished with a rough abrasive, starting from 600 grit and gradually going up to 1200 grit with much finer grains. Polishing papers were installed on the rotating disc of the Struers machine shown in Fig. A.2d and the casts were made into contact with the rotating paper using the cast holder.
p6)	After polishing with the 1200 grit paper, a polishing cloth was installed on the disc and was wetted with a special lubricant. The composition of the lubricant used, given that our polishing involves a composite material, was 50% silica and 50% methanol. Casts were further polished with the cloth until the surface smoothness of the diced edges reached a nanometer level.
p7)	The polished surface was sputtered with gold.

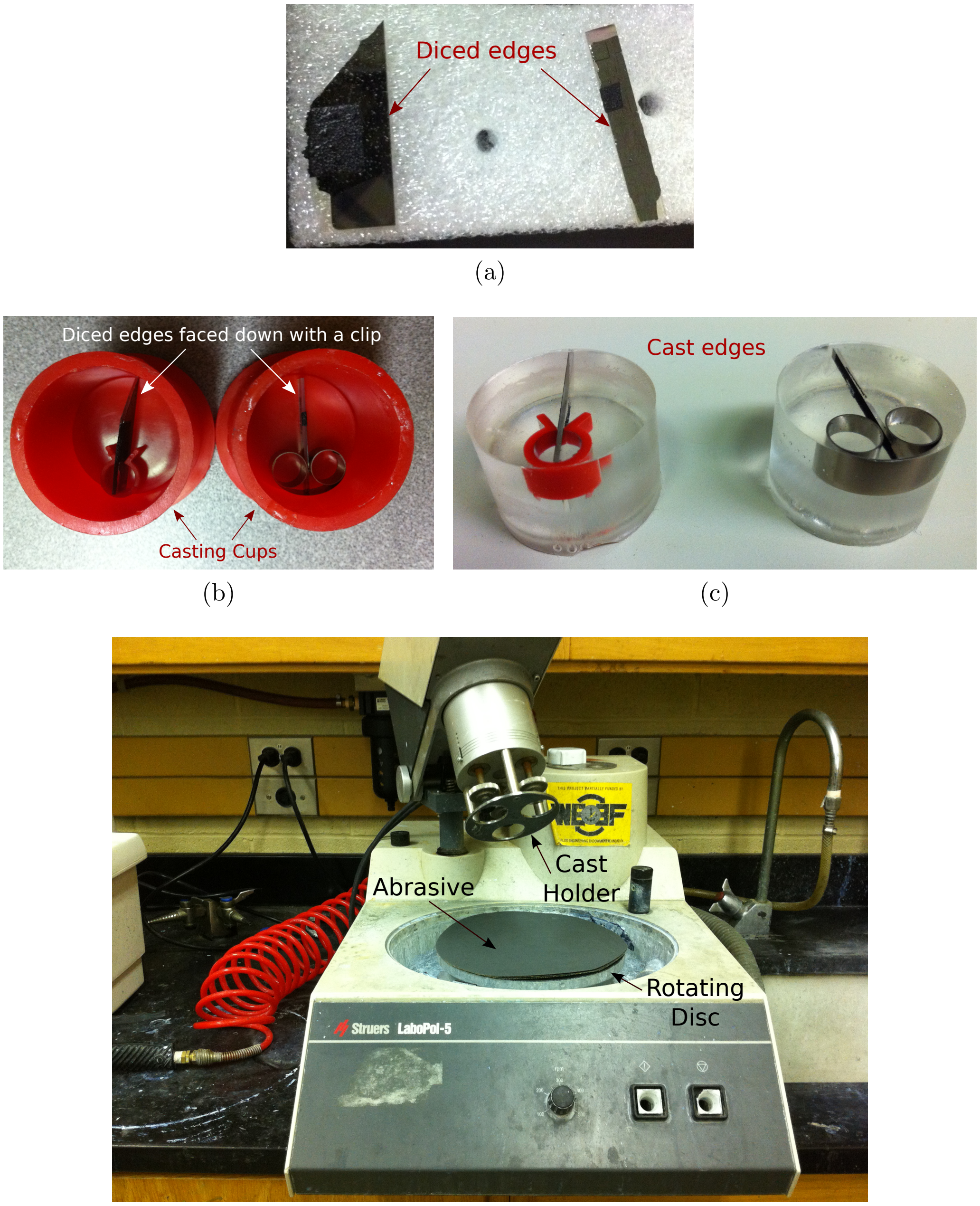

(a)

(b)

(c)

(d)

Figure A.2: (a) Diced edges where the cut was orthogonal to the microstrips for the fabricated device of Fig. 5.6. (b) Diced edges placed in casting cups with clips. (c) Cast edges with room-temperature curing transparent epoxy. (d) Struers machine used for polishing the cast edges.

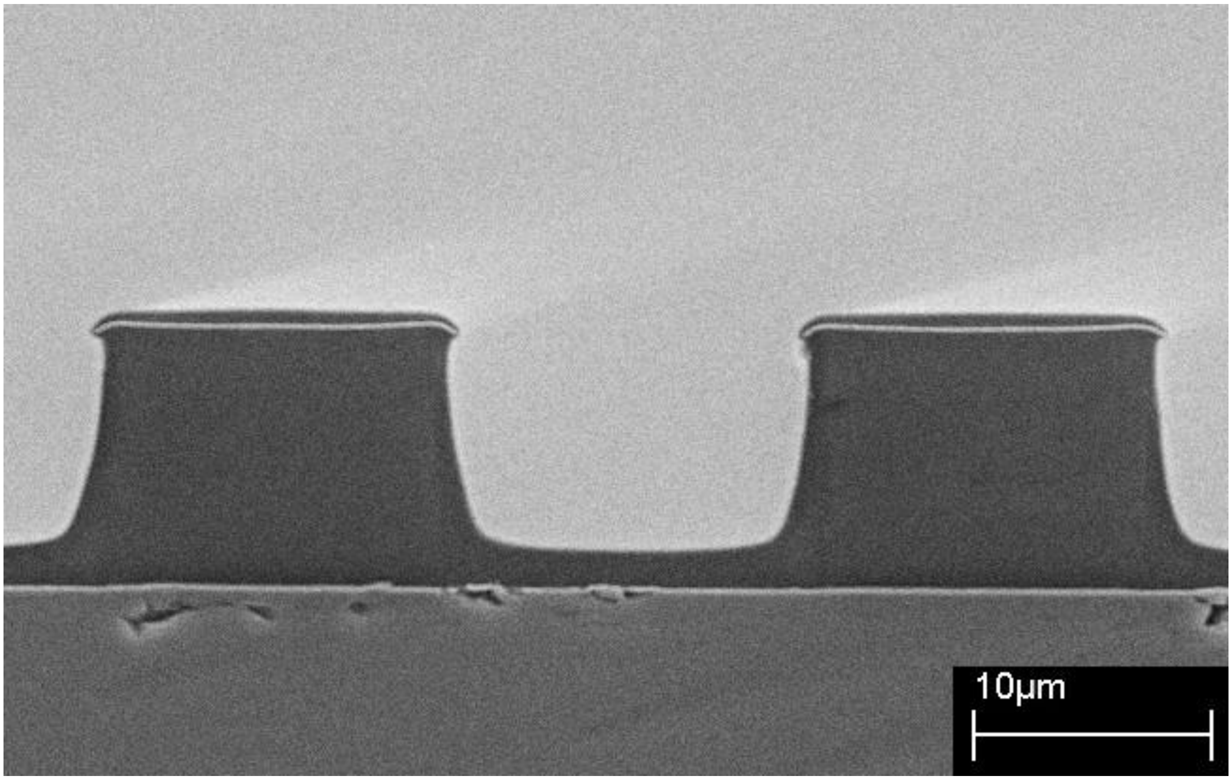

Figure A.3: SEM of a polished cross-section. All features, compositions, and layer thicknesses are clearly identified.

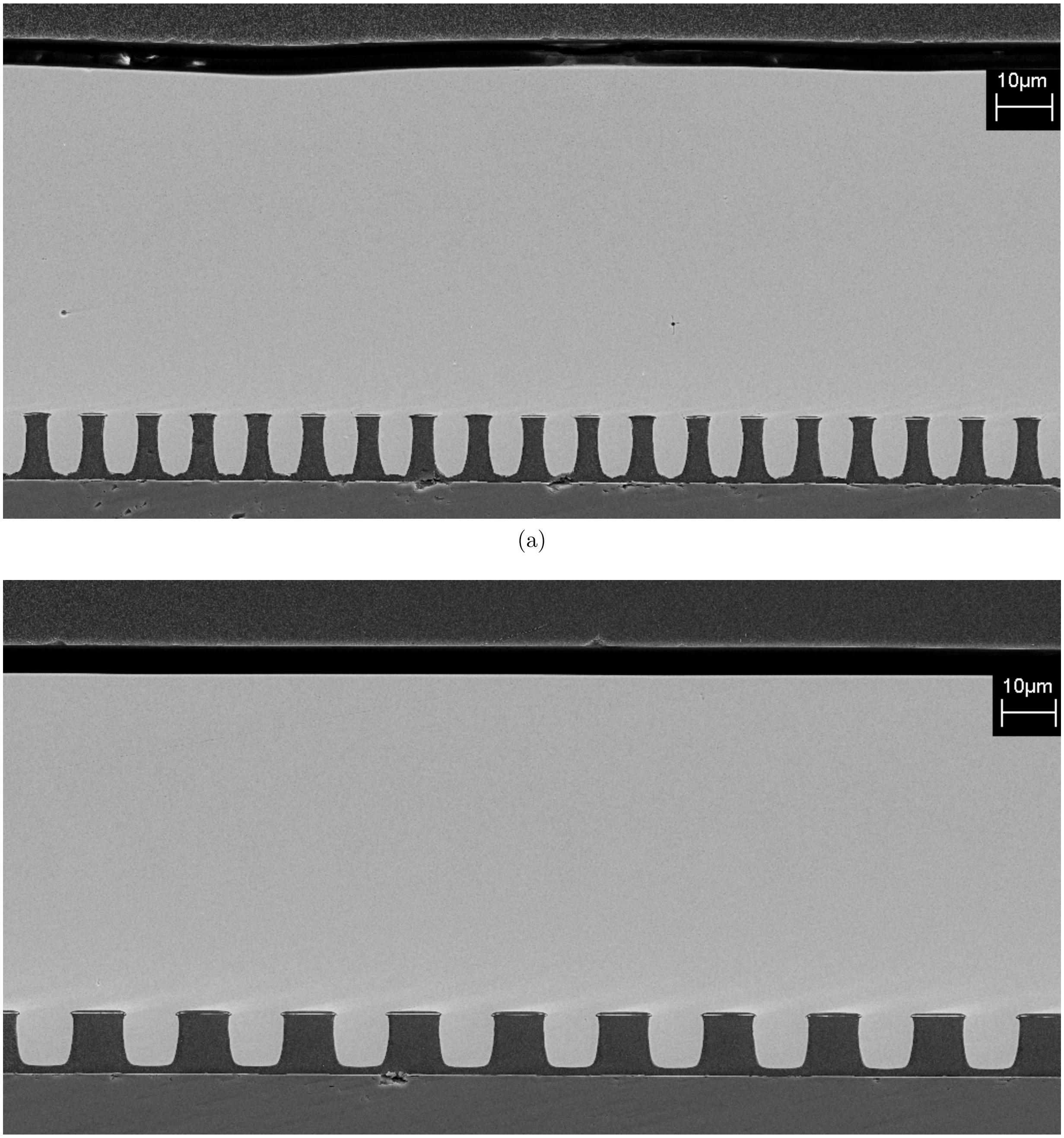

(a)

(b)

Figure A.4: SEMs of samples with microstrip pitch of (a) 10 μm, (b) 20 μm.

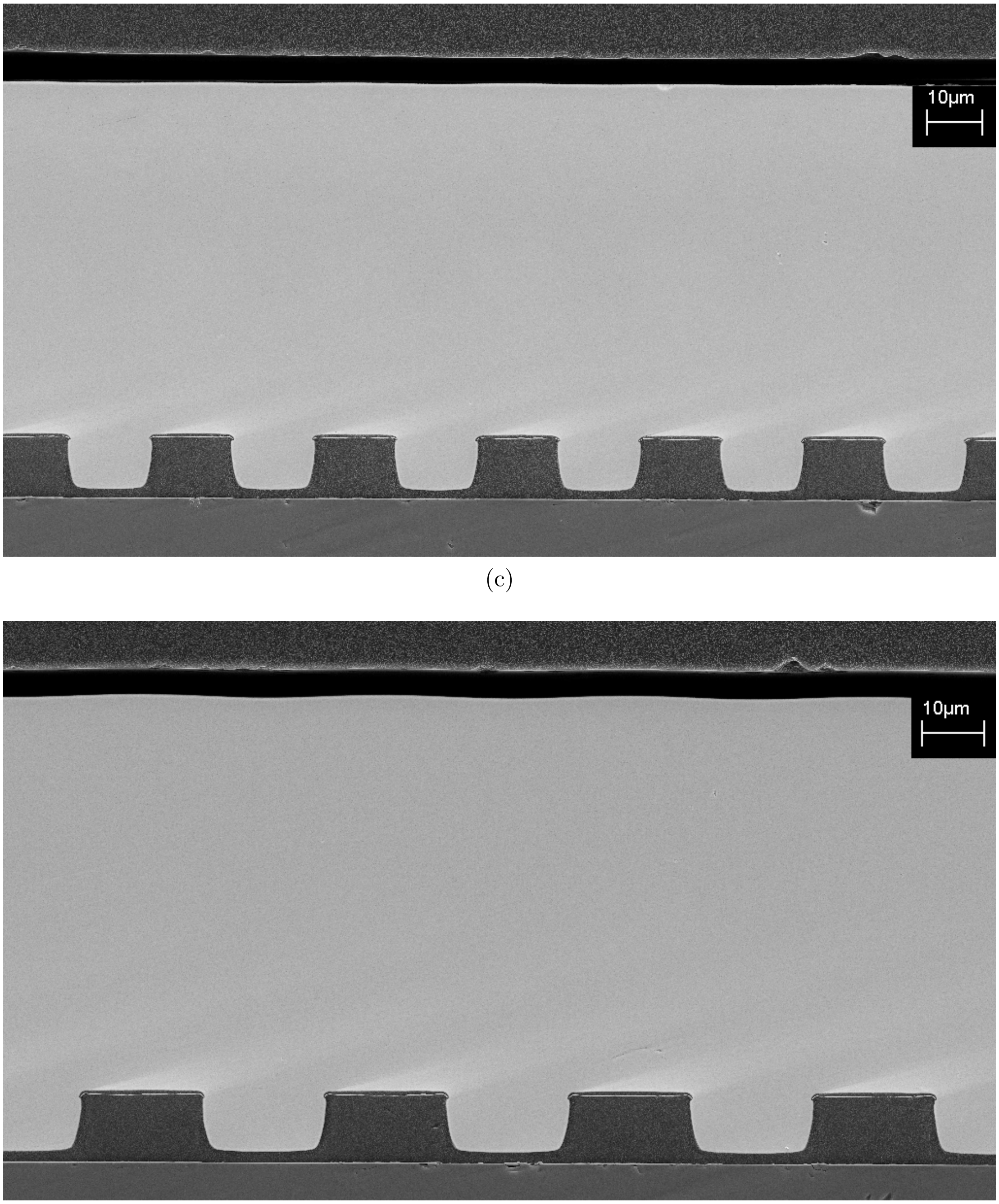

(c)

(d)

Figure A.4: SEMs of samples with microstrip pitch of (c) 30 μm, and (d) 40 μm.

Appendix B

Emulating Photolithography with Sentaurus Structure Editor

```
;=== Defining the emulation domain
(define Xmax -75) ; Width
(define Ymax 75)  ; Length
(sdepe:define-pe-domain (list 0.0 0.0 Xmax Ymax))
;=== Defining the substrate (glass-insulator)
(define SubThi 5.0)
(define SUB (sdepe:add-substrate
"material" "Anyinsulator" "thickness" SubThi))
(sde:add-material SUB "Anyinsulator" "R.GlassSubstrate")
;=== Depositing the pixel electrode (Aluminum)
(define PixThi 0.4)
(define PIX (sdepe:depo
"material" "Aluminum" "thickness" PixThi "type" "iso"))
(sde:add-material PIX "Aluminum" "R.PixelElectrode")
;=== Depositing the Frisch insulating pillar (Polyimide)
(define PillarThi 7.5)
```

```
(define PILLAR (sdepe:depo
"material" "InsulatorX" "thickness" PillarThi "type" "iso"))
(sde:add-material PILLAR "InsulatorX" "R.FrischPillar")
;=== Depositing the Frisch Electrode (Chromium)
(define FrischThi 0.4)
(define FRISCH (sdepe:depo
"material" "Chromium" "thickness" FrischThi "type" "iso"))
(sde:add-material FRISCH "Chromium" "R.FrischElectrode")
;=== Generating the microstrip mask
(define fm1Xb 0)
(define fm1Yb 0)
(define fm1Xe -75)
(define fm1Ye 15)
(define fm2Xb 0)
(define fm2Yb 30)
(define fm2Xe -75)
(define fm2Ye 45)
(define fm3Xb 0)
(define fm3Yb 60)
(define fm3Xe -75)
(define fm3Ye 75)
(sdepe:generate-mask "mFRISCH"
(list (list fm1Xb fm1Yb fm1Xe fm1Ye)
(list fm2Xb fm2Yb fm2Xe fm2Ye)
(list fm3Xb fm3Yb fm3Xe fm3Ye)))
(define frThi 3)
(sdepe:pattern "mask" "mFRISCH" "polarity" "light"
"type" "aniso" "material" "Resist" "thickness" frThi)
;=== Etch the Frisch Electrode (Chromium)
(sdepe:etch-material "material" "Chromium" "depth" FrischThi)
;=== Strip the Frisch resist
(sdepe:strip-material "Resist")
;=== Etch the Frisch Channel (Polyimide)
(sdepe:etch-material "material" "InsulatorX" "depth" PillarThi
"type" "iso" "algorithm" "lopx" "taper-angle" 8)
;=== Depositing the Frisch shield (Polyimide)
(define ShieldThi 1)
(define SHIELD (sdepe:depo "material" "InsulatorX" "thickness" ShieldThi
```

```
"type" "iso" "vexity" "all" "radius" 0))
(sde:add-material SHIELD "InsulatorX" "R.FrischShield")
;=== Generating the blocking layer mask
(define fm1Xb2 0)
(define fm1Yb2 0)
(define fm1Xe2 -75)
(define fm1Ye2 16)
(define fm2Xb2 0)
(define fm2Yb2 29)
(define fm2Xe2 -75)
(define fm2Ye2 46)
(define fm3Xb2 0)
(define fm3Yb2 59)
(define fm3Xe2 -75)
(define fm3Ye2 75)
(sdepe:generate-mask "mFRISCH2" (list
(list fm1Xb2 fm1Yb2 fm1Xe2 fm1Ye2)
(list fm2Xb2 fm2Yb2 fm2Xe2 fm2Ye2)
(list fm3Xb2 fm3Yb2 fm3Xe2 fm3Ye2)))
(define frThi 3)
(sdepe:pattern "mask" "mFRISCH2" "polarity" "light"
"type" "aniso" "material" "Resist" "thickness" frThi)
;=== Etch the Collector Insulator
(sdepe:etch-material "material" "InsulatorX" "depth" 1
"type" "aniso" "overetch" 0  "radius" 1)
;=== Strip the Frisch resist
(sdepe:strip-material "Resist")
(sdegeo:set-default-boolean "BAB")
;=== Create the photoconductive layer (Selenium)
(sdegeo:create-cuboid
(position 0 0 5.4) (position -75 75 30) "CdTe" "R.Detector")
;=== Depositing the High-Voltage Electrode (Gold)
(define hvThi 0.4)
(define HV (sdepe:depo "material" "Gold" "thickness" hvThi
"type" "iso" "vexity" "all" ))
(sde:add-material HV "Gold" "R.HighVoltageElectrode")
;=== Saving the Model
(sde:save-model "Micro_Strip_Solid_State_Detector")
```

References

[1] Jerrold T. Bushberg, J. Anthony Seibert, Edwin M. Leidholdt Jr., and John M. Boone. *The Essential Physics of Medical Imaging (2nd Edition)*. Lippincott Williams & Wilkins, 2.00 edition, December 2001. xii, 10, 11, 55

[2] W. Zhao and J. A. Rowlands. Xray imaging using amorphous selenium: Feasibility of a flat panel selfscanned detector for digital radiology. *Medical Physics*, 22(10):1595–1604, 1995. x, 10, 11

[3] M. J. Yaffe and J. A. Rowlands. X-ray detectors for digital radiography. *Physics in Medicine and Biology*, 42(1):1–39, January 1997. 12, 140

[4] E. Samei and M. J. Flynn. An experimental comparison of detector performance for direct and indirect digital radiography systems. *Medical Physics*, 30(4):608–622, 2003. 12

[5] S. O. Kasap. Photoreceptors: the selenium alloys. pages 329–372. Marcel Dekker, 1991. 12

[6] M. Lundqvist, B. Cederstrom, V. Chmill, M. Danielsson, and B. Hasegawa. Evaluation of a photon-counting X-ray imaging system. *Nuclear Science, IEEE Transactions on*, 48(4):1530–1536, August 2001. xii, 13, 14, 15

[7] O. Tousignant, Y. Demers, L. Laperriere, and S. Marcovici. A-Se Flat Panel Detectors for Medical Applications. *Sensors Applications Symposium, 2007. SAS '07. IEEE*, pages 1–5, February 2007. 13

[8] J. A. Segui and W. Zhao. Amorphous selenium flat panel detectors for digital mammography: Validation of a NPWE model observer with CDMAM observer performance experiments. *Medical Physics*, 33(10):3711–3722, 2006. 13

[9] Mats Danielsson, Hans Bornefalk, Bjoern Cederstroem, Valery Chmill, Bruce H. Hasegawa, Mats Lundqvist, David R. Nygren, and Tamas Tabar. Dose-efficient system for digital mammography. In *Proceedings of SPIE*, volume 3977. The International Society for Optical Engineering., April 2000. x, 15

[10] M.M Tesic, M Fisher Piccaro, and B Munier. Full field digital mammography scanner. *European Journal of Radiology*, 31(1):2–17, July 1999. 15

[11] Paul S. Rezentes, Adelaide de Almeida, and Gary T. Barnes. Mammography Grid Performance. *Radiology*, 210(1):227–232, January 1999. 15

[12] Robert K. Swank. Absorption and noise in xray phosphors. *Journal of Applied Physics*, 44(9):4199–4203, September 1973. 16

[13] M. Maolinbay, Y. El-Mohri, L. E. Antonuk, K. W. Jee, S. Nassif, X. Rong, and Q. Zhao. Additive noise properties of active matrix flat-panel imagers. *Medical Physics*, 27(8):1841–1854, 2000. 16

[14] A. H. Goldan, K. S. Karim, A. Reznik, C. B. Caldwell, and J. A. Rowlands. Photon counting readout pixel array in 0.18-μm CMOS technology for on-line gamma-ray imaging of 103palladium seeds for permanent breast seed implant (PBSI) brachytherapy. In *Proceedings of SPIE*, volume 6913. The International Society for Optical Engineering., March 2008. 16

[15] R. N. Cahn, D. Nygren, B. Cederström, M. Danielsson, A. Hall, and M. Lundqvist. Detective quantum efficiency dependence on x-ray energy weighting in mammography. *Medical Physics*, 26(12):2680–2683, 1998. x, 17, 18

[16] S. O. Kasap and J. A. Rowlands. Review X-ray photoconductors and stabilized a-Se for direct conversion digital flat-panel X-ray image-detectors. *Journal of Materials Science: Materials in Electronics*, 11(3):179–198, April 2000. 18

[17] A. H. Goldan, Y. Fang, K. S. Karim, O. Tousignant, H. Mani, and L. Laperrière. Amorphous selenium detector utilizing a Frisch grid for photon-counting imaging applications. In *Proceedings of SPIE*, volume 7258. The International Society for Optical Engineering., February 2009. 18, 59

[18] H G Chotas, C E Floyd, and C E Ravin. Memory artifact related to selenium-based digital radiography systems. *Radiology*, 203(3):881–883, June 1997. 19, 127

[19] Wei Zhao, Giovanni DeCrescenzo, and John A. Rowlands. Investigation of lag and ghosting in amorphous selenium flat-panel x-ray detectors. In *Proceedings of SPIE*, volume 4682, pages 9–20. The International Society for Optical Engineering., May 2002. 19, 124

[20] Brad T. Polischuk, Ziad Shukri, Anne Legros, and Henri Rougeot. Selenium direct-converter structure for static and dynamic x-ray detection in medical imaging applications. In *Proceedings of SPIE*, volume 3336. The International Society for Optical Engineering., July 1998. 19, 128

[21] Olivier Tousignant, Yves Demers, Luc Laperriere, Habib Mani, Philippe Gauthier, and Jonathan Leboeuf. Spatial and temporal image characteristics of a real-time large area a-Se x-ray detector. In *Proceedings of SPIE*, volume 5745. The International Society for Optical Engineering., April 2005. 19, 125, 128

[22] George Zentai, Larry D. Partain, Raisa Pavlyuchkova, Cesar Proano, Gary F. Virshup, L. Melekhov, A. Zuck, Barry N. Breen, O. Dagan, A. Vilensky, Michael Schieber, Haim Gilboa, Paul Bennet, Kanai S. Shah, Yuriy N. Dmitriyev, Jerry A. Thomas, Martin J. Yaffe, and David M. Hunter. Mercuric iodide and lead iodide x-ray detectors for radiographic and fluoroscopic medical imaging. In *Proceedings of SPIE*, volume 5030. The International Society for Optical Engineering., June 2003. 19, 125

[23] L T Niklason, B T Christian, L E Niklason, D B Kopans, D E Castleberry, B H Opsahl-Ong, C E Landberg, P J Slanetz, A A Giardino, R Moore, D Albagli, M C

DeJule, P F Fitzgerald, D F Fobare, B W Giambattista, R F Kwasnick, J Liu, S J Lubowski, G E Possin, J F Richotte, C Y Wei, and R F Wirth. Digital tomosynthesis in breast imaging. *Radiology*, 205(2):399–406, November 1997. 19, 20

[24] James T Dobbins and Devon J Godfrey. Digital x-ray tomosynthesis: current state of the art and clinical potential. *Physics in Medicine and Biology*, 48(19):R65–R106, October 2003. 20

[25] A Brief History of Glass. 22

[26] Sir Nevill Mott. Electrons in glass. *Reviews of Modern Physics*, 50(2):203–208, 1978. xiii, 23, 32, 36, 38, 40

[27] B. T. Kolomiets. Vitreous Semiconductors (I). *phys. stat. sol. (b)*, 7(2):359–372, 1964. 23

[28] A. F. Ioffe and A. R. Regel. Non-crystalline, amorphous, and liquid electronic semiconductors. *Prog. Semicond.*, 4:237–291, 1960. 24, 32

[29] P W Anderson. Absence of Diffusion in Certain Random Lattices. *Phys. Rev.*, 109:1492–1505, 1958. 24, 25, 26, 32

[30] Nevill Mott. *Metal-Insulator Transitions.* Taylor & Francis, London, 2 edition, 1990. 24

[31] P W Anderson. The Fermi Glass: Theory and Experiment. *Comments Solid State Phys.*, 2:193–197, 1970. 25, 28

[32] P. W. Anderson. Local moments and localized states. *Reviews of Modern Physics*, 50(2):191–201, 1978. 25

[33] N. F. Mott. Conduction in non-Crystalline systems IV. Anderson Localization in a Disordered Lattice. *Philosophical Magazine*, 22(175):7–29, July 1970. xii, xiii, 26, 27, 31, 34, 35

[34] N.F. Mott. Electrons in disordered structures. *Advances in Physics*, 16(61):49–144, January 1967. 28

[35] N. F. Mott. Conduction in non-crystalline systems. *Philosophical Magazine*, 17(150):1259–1268, June 1968. xiii, 28, 32, 33

[36] Morrel H. Cohen, H. Fritzsche, and S. R. Ovshinsky. Simple Band Model for Amorphous Semiconducting Alloys. *Physical Review Letters*, 22(20):1065–1068, 1969. xiii, 28, 30, 38, 40

[37] J. M. Ziman. *Models of Disorder: The Theoretical Physics of Homogeneously Disordered Systems*. Cambridge University Press, 1 edition, October 1979. xii, 28, 29

[38] N.F. Mott and W.D. Twose. The theory of impurity conduction. *Advances in Physics*, 10(38):107–163, April 1961. 32

[39] N. F. Mott. Conduction in non-crystalline systems IX. the minimum metallic conductivity. *Philosophical Magazine*, 26(4):1015–1026, October 1972. 34

[40] Nevill Mott, M. Pepper, S. Pollitt, R. H. Wallis, and C. J. Adkins. The Anderson Transition. *Proceedings of the Royal Society of London. Series A, Mathematical and Physical Sciences*, 345(1641), 1975. xiii, 35, 36, 37

[41] N F Mott. Conduction in glasses containing transition metal ions. *Journal of Non-Crystalline Solids*, 1(1):1–17, December 1968. 36

[42] E. A. Davis and N. F. Mott. Conduction in non-crystalline systems V. Conductivity, optical absorption and photoconductivity in amorphous semiconductors. *Philosophical Magazine*, 22(179):903–922, 1970. xiii, xiv, 39, 40, 41

[43] N. F. Mott. Conduction in non-crystalline systems. VII. Non-ohmic behaviour and switching. *Philosophical Magazine*, 24(190):911–934, 1971. xiii, 40, 139

[44] H. Scher and E. W. Montroll. Anomalous transit-time dispersion in amorphous solids. *Physical Review B*, 12(6):2455–2477, 1975. xiv, 42, 43, 49, 62, 69, 98

[45] G. Pfister and H. Scher. Dispersive (non-Gaussian) transient transport in disordered solids. *Advances in Physics*, 27(5):747–798, 1978. 42, 69, 92, 98

[46] Georges Charpak. Electronic imaging of ionizing radiation with limited avalanches in gases. *Reviews of Modern Physics*, 65:591–598, 1993. xiv, 45, 46, 47, 48

[47] G. F. Knoll. Proportional Counters. In *Radiation Detection and Measurement*, book chapter/section 6. Wiley, 3rd edition, 1999. 46

[48] G. Charpak, R. Bouclier, T. Bressani, J. Favier, and C. Zupancic. The use of multiwire proportional counters to select and localize charged particles. *Nuclear Instruments and Methods*, 62(3):262–268, July 1968. 46, 75, 91

[49] G. Charpak. Applications of proportional chambers and drift chambers in high-energy physics and other fields. *Nature*, 270:479–482, December 1977. 46, 91

[50] G. Charpak, G. Petersen, A. Policarpo, and F. Sauli. Progress in high-accuracy proportional chambers. *Nuclear Instruments and Methods*, 148(3):471–482, February 1978. 46

[51] G. Charpak and F. Sauli. Multiwire proportional chambers and drift chambers. *Nuclear Instruments and Methods*, 162, 1979. xiv, 46, 48

[52] A. Oed. Position-sensitive detector with microstrip anode for electron multiplication with gases. *Nuclear Instruments and Methods A*, 263(2-3):351–359, January 1988. 47, 75, 76, 91

[53] F. Angelini, R. Bellazzini, A. Brez, M. M. Massai, R. Raffo, G. Spandre, and M. A. Spezziga. The micro-gap chamber. *Nuclear Instruments and Methods A*, 335(1-2):69–77, October 1993. 47, 91

[54] Y. Giomataris. MICROMEGAS: a high-granularity position-sensitive gaseous detector for high particle-flux environments. *Nuclear Instruments and Methods A*, 376(1):29–35, June 1996. 47, 91

[55] F. Sauli. GEM: A new concept for electron amplification in gas detectors. *Nuclear Instruments and Methods A*, 386(2-3):531–534, February 1997. 47, 91

[56] W. Spear. Drift mobility techniques for the study of electrical transport properties in insulating solids. *Journal of Non-Crystalline Solids*, 1(3):197–214, April 1969. 49, 95

[57] G. Pfister. Hopping transport in a molecularly doped organic polymer. *Phys. Rev. B*, 16(8), October 1977. 49, 62

[58] J. A. Rowlands, G. DeCrescenzo, and N. Araj. Xray imaging using amorphous selenium: Determination of xray sensitivity by pulse height spectroscopy. *Medical Physics*, 19(4):1065–1069, 1992. x, xiv, 50, 51, 53

[59] E J Hoffman and M E Phelps. Production of monoenergetic X-rays from 8 to 87 keV (for use in chemical analysis). *Physics in Medicine and Biology*, 19(1), January 1974. 50

[60] I. M. Blevis, D. C. Hunt, and J. A. Rowlands. Measurement of x-ray photogeneration in amorphous selenium. *Journal of Applied Physics*, 85(11):7958–7963, 1999. 53, 110

[61] S. S. Kapoor and V. Ramamurthy. Electronics for Detector Signal Processing. In *Nuclear Radiation Detectors*, book chapter/section VII. John Wiley & Sons, April 1986. 55

[62] T. Wu, A. Stewart, M. Stanton, T. McCauley, W. Phillips, D. B. Kopans, R. H. Moore, J. W. Eberhard, B. Opsahl-Ong, and M. B. Williams. Tomographic mammography using a limited number of low-dose cone-beam projection images. *Medical Physics*, 30(3):365–380, 2003. 56

[63] L Jones and P Woollam. Resolution improvement in CdTe gamma detectors using pulse-shape discrimination. *Nuclear Instruments and Methods*, 124(2):591–595, March 1975. 56

[64] M. Richter and P. Siffert. High resolution gamma ray spectroscopy with CdTe detector systems. *Nuclear Instruments and Methods in Physics Research Section A: Accelerators, Spectrometers, Detectors and Associated Equipment*, 322(3):529–537, November 1992. 56, 57

[65] H. L. Malm, C. Canali, J. W. Mayer, M-A. Nicolet, K. R. Zanio, and W. Akutagawa. Gamma-ray spectroscopy with single-carrier collection in high-resistivity semiconductors. *Applied Physics Letters*, 26(6):344–346, March 1975. 58

[66] H. H. Barrett, J. D. Eskin, and H. B. Barber. Charge Transport in Arrays of Semiconductor Gamma-Ray Detectors. *Physical Review Letters*, 75(1):156–159, 1995. 58

[67] O. Frisch. Untitled. *British atomic energy report*, BR-49, 1944. 58, 59, 64, 74

[68] P. N. Luke. Single-polarity charge sensing in ionization detectors using coplanar electrodes. *Applied Physics Letters*, 65(22):2884–2886, 1994. 58, 129

[69] P.N. Luke. Unipolar charge sensing with coplanar electrodes-application to semiconductor detectors. *Nuclear Science, IEEE Transactions on*, 42(4):207–213, August 1995. 58, 129

[70] Direct X-ray detectors. 59

[71] A. H. Goldan and K. S. Karim. Unipolar charge sensing using Frisch grid technique for amorphous selenium radiation detectors. In *Proceedings of SPIE*, volume 7079. The International Society for Optical Engineering., August 2008. 59

[72] W. Shockley. Currents to Conductors Induced by a Moving Point Charge. *Journal of Applied Physics*, 9(10):635–636, 1938. 60, 129

[73] S. Ramo. Currents Induced by Electron Motion. *Proceedings of the IRE*, 27(9):584–585, September 1939. 60, 129

[74] G. Cavalleri, G. Fabri, E. Gatti, and V. Svelto. On the induced charge in semiconductor detectors. *Nuclear Instruments and Methods*, 21(C), January 1963. 61

[75] G Cavalleri, E Gatti, G Fabri, and V Svelto. Extension of Ramo's theorem as applied to induced charge in semiconductor detectors. *Nuclear Instruments and Methods*, 92(1):137–140, March 1971. 61

[76] J. Noolandi. Multiple-trapping model of anomalous transit-time dispersion in a-Se. *Physical Review B*, 16(10):4466–4473, 1977. 62

[77] M. Redecker, D. D. C. Bradley, M. Inbasekaran, and E. P. Woo. Nondispersive hole transport in an electroluminescent polyfluorene. *Applied Physics Letters*, 73(11):1565–1567, 1998. 62

[78] A. Many and G. Rakavy. Theory of Transient Space-Charge-Limited Currents in Solids in the Presence of Trapping. *Physical Review Online Archive (Prola)*, 126(6):1980–1988, 1962. 68, 98

[79] B. Polischuk, S. O. Kasap, and A. Baillie. Study of photogenerated charge carrier dispersion in chlorinated aSe:0.3%As by the interrupted field timeofflight technique. *Applied Physics Letters*, 63(2):183–185, July 1993. 69

[80] S O Kasap, D Brinkhurst, and C Haugen. Modelling of photoinduced discharge of photoreceptors under pulsed photoexcitation: small and large signal xerographic time-of-flight analysis. *Journal of Physics D: Applied Physics*, 33(4), February 2000. 69

[81] S. O. Kasap, C. Haugen, B. Polischuk, E. V. Emelianova, and V. I. Arkhipov. Field dependence of the hole transit-time dispersion in As-Cl stabilized amorphous selenium X-ray photoconductors. *Journal of Imaging Science and Technology*, 45(1):30–36, 2001. 69

[82] W. Que and J. A. Rowlands. Xray imaging using amorphous selenium: Inherent spatial resolution. *Medical Physics*, 22, January 1995. 69, 101, 102, 115

[83] A. H. Goldan and K. S. Karim. Method and Apparatus for a Radiation Detector. *Notice of Allowance Issued*, US Patent(12/357577), October 2011. 76

[84] Non Photodefinable Dry Etch, PI-2600 Series. 80

[85] J. M. Marshall and A. E. Owen. Drift mobility studies in vitreous arsenic triselenide. *Philosophical Magazine*, 24(192):1281–1305, 1971. 92

[86] J. M. Marshall and A. E. Owen. The hole drift mobility of vitreous selenium. *phys. stat. sol. (a)*, 12(1):181–191, 1972. 92

[87] G. Pfister. Dispersive Low-Temperature Transport in a-Selenium. *Physical Review Letters*, 36(5):271–273, 1976. 92

[88] G. Pfister and C. H. Griffiths. Temperature Dependence of Transient Hole Hopping Transport in Disordered Organic Solids: Carbazole Polymers. *Phys. Rev. Lett.*, 40(10), March 1978. 92

[89] J. X. Mack, L. B. Schein, and A. Peled. Hole mobilities in hydrazone-polycarbonate dispersions. *Phys. Rev. B*, 39(11), April 1989. 92

[90] J. A. Rowlands and S. Kasap. Amorphous Semiconductors Usher in Digital X-Ray Imaging. *Physics Today*, 50(11):24–30, 1997. 93

[91] G. Juška and K. Arlauskas. Impact ionization and mobilities of charge carriers at high electric fields in amorphous selenium. *phys. stat. sol. (a)*, 59(1):389–393, 1980. 93

[92] K. Tanioka. The ultra sensitive TV pickup tube from conception to recent development. *Journal of Materials Science: Materials in Electronics*, 18(0):321–325, October 2007. 93, 140

[93] M. M. Wronski, W. Zhao, A. Reznik, G. DeCrescenzo, K. Tanioka, and J. A. Rowlands. A solid-state amorphous selenium avalanche technology for low photon flux imaging applications. *MEDICAL PHYSICS LETTERS*, 37(9), August 2010. 93

[94] P. M. Borsenberger, L. T. Pautmeier, and H. Bässler. Scaling behavior of nondispersive charge transport in disordered molecular solids. *Physical Review B*, 48(5):3066–3073, 1993. 99

[95] A. W. Rau, L. Bakueva, and J. A. Rowlands. The x-ray time of flight method for investigation of ghosting in amorphous selenium-based flat panel medical x-ray imagers. *Medical Physics*, 32(10), September 2005. 101

[96] M. Zahangir Kabir and S. O. Kasap. Charge collection and absorption-limited x-ray sensitivity of pixellated x-ray detectors. *Journal of Vacuum Science & Technology A: Vacuum, Surfaces, and Films*, 22(3):975–980, May 2004. 107, 119

[97] S O Kasap. X-ray sensitivity of photoconductors: application to stabilized a-Se. *Journal of Physics D: Applied Physics*, 33(21), November 2000. 107, 127

[98] M. Zahangir Kabir and S. O. Kasap. Charge collection and absorption-limited sensitivity of x-ray photoconductors: Applications to a-Se and HgI[sub 2]. *Applied Physics Letters*, 80(9):1664–1666, 2002. 107

[99] M. Zahangir Kabir and S. O. Kasap. Sensitivity of x-ray photoconductors: Charge trapping and absorption-limited universal sensitivity curves. *Journal of Vacuum Science & Technology A: Vacuum, Surfaces, and Films*, 20(3):1082–1086, May 2002. 107

[100] Majid Rabbani, Rodney Shaw, and Richard Van Metter. Detective quantum efficiency of imaging systems with amplifying and scattering mechanisms. *J. Opt. Soc. Am. A*, 4(5):895–901, May 1987. 109

[101] Majid Rabbani and Richard Van Metter. Analysis of signal and noise propagation for several imaging mechanisms. *J. Opt. Soc. Am. A*, 6(8):1156–1164, August 1989. 109

[102] Ian A. Cunningham and Rodney Shaw. Signal-to-noise optimization of medical imaging systems. *J. Opt. Soc. Am. A*, 16(3):621–632, March 1999. 109

[103] H. H. Barrett and W. Swindell. *Radiological Imaging: The Theory of Image Formation, Detection, and Processing.* Academic Press, October 1996. 110

[104] W. Que and J. A. Rowlands. X-ray photogeneration in amorphous selenium: Geminate versus columnar recombination. *Physical Review B*, 51:10500–10507, 1995. 110

[105] J Hirsch and H Jahankhani. The carrier yield in a-Se under electron bombardment. *Journal of Physics: Condensed Matter*, 1(45), November 1989. 110

[106] M Zahangir Kabir and S O Kasap. DQE of photoconductive x-ray image detectors: application to a-Se. *Journal of Physics D: Applied Physics*, 35(21), November 2002. 111, 121

[107] D R Dance and G J Day. Escape probabilities for fluorescent X-rays. *Physics in Medicine and Biology*, 30(3), March 1985. 111

[108] J. G. Mainprize, D. C. Hunt, and M. J. Yaffe. Direct conversion detectors: The effect of incomplete charge collection on detective quantum efficiency. *Medical Physics*, 29(6):976–990, 2002. 112

[109] S.O. Kasap and J.A. Rowlands. Direct-conversion flat-panel X-ray image sensors for digital radiography. *Proceedings of the IEEE*, 90(4):591–604, April 2002. 115

[110] M Zahangir Kabir and S O Kasap. Modulation transfer function of photoconductive x-ray image detectors: effects of charge carrier trapping. *Journal of Physics D: Applied Physics*, 36(19), October 2003. 115, 124

[111] Oliver D. Kellogg. *Foundations of Potential Theory (Dover Books on Advanced Mathematics)*. Dover Publications, October 2010. 116

[112] J. A. Rowlands and J. Yorkston. Flat Panel Detectors for Digital Radiography. In *Handbook of Medical Imaging*, volume 1, book chapter/section 4. SPIE Publications, 1st edition, February 2000. 119

[113] Satoshi Tokuda, Hiroyoki Kishihara, Susumu Adachi, Toshiyuki Sato, Yoshihiro Izumi, Osamu Teranuma, Yasukuni Yamane, and Satoshi Yamada. Large-area deposition of a polycrystalline CdZnTe film and its applicability to x-ray panel detectors with superior sensitivity. In *Proceedings of SPIE*, volume 4682. The International Society for Optical Engineering., May 2002. xx, 122, 123

[114] George Zentai, Larry D. Partain, Raisa Pavlyuchkova, Cesar Proano, Gary F. Virshup, Barry N. Breen, Asaf Zuck, Benjamin Reisman, A. Taieb, and Michael M. Schieber. Large area mercuric iodide thick film x-ray detectors for fluoroscopic (online) imaging. In *Proceedings of SPIE*, volume 4702. The International Society for Optical Engineering., June 2002. xx, 122, 123

[115] JG Mainprize, NL Ford, S Yin, T Tümer, and MJ Yaffe. A slot-scanned photodiode-array/CCD hybrid detector for digital mammography. *Med Phys*, 29(2):214–225, February 2002. 122

[116] A. Zuck, M. Schieber, O. Khakhan, and Z. Burshtein. Near single-crystal electrical properties of polycrystalline HgI2 produced by physical vapor deposition. *Nuclear Science, IEEE Transactions on*, 50(4):991–997, August 2003. 123

[117] Olivier Tousignant, Martin Choquette, Yves Demers, Luc Laperriere, Jonathan Leboeuf, Michitaka Honda, Masayuki Nishiki, Akihito Takahashi, and Akira Tsukamoto. Progress report on the performance of real-time selenium flat-panel detectors for direct x-ray imaging. In *Proceedings of SPIE*, volume 4682. The International Society for Optical Engineering., May 2002. xx, 123, 124, 125

[118] S O Kasap and C Juhasz. Time-of-flight drift mobility measurements on chlorine-doped amorphous selenium films. *Journal of Physics D: Applied Physics*, 18(4), April 1985. 123

[119] W Zhao, WG Ji, A Debrie, and JA Rowlands. Imaging performance of amorphous selenium based flat-panel detectors for digital mammography: characterization of a small area prototype detector. *Med Phys*, 30(2):254–263, February 2003. 124

[120] H. Fujita, D.-Y. Tsai, T. Itoh, K. Doi, J. Morishita, K. Ueda, and A. Ohtsuka. A simple method for determining the modulation transfer function in digital radiography. *Medical Imaging, IEEE Transactions on*, 11(1):34–39, March 1992. 124

[121] Mohammad Z. Kabir and Safa O. Kasap. Charge transport and trapping-limited sensitivity and resolution of pixellated x-ray image detectors. In *Proceedings of SPIE*, volume 5030. The International Society for Optical Engineering., June 2003. 124

[122] C. Haugen, S. O. Kasap, and J. Rowlands. X-ray irradiation induced bulk space charge in stabilized a-Se x-ray photoconductors. *Journal of Applied Physics*, 84(10):5495–5501, 1998. 124, 128, 132

[123] B. Zhao and W. Zhao. Temporal performance of amorphous selenium mammography detectors. *Medical Physics*, 32(1):128–136, 2005. 125, 132

[124] M. Bissonnette, M. Hansroul, E. Masson, S. Savard, S. Cadieux, P. Warmoes, D. Gravel, J. Agopyan, B. Polischuk, W. Haerer, T. Mertelmeier, J. Y. Lo, Y. Chen, J. T. Dobbins III, J. L. Jesneck, and S. Singh. Digital breast tomosynthesis using an amorphous selenium flat panel detector. In *Proceedings of SPIE*, volume 5745, pages 529–540. The International Society for Optical Engineering., April 2005. 125

[125] James G. Mainprize, Xinying Wang, and Martin J. Yaffe. The effect of lag on image quality for a digital breast tomosynthesis system. In *Proceedings of SPIE*, volume 7258. The International Society for Optical Engineering., February 2009. 125

[126] S. O. Kasap, Bud Fogal, M. Zahangir Kabir, Robert E. Johanson, and Stephen K. O'Leary. Recombination of drifting holes with trapped electrons in stabilized a-Se photoconductors: Langevin recombination. *Applied Physics Letters*, 84(11):1991–1993, 2004. 128

[127] N Hindley. Random phase model of amorphous semiconductors II. Hot electrons. *Journal of Non-Crystalline Solids*, 5(1):31–40, September 1970. 139

[128] E. Gatti and P. Rehak. Semiconductor drift chamber An application of a novel charge transport scheme. *Nuclear Instruments and Methods*, 225(3):608–614, September 1984. 140

[129] F. S. Goulding and Y. Stone. Semiconductor Radiation Detectors. *Science*, 170(3955):280–289, October 1970. 140

[130] E. Costa, P. Soffitta, R. Bellazzini, A. Brez, N. Lumb, and G. Spandre. An efficient photoelectric X-ray polarimeter for the study of black holes and neutron stars. *Nature*, 411(6838):662–665, June 2001. 140

[131] J. Miao, P. Charalambous, J. Kirz, and D. Sayre. Extending the methodology of X-ray crystallography to allow imaging of micrometre-sized non-crystalline specimens. *Nature*, 400(6742):342–344, July 1999. 140